Technical University Munich

Department of Physics

Experimental Physics with Cosmic Particles

Precision background modeling for neutrino telescopes

Stephan Meighen-Berger

Technische Universität München
Fakultätsgraduiertenzentrum Physik
Experimentalphysik mit kosmischer Strahlung

Precision background modeling for neutrino telescopes

Stephan Meighen-Berger

Vollständiger Abdruck der von der Fakultät für Physik der Technischen Universität München zur Erlangung des akademischen Grades eines Doktors

Doktor der Naturwissenschaften (Dr. rer. nat.)

genehmigten Dissertation.

Vorsitzende/-r:

Prof. Dr. Andreas Weiler

Prüfende/-r der Dissertation:

1. Prof. Dr. Elisa Resconi
2. Prof. Dr. Alejandro Ibarra

Die Dissertation wurde am 02.06.2021 bei der Technischen Universität München eingereicht und durch die Fakultät für Physik am 23.07.2021 angenommen.

Technical University Munich
Department Graduate Center Physics
Experimental Physics with Cosmic Particles

Precision background modeling for neutrino telescopes

Stephan Meighen-Berger

Complete copy of the dissertation approved by the Physics Department of the Technical University of Munich to obtain the academic degree of

Doctor of Natural Sciences (Dr. rer. nat.)

Head of Committee:

Prof. Dr. Andreas Weiler

Dissertation Examination:

1. Prof. Dr. Elisa Resconi
2. Prof. Dr. Alejandro Ibarra

The dissertation was submitted to the Technical University Munich on 02.06.2021 and accepted by the Physics Department on 23.07.2021.

I certify that this thesis, and the research to which it refers, are the product of my own work, and that any ideas or quotations from the work of other people, published or otherwise, are fully acknowledged in accordance with the standard referencing practices of the discipline.

Signed:

Abstract

In this thesis we present tools and methods useful for precise atmospheric cascade and bioluminescence modeling, required by cosmic ray, gamma ray and neutrino experiments. We will show how to employ these methods to perform traditional studies such as the kaon-pion ratio, where we use BOREXINO data to set a ratio of $0.11^{+0.11}_{-0.07}$ at approximately 190 GeV center of mass energy. Then, we will introduce a new electromagnetic simulation framework, which includes a new interaction model, as well as those employed by other electromagnetic cascade simulators. The difference between these models is of relevance when measuring the total energy of atmospheric showers by fluorescence experiments, causing a change of up to 5%. By using the precision calculations introduced in the previous sections, we perform a new type of study on the supersymmetric partner particle of the tau, the stau. In this analysis we set a lower mass-bound of 320 GeV on this new particle using 1 year of public data from IceCube. Afterwards we perform another study on the limit setting capability of IceCube on the astrophysical antiproton flux. We find IceCube is able to set limits at energies above 10 TeV, the first experiment capable of doing so. Additionally, the antiproton flux could explain some of the neutrino flux typically attributed to the astrophysical sources. Finally, we introduce a new simulation framework to model bioluminescence for deep sea neutrino detectors. There we show the relevance of shear stress on the emission spectra and compare the simulation results to preliminary STRAW-b data.

Zusammenfassung

In dieser Arbeit stellen wir Werkzeuge und Methoden vor, die für eine präzise Modellierung atmosphärischer Teilchenkaskaden und Biolumineszenz nützlich sind, die für Experimente mit kosmischer Strahlung, Gammastrahlung und Neutrinos benötigt werden. Wir zeigen, wie man diese Methoden einsetzt, um traditionelle Studien durchzuführen, wie z.B. das Kaon-Pion-Verhältnis, bei dem wir mit Hilfe von BOREXINO Daten ein Verhältnis von $0.11^{+0.11}_{-0.07}$ bei einer Schwerpunktsenergie von etwa 190 GeV bestimmen. Anschließend stellen wir ein neues elektromagnetisches Simulationspaket vor, das ein neues Wechselwirkungsmodell beinhaltet, wie auch Modelle die von anderen elektromagnetischen Kaskadensimulatoren verwendet werden. Der Unterschied zwischen diesen Modellen ist bei der Messung der Gesamtenergie von atmosphärischen Schauern durch Fluoreszenzexperimente von Bedeutung und verursacht eine Änderung von bis zu 5% in der gemessenen Energie. Unter Verwendung der in den vorherigen Abschnitten vorgestellten Präzisionsrechnungen führen wir eine neuartige Untersuchung des supersymmetrischen Partnerteilchens des Tau, das Stau, durch. In dieser Analyse setzen wir, unter Verwendung von 1 Jahr öffentlicher Daten von IceCube, eine untere Massengrenze von 320 GeV für dieses neue Teilchen. Anschließend führen wir eine weitere Studie über die Fähigkeit von IceCube zur Grenzwertsetzung für den astrophysikalischen Antiprotonen-Fluss durch. Wir stellen fest, dass IceCube als erstes Experiment in der Lage ist, Grenzen bei Energien über 10 TeV zu setzen. Außerdem könnte der Antiprotonenfluss einen Teil vom gesamten Neutrinostrom erklären, der typischerweise astrophysikalischen Quellen zugeordnet wird. Schließlich stellen wir einen neuen Simulationsrahmen zur Modellierung der Biolumineszenz für Tiefsee-Neutrinodetektoren vor. Dort zeigen wir die Relevanz von Turbulenzen auf die Emissionsspektren von Organismen und vergleichen die Simulationsergebnisse mit vorläufigen STRAW-b Daten.

Acknowledgments

I would like to thank my supervisor Prof. Elisa Resconi for her strong support throughout my PhD. Her continuous steam of ideas and our fruitful discussions are the basis of many of the works presented in this thesis.

Many thanks go out to Hans Niederhausen and Matteo Agostini. Each showed a great deal of patience when explaining statistics and experimental analyses to this theoretician.

Without the support from Golo Wimmer, the bioluminescence simulations would never have come to be. It was his suggestion to collaborate and without his expertise in fluid simulations this project would never have gotten off the ground.

Apologies and a thanks go out to my all of my colleagues who shared an office with me during my studies. They had to suffer through a lot of complaining and nagging.

I would also like to thank my family and friends for their continued patience, love and support throughout my PhD. This has proven to be a strong foundation for a productive and enjoyable PhD.

Finally, I would like to thank the DFG Sonderforschungsbereich Neutrinos and Dark Matter in Astro- and Particle Physics (SFB1258) which enabled me to pursue a PhD through their funding and support.

Publication List

- M. Agostini *et al.*, "The Pacific Ocean Neutrino Experiment", *Nature Astron.*, vol. 4, no. 10, pp. 913-915, 2020.
  Contribution: Calculated the neutrino veto and limit setting capabilities on staus

- S. Meighen-Berger *et al.*, "New constraints on supersymmetry using neutrino telescopes", *Physics Letters B*, vol. 811, p. 135929, 2020
  Contribution: Leading author. Developed phenomenology, wrote simulation and analysis framework and wrote the paper.

- M. Agostini *et al.*, "Modulation of the Cosmic Muon Signal in Ten Years of Borexino Data", *JCAP*, vol. 02, p. 046, 2019
  Contribution: Wrote the atmospheric muon simulation using cascade equations.

- S. Meighen-Berger and M. Li, "Atmospheric muons from electromagnetic cascades", *PoS*, vol. ICRC2019, p. 961, 2020
  Contribution: Leading author. Wrote the simulation and analysis framework and wrote the paper.

- S. Meighen-Berger, A. Fedynitch and M. Huber, "EmCa - Electromagnetic-Cascades Simulation Package", *arXiv*, 1907.06924, 2019
  Contribution: Leading author. Wrote the simulation framework and built the underlying physical model. Wrote the paper.

- S. Meighen-Berger, L. Ruohan and G. Wimmer, "Bioluminescence modeling for deep-sea neutrino telescopes", *arXiv*, 2103.03816, 2021
  Contribution: One of the leading authors. Developed the biological population model and light propagation. Developed the phenomenological analysis and wrote the paper.

- A. Ibarra and S. Meighen-Berger, "Constraining the antiproton flux using neutrino telescopes", *in preparation*
  Contribution: One of the leading authors. Wrote the simulation and analysis framework. Developed the phenomenology. Wrote parts of the paper

- T.R. Pollmann *et al.*, "The impact of digital contact tracing on the sars-cov-2 pandemic - a comprehensive modelling study", **medRxiv**, 2020.09.13.20192682
  Contribution: Developed the python simulation framework.

Contents

Abstract viii

Zusammenfassung ix

Acknowledgments x

Publication List xi

Contents xii

1 Introduction 1

2 Theory 3
- 2.1 Model Components . . . 4
  - Cosmic Primary Flux . . . 4
  - Atmosphere . . . 6
  - Particle Interactions . . . 7
- 2.2 Cascade Equations . . . 11
  - Example Application . . . 12
  - Matrix Form . . . 15
  - Method of Moments . . . 17

3 Modulation of the Cosmic Muon Signal in Ten Years of Borexino Data 19
- 3.1 Introduction . . . 19
- 3.2 Parametrization . . . 19
- 3.3 BOREXINO . . . 20
- 3.4 Results . . . 20
- 3.5 Conclusion . . . 22

4 EmCa - Electromagnetic Cascades 25
- 4.1 Coupled Cascade Equations . . . 27
- 4.2 Theoretical Model . . . 27
  - Material Effects . . . 32
- 4.3 Numerical Implementation . . . 34
  - Ionization . . . 36
  - Code . . . 38
- 4.4 Comparisons . . . 41
  - CORSIKA . . . 41
  - EGS4 . . . 42
- 4.5 Three Dimensions . . . 43
  - Landau approximation . . . 43
  - Molière Treatment . . . 45
  - Numerical implementation . . . 46
- 4.6 Conclusions . . . 47

5 Fluorescence from Electromagnetic Cascades 49
  - Models . . . 49
- 5.1 Fluorescence . . . 50
- 5.2 Results . . . 51

6 New Constraints on Supersymmetry Using Neutrino Telescopes 53
6.1 Production 54
6.2 Propagation 55
6.3 Background 57
6.4 Detector Response 57
6.5 Events 59
6.6 Energy and Angular Cut 60
6.7 Results 60

7 Antiprotons 63
7.1 Decaying Dark Matter 63
7.2 Atmospheric Showers 65
7.3 Astrophysical Neutrinos 65
7.4 Results 65
7.5 Conclusion 68

8 Bioluminescence 69
8.1 Bioluminescence Triggers 69
8.2 Population Modeling 70
8.3 Current Modeling 70
Discretization 72
8.4 Light Propagation 75
8.5 Fourth Day 75
8.6 Discussion 77
8.7 Simulation vs Data 81
8.8 Conclusion 82

9 Conclusion 83

List of Figures

2.1 Cascade Sketch . . . 3
2.2 Theoretical Primary Spectrum . . . 5
2.3 Primary Cosmic Ray Models . . . 6
2.4 Extended U.S. Standard Atmosphere . . . 7
2.5 PDG Proton Target Data . . . 7
2.6 Sibyll Comparison to Data . . . 7
2.7 Proton-Air Scaling Difference . . . 8
2.8 Proton-Air Comparison Between Models . . . 8
2.9 Collision Cartoon . . . 9
2.10 Proton PDF . . . 10
2.11 PDG $p\bar{p}$ Data . . . 10
2.12 PYTHIA Weak . . . 10
2.13 PYTHIA All . . . 11
2.14 Atmospheric Neutrinos from the Sun and Earth . . . 15
2.15 Relevant Interaction Lengths in Hadronic Cascades . . . 17
2.16 Example Particle Flux above IceCube . . . 18
3.1 Seasonal Flux Change IceCube . . . 19

3.2 Muon Production and Temperature . . . 20
3.3 Atmospheric Muon Fluxes above BOREXINO . . . 20
3.4 Atmospheric Muon Fluxes Change above BOREXINO . . . 21
3.5 Theoretical and Experimental Results for α_T . . . 21
3.6 Ratio Measurement Between K and π . . . 22

4.1 Pair Production . . . 25
4.2 Screening Effect on Pair Production . . . 28
4.3 Electromagnetic Differential Cross Sections . . . 30
4.4 Electromagnetic Interaction Lengths . . . 31
4.5 Electromagnetic Cross Sections . . . 32
4.6 LPM Shower Changes . . . 33
4.7 Stability Bremsstrahlung . . . 34
4.8 Stability Regeneration μ . . . 35
4.9 Stability Self Regeneration . . . 35
4.10 Equation Matrix . . . 36
4.11 Ionization . . . 37
4.12 EmCa Structure . . . 38
4.13 The Simulation Time from EmCa . . . 39
4.14 Example Results from EmCa . . . 40
4.15 EmCa vs CORSIKA . . . 41
4.16 Shower Maximum Development . . . 42
4.17 EmCa vs EGS4 . . . 43
4.18 Landau Spread of Electrons . . . 45
4.19 First 3D Approximation using Landau . . . 46
4.20 Moliere Spread of Electrons . . . 46
4.21 First 3D using Landau . . . 47
4.22 First 3D using Moliere . . . 47

5.1 Shower Difference between BH and Tsai 49
5.2 Differences between BH and Tsai 50
5.3 Electron Production Difference 51
5.4 Energy Measurement Difference 52

6.1 Stau Cross Section 54
6.2 Hadron Air Cross Section 55
6.3 Energy Loss of the Muon 55
6.4 Energy Loss of the Stau 56
6.5 Angular Dependence of the Stau Flux 56
6.6 Surface Fluxes above IceCube 57
6.7 IceCube Energy Reconstruction 58
6.8 Energy Distribution Comparison 58
6.9 Total Event Counts in IceCube 59
6.10 Final Stau Count 60
6.11 Future IceCube Limits 61

7.1 DM $\bar{p}$ Flux 64
7.2 DM $\bar{p} - p$ Ratio 64
7.3 Atmospheric ν from h 65
7.4 Astrophysical ν from h 66
7.5 Predicted h Limits 67
7.6 Antiproton IceCube vs HAWC 67

8.1 Magnitude of the Velocity Field 72
8.2 Mesh Overview 72
8.3 Zoomed in Mesh 72
8.4 Velocity Field After 200 Seconds 75
8.5 FD Code Structure 75
8.6 Example State 76
8.7 Organism Distribution 78
8.8 Spectrometer Simulation 79
8.9 PDF Spread due to the Velocity Field 79
8.10 Fourier Transform of the Emissions 80
8.11 Average Number of Flashes 81
8.12 Injected Organism's Emission Profile 81
8.13 STRAW-b Comparison 82

List of Tables

2.1 H4a Model Parameters 5

6.1 Hadron Air Table 54

Introduction | 1

More than a hundred years ago Victor Hess performed his famous balloon experiments, finding that ionizing radiation increases the further one is from the ground. He concluded that radiation must be coming from extraterrestrial sources, which was confirmed later by Robert Andrews Millikan. He gave this particle flux from space the name "cosmic rays". In 1936 Victor Hess was awarded the Nobel Prize for his discovery of this astrophysical particle flux.

Today we know that when extraterrestrial particles reach the Earth, they collide with the atmosphere and produce particle cascades. There are a multitude of experiments which study these particle showers as a source of new physics, to benchmark our understanding of the standard model or in the source of their production sites. Cosmic ray experiments such as KASCADE [1], CASA-MIA [2], AGASA [3], HiRes [4], Auger [5] KASCADE-Grande [6], ARGO [7], TAIGA [8] and CREAM [9], gamma-ray experiments such as HAWC [10] and CTA [11] as well as neutrino experiments such as P-ONE [12], KM3NeT [13], GVD [14], ANTARES [15] and IceCube [16] all require precise modeling of these atmospheric cascades for their searches.

In this thesis, we will discuss how to precisely model such atmospheric particle cascades. First, we will give a brief introduction on the necessary components when modeling, such as the primary flux of cosmic rays, the atmospheric density, particle interactions and cascade equations.

We then show how these tools can be combined to calculate the seasonal variation of particle fluxes at particle detectors, specifically for the BOREXINO detector [17]. We then use these seasonal variations to estimate the ratio of kaons to pions being produced in the atmosphere.

Afterwards we will develop a new electromagnetic interaction model, which improves on previous models, by including material effects and by building on newer interaction calculations. We then show the effect these improvements have on cosmic ray experiments, by modeling the change in measured cosmic ray energy when using the fluorescence technique.

Having improved this cascade equation modeling scheme, we will then model the sensitivity of IceCube to a hypothetical beyond the standard model particle, the stau. Based on this, we will construct an estimate of the limits IceCube is capable of setting on this new particle's mass and compare them to current collider experiments.

Afterwards we perform an additional study, of the capability of neutrino telescopes to constrain a new antiproton component arriving at earth. This new particle flux could be produced by decaying dark matter in our galactic halo or neighborhood. This makes such studies highly relevant for theoreticians, since currently there are no constraints at very high energies on the antiproton to proton ratio.

Finally, moving away from particle cascades, we will apply similar techniques to develop the first precise model for bioluminescence at neutrino detectors in the deep sea. This topic has become more and more relevant with new water based neutrino telescopes coming online, such as P-ONE

[12] and KM3NeT [13]. We will show that neutrino telescopes are capable of measuring these flashes and able to identify the emitting organisms by utilizing our model. This makes such detectors not only relevant for the physics community, but for the biologist one as well.

Theory 2

When cosmic rays impinge on Earth's atmosphere, they initiate a particle cascade. A sketch of such a shower is shown in figure 2.1. During the shower's evolution, the secondaries, produced by the cosmic ray in the first interaction, in turn interact or decay again producing a new set of particles. This scheme proceeds until all unstable particles have decayed and the energy among the showering particles has been distrusted to such a level, that ionization losses dominate their energy loss. Ground based experiments measure the particles produced in these particle cascades, primarily muons and neutrinos. Due to their stability and low interaction cross sections, these species are capable of traversing the full atmosphere. In this chapter, we will give a brief introduction to the underlying theory required to understand transport of these particle cascades, the main focus of this thesis. We will start with a general introduction to the required components to construct particle shower models, namely a primary, a density and an interaction model. Afterwards we introduce cascade equations which we use to model particle showers.

2.1 Model Components 4
Cosmic Primary Flux 4
Atmosphere 6
Particle Interactions 7
2.2 Cascade Equations 11
Example Application 12
Matrix Form 15
Method of Moments 17

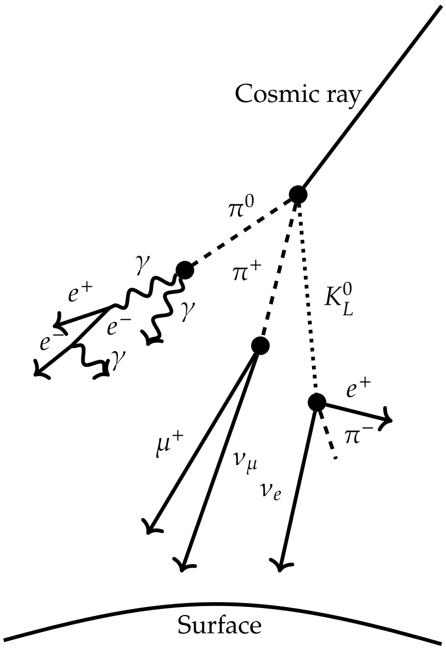

Figure 2.1: A sketch of an atmospheric particle cascade. The electromagnetic part can be treated as decoupled since the main coupling between it and the hadronic component is π^0 decay. The latter component is mainly driven by pions and kaons.

2.1 Model Components

Atmospheric cascade modeling, or any form of particle cascade modeling, requires three components:

- A primary model which defines the injected particle species and their energies.
- A density model which defines the target material.
- An interaction model which defines the particle interactions at the energies of interest.

In this section we discuss the fundamentals of these models and how to construct them.

Cosmic Primary Flux

In collider physics the primary spectrum is usually given by a delta peak of a single particle species at the beam's energy. In astrophysics the delta peak and single species is replaced by a spectrum of particle types and energies. Primarily protons and heavier nuclei, photons and neutrinos are of interest, depending on the experiment. Here we will focus on the proton and heavier nuclei spectra, commonly termed the cosmic ray flux. Being composed of ionized nuclei, their charge causes them to be deflected by astrophysical magnetic fields. This causes them to mostly arrive istotropically at Earth. This charges means a Lorentz force, F_L is applied by the external fields, B, of the form

$$F_\mathrm{L} = \frac{Ze}{c}\vec{v} \times \vec{B}. \tag{2.1}$$

Here Ze describes the charge of the nucleus and c is the speed of light. This causes the particles to spiral along the direction of the magnetic field lines [18]. The radius of this spiral motion is then defined by the Larmor radius, r_L, given by

$$r_\mathrm{L} \approx \frac{E}{ZeB}. \tag{2.2}$$

When the path traveled by the cosmic ray is of the same order as the Larmor radius, this deflection becomes relevant when pinpointing their origin. Our galaxy has an average magnetic field strength of $B \approx 4\ \mu\mathrm{G}$ [18], which we can use to estimate the required energy that the Larmor radius exceeds the size of our galaxy. At 1 EeV $r_\mathrm{L} \approx 300$ pc, which is larger than the thickness of our galactic disc, meaning particle with such ultra-high-energies could originate from beyond our galaxy, while at lower energies the particles are confined inside of the galactic volume. From this exercise we can derive that there must be at least two components when modeling cosmic rays, namely a galactic and extragalactic one.

As a first approximation we can ignore these two components and assume the cosmic ray flux, ϕ, is composed purely of protons and follows a simple power law

$$\phi(E) = 3.5\left(\frac{E}{\mathrm{GeV}}\right)^{-2.7} \times 10^4[(\mathrm{GeVm}^2\ \mathrm{sr\ s})^{-1}]. \tag{2.3}$$

Here E is the nucleus' total energy. We obtained the parameters by running a fit on the values given by figure 2.2, shown with the dotted line as PL(2.7). Over five orders of magnitude, namely between 10 GeV and 1 PeV, this approximation seems work very well and agree with data. While this approximation is enough for a general estimate, it can not reproduce features observed by cosmic ray experiments and more refined models are required for precision experiments. Multiple experiments have measured the energy dependence and composition of the cosmic ray flux, such as KASCADE [1], CASA-MIA [2], AGASA [3], HiRes [4], Auger [5] and CREAM [9]. The CREAM measurements are direct measurements, extending up to 100 TeV, making them an ideal baseline for modeling. Typically the nuclei are grouped into five groups H, He, CNO, Mg-Si and Mn-Fe [19] and their energy spectra need to be extrapolated to higher energies. To do this one can assume multiple underlying populations of cosmic rays, each with their own corresponding power law spectrum [20], which together need to described some observed features in the cosmic ray spectrum.

R_c	γ	p	He	CNO	Mg-Si	Fe
-	-	1.66	1.58	1.63	1.67	1.63
4 PeV	See line 1	7860	3550	2200	1430	2120
30 PeV	1.4	20	20	13.4	13.4	13.4
2 EeV	1.4	1.7	1.7	1.14	1.14	1.14
60 EeV	1.6	200	0	0	0	0

Table 2.1: Model parameters for equation 2.5 given by the H4a [19]model. These represent extrapolations from measurements done by CREAM [9]. The first column shows the cutoff R_c, while the second the power law's exponent $\gamma_{i,j}$. At 4 PeV differences in the species' power law's have been measured. For this reason the first line shows individual exponents for each type. The final 5 columns show the normalization factors $a_{i,j}$ for each nucleus type at a given energy.

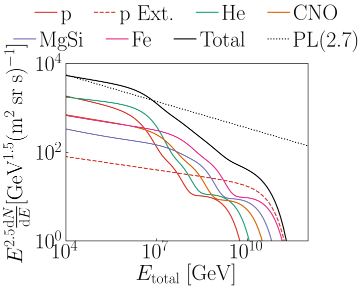

Figure 2.2: Example of a theoretical primary spectrum. The rigidity, normalization and spectral indices were taken from the H4a model [19]. Included as a dashed line is an additional high energy component of protons. The dotted line, PL(2.7), represents the fitted power-law described in equation 2.3.

At around 3 PeV the spectrum steepens and this region is usually termed the *knee*. This region is assumed to signal the end of one galactic population, namely those produced by supernova remnants.

The next feature is usually termed the *ankle* and is a flattening of the spectrum at approximately 10 EeV. Usually this is attributed to the end of cosmic rays produced in our galaxy. For energies above this an extra-galactic origin is assumed.

Together this means three populations are required to explain and model cosmic rays [21]:

- One associated with supernova remnants.
- A higher energy galactic component of unknown origin.
- An even higher energetic extra-galactic component with extra-galactic origin.

Each population shows a cutoff which can be assumed to depend on magnetic rigidity, R, [22]

$$R = \frac{E}{Ze}. \tag{2.4}$$

Here E and Ze are the nucleus' total energy and charge respectively. This is motivated by diffusion models in magnetized plasma which depend on R. Above a specific cutoff rigidity, R_c, acceleration reaches a limit, leading to a cutoff in the energy spectrum of the nuclei. Assuming a power law for each nucleus species, i, and origin, j, the total spectrum

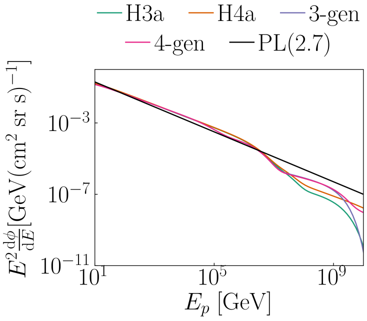

Figure 2.3: The proton fluxes as given by the H3a, H4a [19] and Gen 3 and 4 models [23] with a power-law approximation, PL(2.7). Discrepancies appear at the highest energies, where there is currently a lack of precise experimental measurements.

can be written as their sum [19]

$$\phi_i(E) = \sum_{j=1}^{3} a_{i,j} E^{-\gamma_{i,j}} \exp\left[-\frac{E}{Z_i R_{c,j}}\right]. \tag{2.5}$$

In figure 2.2 we show the resulting nuclei spectra when using the parameters given in the H4a model [19] shown in Table (2.1). In the final line of Table (2.1) an additional high energy component of protons was added. As of now, no direct measurements of the primary cosmic ray flux at energies above 100 TeV have been made. This allows for some freedom when extrapolating to higher energies. Compared to the discussion until now, one could assume a different rigidity or a different population count. This leads to a range of primary models such as the Gaisser-Hillas models H3a, H4a [19] and Gaisser-Tilav Gen 3 and 4 models [23]. The discrepancies appear primarily at the highest energies as shown in figure 2.3.

While indirect measurements of the primary cosmic ray flux exist, e.g. by Auger [5], the composition still has uncertainties, leaving room for the discrepancies shown in figure 2.3. When running precision simulations, these uncertainties are one of the limiting factors when making predictions.

Atmosphere

When particles pass through matter, the likelihood of them interacting (or decaying) depends on the density of the target material and its amount. To quantify the amount of material passed by the particle cascade along its path, we need to know the density of said material at each given point. For homogeneous systems, this is not difficult but in the case of Earth's atmosphere, being a variable system, requires a more in-depth treatment. Since temperature modulations in the atmosphere, caused by seasonal variance, influences the final particle fluxes measured by ground based detectors [24], we require models which represent the density at any given time and location.
As a first approximation one can use the U.S. Standard Atmosphere [25]. In this model the atmosphere is divided into layers. Each layer is assumed to have a linear temperature distribution in height h. Pressure, P and density, ρ, are then calculated by solving the pressure variation

$$\frac{\mathrm{d}P}{\mathrm{d}h} = -\rho g \tag{2.6}$$

and ideal gas law

$$P = \rho R T. \tag{2.7}$$

In the above equations R is the specific gas constant and g the standard acceleration of gravity. The U.S. Standard atmosphere extends up to 86 km. For shower simulations the atmospheric model needs to be extended further for which we adopt Braeunig's* method which uses 4th order polynomials to approximate the atmosphere. To model fluctuations due to seasonal variations in the atmosphere, experimental data or more precise models are required such as the NRLMSISE-00 [26] model or

---

* http://www.braeunig.us/space/atmmodel.htm

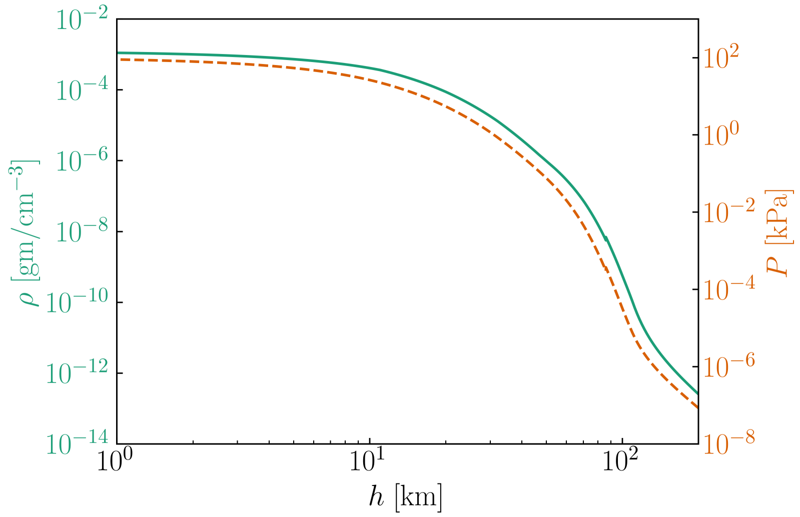

Figure 2.4: The extended U.S. Standard Atmosphere constructed for the atmospheric cascade simulations. This extended version includes heights above 86 km, based on the polynomials by Braeunig, http://www.braeunig.us/space/atmmodel.htm.

measurements by ECMWF [27]. The effect this can have is discussed in greater detail in section 3.2 and shown in figure 3.4.

Particle Interactions

The final component required to model particle cascades is an interaction model. These models usually describe hadronic interactions from a few GeV to EeV energies. The main components, relevant to most experiments are the interactions of protons, neutrons, pions and kaons. Pions (and kaons) being pseudo-Goldstone bosons, acting as mediators of the strong force, are the main interaction channel in particle cascades. While experimental data from experiments such as the LHC can be used to benchmark energies below a few TeV, no such comparison exists in the high energy regimes. Additionally, the cross sections change depending on the target material, with very little experimental data existing for air targets at high energies. For this reason discrepancies can and do appear between the interaction models. The methods used to construct the models differ from model to model, see Sibyll2.3c [28], EPOS-LHC [29], QGSJET-II [30] and DPMJET-III [31]. Here we will discuss how one can extrapolate to different targets, such as air, from experimental proton proton data. For further details see [32, 33, 34, 35]. As a starting point one can use different experimental data sets for the interactions between protons and particles [36]. An example of experimental data is shown in figure 2.5. Here we already include measurements and constraints from air shower experiments, as discussed in [32].

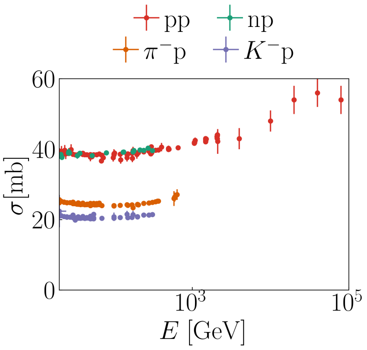

Figure 2.5: A collection of total cross sections from different experiments using proton targets from [36]. Current experimental constraints limit direct cross section measurements to a few TeV. The higher energy cross section were calculated using measurements by air shower experiments, see [37, 38] for examples

Comparing the experimental proton data to Sibyll2.3cpp, the proton target interaction model of Sibyll2.3c, results in figure 2.6. The agreement is high, as expected.

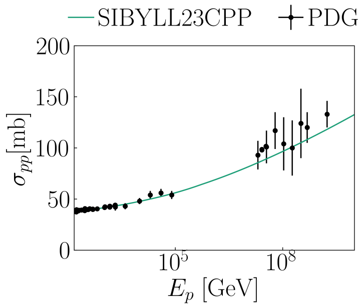

Figure 2.6: A comparison between Sibyll2.3cpp and PDG data [36, 37, 38]. The agreement is high, as expected, since experimental data is used to benchmark interaction models.

To convert a proton target cross section to ones of arbitrary material one can employ the Glauber formalism. [33, 34]. There the nucleus is treated as a closed many-particle system. Treating each interaction as a two-particle one, the overall phase shift χ_A is the sum of all two-particle ones

$$\chi_A(b, d) = \sum_{j=1}^{A} \chi_j(b - d_j). \tag{2.8}$$

Here A denotes the nucleus, the sum runs over its constituents, b is the impact parameter and d_j denotes the nucleons position in the nucleus. The scattering amplitude S is then given by

$$S(t) = \frac{1}{2\pi} \int e^{itb} \mathrm{d}^2 b \int |\psi(d)|^2 \left(1 - e^{i\chi_A}\right) \prod_{j=1}^{A} \mathrm{d}^2 d_j. \tag{2.9}$$

Since scattering can be treated as a single collision process with a single phase shift χ_{opt}

$$S(t) = \frac{i}{2\pi} \int e^{itb} \left(1 - e^{i\chi_{\mathrm{opt}}}\right) \mathrm{d}^2 b, \tag{2.10}$$

the two above equations can be combined. Assuming there are a large number of scattering centers the single phase shift becomes

$$\chi_{\mathrm{opt}}(b) = i \int \mathrm{d}^2 d \rho_A(d) \left(1 - e^{i\chi(b-d)}\right). \tag{2.11}$$

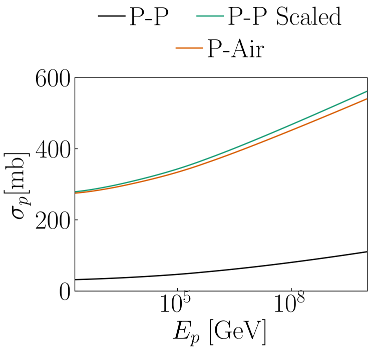

Figure 2.7: A comparison between Sibyll2.3cpp, its scaled version, using the Glaubner formalism and Sibyll2.3c.

Here ρ_A is the distribution of scattering centers. Plugging this into the definition of the cross sections

$$\sigma_{\mathrm{tot}} = 2 \int \left[1 - \mathrm{Re}\left(e^{i\chi(b)}\right)\right] \mathrm{d}^2 b, \tag{2.12}$$

$$\sigma_{\mathrm{inel}} = \int 1 - \left(e^{i\chi(b)}\right)^2 \mathrm{d}^2 b, \tag{2.13}$$

the inelastic cross section becomes

$$\sigma_{pA}^{\mathrm{inel}} = \int \mathrm{d}^2 b \left[1 - \left(1 - \sigma_{pp}^{\mathrm{tot}} \frac{\rho_A}{A}\right)^A\right]. \tag{2.14}$$

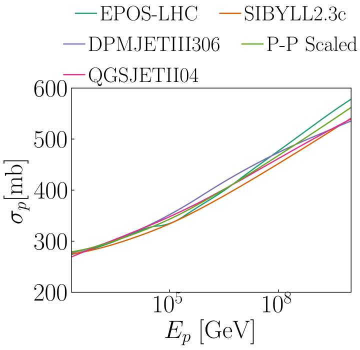

Figure 2.8: A comparison between Sibyll2.3c [28], EPOS-LHC [29], QGSJET-II [30] and DPMJET-III [31]. We have included a scaled version of Sibyll2.3cpp using the Glaubner formalism.

The nucleon distribution ρ_A can be written as [39]

$$\rho_A = \frac{\rho_0}{1 + e^{(r-c)/a}}, \tag{2.15}$$

where $c = R_A - (\pi a)^2/(3R_A)$, $R_A = 1.145A^{1/3}$ fm and $a = 0.545$ fm. Applying this scaling to the proton-proton cross section from Sibyll2.3c, we obtain the proton-air version, shown in figure 2.7.

The scaled version agrees well with the more precise calculations used in Sibyll2.3c. This methodology can be used to extrapolate data from experiments to be used for modeling particle cascades in a broad range of materials. This in turn can also be used in the inverse, to obtain proton-proton cross sections from air shower experiments [37, 38, 32]. In figure 2.8, we show a comparison between the proton-air cross section between four interaction models. The differences these make in particle air showers is discussed in section 2.2.

Later on a search for antiprotons in the cosmic ray flux is performed, see Chapter 7. For this reason we will briefly explain the main differences between $p - p$ and $\bar{p} - p$ collisions (or the lack thereof) in air shower physics.

Antiproton-Proton collisions

A cartoon of the collision between $\bar{p}$ and p is shown in figure 2.9. The only relevant difference between the two hadrons for our discussion is the inversion of their main constituents, the valence quarks. This makes the annihilation process happen more efficiently in $\bar{p} - p$ collisions, than in $p - p$ ones. As an example, the Drell-Yan process for the production of di-leptons, can now happen using the primary constituents, instead of the sea quarks

$$\bar{q}q \longrightarrow Z/\gamma^* \longrightarrow \bar{l}l. \tag{2.16}$$

Specifically, in the case of IceCube, this would mean a higher flux of highly energetic μ and ν, which could be used to differentiate between a primary p and $\bar{p}$. [40].

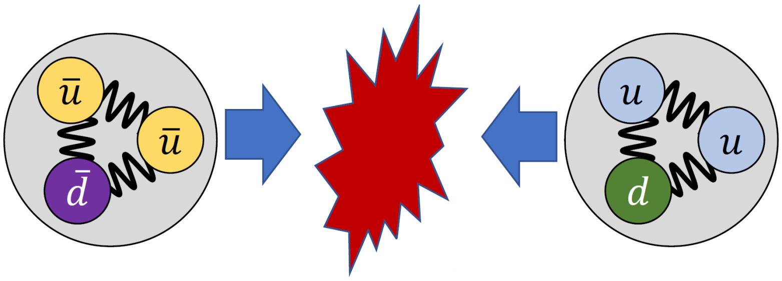

Figure 2.9: Cartoon of a $\bar{p}-p$ collision. The only relevant difference between the two hadrons, is the inversion of their valence quarks.

This only holds true for low s, while at higher center of mass energies the differences between the cross sections vanish. In Regge theory, we can write the hadronic amplitude, $\mathscr{A}$, as [41, 40]

$$\mathscr{A}(s,t) = Cs^{\alpha(M^2=t)} \pm (s \longrightarrow -s). \tag{2.17}$$

Here M is the mass of the bound states and α is the meson's trajectory. The last term is a signature factor. The amplitude is then the sum over all bound states. From observations we know that meson trajectories behave linearly

$$\alpha(M^2) = \alpha_0 + \alpha' M^2, \tag{2.18}$$

with α_0 and α' being the intercept and slope respectively. Using the optical theorem, we can relate the total cross section to the amplitude

$$\mathrm{Im}\mathscr{A}(s, t = M^2 = 0). \tag{2.19}$$

The most relevant trajectories have approximately $\alpha_0 \approx -0.5$, leading to the cross section dropping as $1/\sqrt{s}$. From experimental measurements we know the cross sections start rising again, leading to the introduction of a new component, the pomeron. For the purposes of this illustration, we assume two Regge trajectories and an additional pomeron component [41, 42]

$$\sigma(s) = \mathrm{Im}\mathscr{A}(s,0) = \pm(-28.2\ \mathrm{mb})s^{-0.51} + (56.2\ \mathrm{mb})s^{-0.324} + (18.2\ \mathrm{mb})s^{0.095}. \tag{2.20}$$

For low energies the first two terms will dominate the cross section, while for higher energies the last term (pomeron) will be the most relevant part. The sign of the first term changes, depending on whether the particle of interest is a proton (+) or an antiproton (−). A comparison of this model and the experimental measurements collected by PDG [36] is

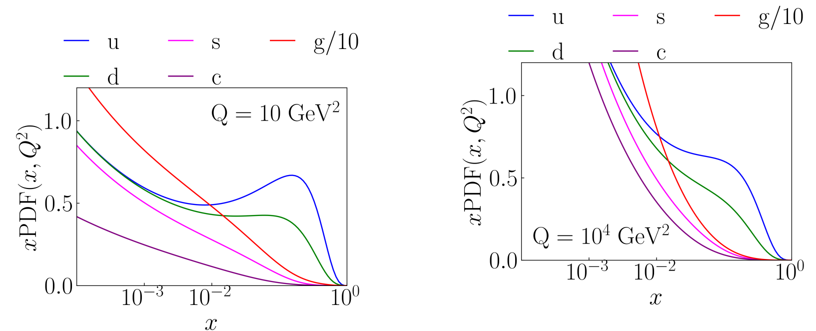

(a) The parton distribution functions at 10 GeV according to CT10 [43] using LHAPDF [44]. The peak in the u and d distributions are due to them being the valance quarks of the proton.

(b) The parton distribution functions at 10 TeV according to CT10 [43] using LHAPDF [44]. Proportionally the valence quarks make up less of the distribution space. This means interactions with gluons and sea quarks are more likely when compared to the plot on the left.

Figure 2.10: The proton PDFs at 10 GeV and 10 TeV

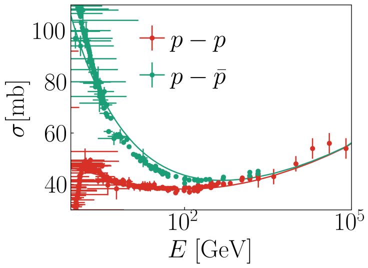

Figure 2.11: A collection of total cross sections from different experiments for protons and antiprotons using proton targets targets from [36]. Included is a fit using Regge and Pomeron theory.

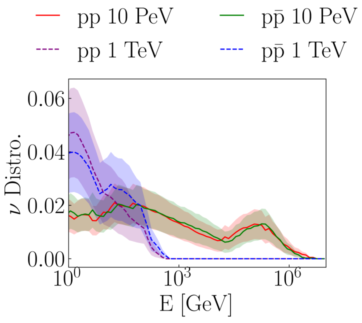

Figure 2.12: The neutrino energy spectra in pp and $p\bar{p}$ collisions, when only simulating weak interactions. The shaded regions denote the 1σ error regions. At low energies, there is a very slight difference between the two collision types. At higher energies any difference vanishes.

shown in figure 2.11. Physically pomeron exchange may correspond to the exchange of glueballs. Generalizing this, leads to the Pomeranchuk's theorem that the ratio of this cross section goes to one

$$\frac{\sigma_{pp}}{\sigma_{\bar{p}p}} \rightarrow 1, s \rightarrow \infty. \tag{2.21}$$

It is also generally accepted that this also holds for the inclusive cross sections and multiplicities. This can be understood by comparing the parton distribution functions (pdfs). In our current understanding the pdfs for the gluons and quarks in the quark sea are the same for particle and antiparticle, with only the valence quarks differing. In figure 2.10 we show the proton's pdf at 10 GeV (left) and 10 TeV (right). The pdfs are plotted using x, which is the energy fraction the parton carries. With increasing energy the relevance of the gluons and quark sea increases. At very high energies, only for very high x are the valence quarks relevant, making the difference between protons and antiprotons negligible. To make sure, that there is no difference in the produced spectra of neutrinos between $p - p$ and $\bar{p} - p$ collisions we ran a PYTHIA 8.3 [45] of 100000 collisions of the two types.

In figure 2.12 we show the resulting neutrino spectra from pp and $p\bar{p}$ collisions at 1 TeV and 10 PeV. There is a very slight difference between the two at low energies, which vanishes for higher energies. This difference, at low energies, is enhanced when looking at the production of ν_τ which could be exploited by low energy experiments.

In figure 2.13 we show the resulting spectra when simulating all interactions. There is no relevant difference between the two collision types. This means neutrinos do not offer a channel for differentiating between the two species. For this reason it is difficult to use IceCube to measure the antiproton flux or differentiate between proton and antiproton air showers.

With all the necessary components required to model atmospheric particle showers, we will now proceed to introduce cascade equations and the numerical tools required to solve them.

2.2 Cascade Equations

There are multiple approaches to simulating particle cascades in materials or the atmosphere. For example, CORSIKA [46] and EGS5 [47] employ Monte Carlo methods, simulating particle interactions on an event by event basis. Here we focus on and employ cascade equations [21, 48, 49], similar to CONEX [50] and MCEq [51].

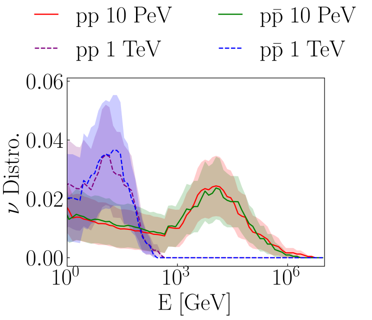

Figure 2.13: The neutrino energy spectra in pp and $p\bar{p}$ collisions, when simulating all interactions. The shaded regions denote the 1σ error regions. There is no difference between the two collision types.

Assuming a particle flux, ϕ, which is defined to be

$$\phi = \frac{\mathrm{d}N}{\mathrm{d}A\mathrm{d}\Omega\mathrm{d}t}\left[\mathrm{cm}^{-2}\mathrm{sr}^{-1}\mathrm{s}^{-1}\right], \tag{2.22}$$

where it is usual to use the differential flux

$$\Phi = \frac{\mathrm{d}\phi}{\mathrm{d}E}, \tag{2.23}$$

we wish to propagate it through a target material. To this end we solve the transport equation in one dimension, dubbed cascade equations for a particle h

$$\begin{aligned}\frac{\mathrm{d}\Phi_h(E,X)}{\mathrm{d}X} &= -\frac{\Phi_h(E,X)}{\lambda_{int,h}(E)} - \frac{\Phi_h(E,X)}{\lambda_{dec,h}(E,X)} - \frac{\partial}{\partial E}\left(\mu(E)\Phi_h(E,X)\right) + \\ &+ \sum_l \int_E^\infty \mathrm{d}E_l \frac{\mathrm{d}N_{l(E_l)\to h(E)}}{\mathrm{d}E}\frac{\Phi_l(E_l,X)}{\lambda_{int,l}(E_l)} + \sum_l \int_E^\infty \mathrm{d}E_l \frac{\mathrm{d}N^{dec}_{l(E_l)\to h(E)}}{\mathrm{d}E}\frac{\Phi_l(E_l,X)}{\lambda_{dec,l}(E_l,X)}.\end{aligned} \tag{2.24}$$

where Φ is the particle flux, X is the slant-depth, E the energy, N the particle number and the λ are interaction or decay lengths. The slant-depth is defined as

$$X(h_0) = \int_0^{h_0} \rho(h)\mathrm{d}h. \tag{2.25}$$

This choice of "distance parameter" is made to factor out the density dependence of the equation. The slant depth as a parameter gives an estimate of the amount of material passed by the particle flux, a more relevant value than the actual distance. The terms of equation 2.24 represent the following:

- $-\frac{\Phi_h(E,X)}{\lambda_{int,h}(E)}$ represents the absorption of the particles due to the interaction with nuclei in the material.
- $-\frac{\Phi_h(E,X)}{\lambda_{dec,h}(E,X)}$ represent the decay of the particles.
- $-\frac{\partial}{\partial E}\left(\mu(E)\Phi_h(E,X)\right)$ represents continuous losses due to radiation, ionization etc. The energies scales appearing in this term are of the order MeV and at the energies of interest ($>$ 50GeV) are at most sub-leading. For low energies and high inclinations this term cannot be neglected. Additionally, the shower shape and maximum is sensitive to ionzation losses due to low energy particles and interactions dominating its shape.
- The final two source terms represent the production of particles due to interaction and decay, respectively. The lower limit of the integrals is due to energy conservation.

The energy distributions in the source terms $\mathrm{d}N/\mathrm{d}E$ can be calculated with

$$\frac{\mathrm{d}N_{j(E_j)\to i(E)}}{\mathrm{d}E} = \frac{1}{\sigma_j(E_j)} \frac{\mathrm{d}\sigma_{j\to i}(E, E_j)}{\mathrm{d}E}. \tag{2.26}$$

In the above equation $\sigma_j(E_j)$ is the inclusive cross-section for the interactions with the background material of a particle of type j with energy E_j. To calculate the interaction length one needs to use the cross section for absorptive processes [21]

$$\sigma_{abs} = \frac{1}{\Phi_a} \frac{\mathrm{d}N_{abs}}{\mathrm{d}t}. \tag{2.27}$$

Here Φ_a is the flux of incoming particles a and $\mathrm{d}N_{abs}/\mathrm{d}t$ is the rate of the absorption processes. The above equation is only valid for a single target particle, b. In this case one needs to know how many particles the incoming flux meets, which is calculated using

$$\mathrm{d}N_b = \frac{\rho_b}{m_b} \mathrm{d}A\mathrm{d}l, \tag{2.28}$$

where ρ_b is the mass density of the target material and m_b the particle mass. In the relativistic case $\mathrm{d}l = \beta c \mathrm{d}t$. Multiplying the above equations and plugging in the relativistic contraction results in

$$\frac{\mathrm{d}N_{abs}}{\mathrm{d}t} = \sigma_{abs} \frac{\rho_b}{m_b} \Phi_a \mathrm{d}A\mathrm{d}l. \tag{2.29}$$

Hence the flux is

$$\frac{\mathrm{d}\Phi_a}{\mathrm{d}l} = -\frac{\mathrm{d}}{\mathrm{d}l} \left(\frac{\mathrm{d}^2 N_{abs}}{\mathrm{d}A\mathrm{d}t} \right) = -\sigma_{abs} \frac{\rho_b}{m_b} \Phi_a. \tag{2.30}$$

Using the differential slant depth X from equation 2.25

$$\mathrm{d}X = \rho_b \mathrm{d}l, \tag{2.31}$$

we obtain the loss term due to interactions from equation 2.24

$$\frac{\mathrm{d}\Phi_a}{\mathrm{d}X} = -\frac{\sigma_{abs}}{m_b} \Phi_a = -\frac{1}{\lambda_{abs}} \Phi_a. \tag{2.32}$$

Here $\lambda_{abs} = m_b/\sigma_{abs}$ is the interaction length. Note that $m_b = A/N_A$, where A is the atomic mass and N_A is Avogadro's constant. Should one model electromagnetic cascades, as we will in this thesis, the terms including d_{dec} in equation 2.24 can be dropped.

Example Application

To understand the cascade equation approach, we give an example calculation for the muon and neutrino production in the atmosphere and the sun. This illustrates the necessary components and how this approach can be used to quickly estimate particle fluxes. We assume the initial flux is primarily composed of protons and follows a single power-law distribution of the form

$$\phi_p(E, X) = \phi_0 E^{-\gamma}. \tag{2.33}$$

ϕ_0 is a constant flux normalization and γ describes the spectrum's energy dependence. Applying the cascade equation approach, the proton flux change after passing through a thin target with thickness $\mathrm{d}X$ is written as

$$\frac{\mathrm{d}\phi_p}{\mathrm{d}X} = -\frac{\phi_p(E,X)}{\lambda_{\mathrm{int,p}}(E)} + \int_E^\infty \mathrm{d}E_p \frac{\mathrm{d}N^{\mathrm{int}}_{p(E_p)\to p(E)}}{\mathrm{d}E} \frac{\phi_p(E_p,X)}{\lambda_{\mathrm{int,p}}(E_p)}. \tag{2.34}$$

Here $\lambda_{\mathrm{int,p}}$ describes the proton's interaction length and $\frac{\mathrm{d}N^{\mathrm{int}}_{p(E_p)\to p(E)}}{\mathrm{d}E}$ the rate of proton production by higher energetic protons. For simplification we assume protons are exclusively produced in interactions between protons and the material's nuclei. Assuming Feynman scaling, equation 2.34 and the primary flux from equation 2.33 can be simplified

$$\begin{aligned}\frac{\mathrm{d}\phi_p}{\mathrm{d}X} &= \frac{\phi_0}{\lambda_{\mathrm{int,p}}(E)}\left[-E^{-\gamma} + \int_E^\infty \mathrm{d}E_p \frac{\mathrm{d}N^{\mathrm{int}}_{p(E_p)\to p(E)}}{\mathrm{d}E} E^{-\gamma}\right] \\ &= -\frac{\phi_0}{\lambda_{\mathrm{int,p}}(E)} E^{-\gamma}\left[1 - \int_0^1 \mathrm{d}x_{\mathrm{Lab}} \frac{\mathrm{d}N^{\mathrm{int}}_{p\to p}}{\mathrm{d}X_{\mathrm{Lab}}} x_{\mathrm{Lab}}^{\gamma-1}\right] \\ &= -\frac{\phi_0}{\lambda_{\mathrm{int,p}}(E)} E^{-\gamma}\left[1 - Z_{pp}\right].\end{aligned} \tag{2.35}$$

Here Z_{pp} is called the *spectrum-weighted moment* [21]. These kernels describe the inclusive production of particles. The above equation is a linear first order differential equation and together with the power law *ansatz* from equation 2.33 the solution is

$$\phi_p(E,X) = \phi_0 \exp\left(-\frac{X}{\lambda_{\mathrm{int,p}}}(1 - Z_{pp})\right) E^{-\gamma} = \phi_0 \exp\left(-\frac{X}{\Lambda_p}\right) E^{-\gamma}, \tag{2.36}$$

if the energy scaling of the interaction length is neglected. For most cases this is a valid approximation, due to the low scaling of the interaction length with energy. We can infer from this result that the flux of nucleons follows the primary's spectral shape, due to the only difference being new or additional kernel terms Z_{ij}. For simplification we denote $\frac{\lambda_{\mathrm{int,p}}}{1-Z_{ii}}$ as Λ_i.

While mesons, such as pions, can be treated similarly as nucleons, some additional terms need to be accounted for in their propagation. First, mesons can be produced in interactions involving nucleons and mesons with the medium. Secondly, mesons can decay, producing other secondaries. The cascade equation with the addition of these two terms becomes

$$\frac{\mathrm{d}\phi_\pi}{\mathrm{d}X} = -\phi_\pi(E,X)\left[\frac{1}{\Lambda_\pi} + \frac{\epsilon_\pi}{EX\cos(\theta)}\right] + \frac{\phi_p(E,X)}{\lambda_{\mathrm{int,p}}} Z_{p\pi}. \tag{2.37}$$

Here we approximated the decay length of the pion, $\lambda_{\mathrm{dec},\pi}(E,X)$ as $\frac{EX\cos(\theta)}{\epsilon_\pi}$ with ϵ_π being the characteristic decay constant and θ the zenith angle of the incoming primary flux [52]. To solve this equation we differentiate between two extreme cases. One where the pion decay is irrelevant and one where it is dominant. In the interaction dominated case the solution of the ODE is

$$\phi_\pi(E,X) = \phi_0 \frac{Z_{p\pi}}{1-Z_{pp}} \frac{\Lambda_\pi}{\Lambda_p - \Lambda_\pi} \left[\exp\left(-\frac{X}{\Lambda_\pi}\right) - \exp\left(-\frac{X}{\Lambda_p}\right)\right] E^{-\gamma}. \tag{2.38}$$

Once again the flux follows the same spectral shape as the injected one. Contrary to this, in the decay dominated case the solution is

$$\phi_\pi(E,X) = \frac{\phi_0 \cos(\theta)}{\epsilon_\pi} \frac{Z_{p\pi}}{\lambda_{\mathrm{int,p}}} \exp\left(-\frac{X}{\Lambda_p}\right) X E^{-\gamma+1}. \tag{2.39}$$

Thus when decays dominate, the energy dependence is one power of energy harder. The production of muons from mesons (kaons would be treated in a similar fashion) is then described by the following equation

$$\frac{\mathrm{d}\phi_\mu}{\mathrm{d}X} = -\frac{\phi_\mu}{\lambda_{\mathrm{int},\mu}} - \frac{\phi_\mu}{\lambda_{\mathrm{dec},\mu}} + \int_E^\infty \mathrm{d}E_\pi \frac{\mathrm{d}N^{\mathrm{dec}}_{\pi\to\mu}}{\mathrm{d}E} \frac{\phi_\pi}{\lambda_{\mathrm{dec},\pi}}. \tag{2.40}$$

Pions predominantly decay into a muon and muon neutrino pair [52], with most of the energy transferred to the muon. This can be approximated by setting

$$\frac{\mathrm{d}N^{\mathrm{dec}}_{\pi\to\mu}}{\mathrm{d}E} \approx \delta(a_\mu E_\pi - E), \tag{2.41}$$

with a_μ describing the transferred energy fraction. Depending on the medium of interest a combination of the first two terms in equation 2.40 can be neglected. Here we discuss two examples, namely in Earth's atmosphere and in the Sun's. In both cases the density of the background material is low enough, that the interaction term can be neglected. A high energy muon can on average travel further than 50 km before it decays, hence the decay term can be neglected for most detectors in the Earth's atmosphere. Thus equation 2.40 becomes

$$\frac{\mathrm{d}\phi_\mu}{\mathrm{d}X} = \frac{\phi_\pi(E/a_\mu, X)\epsilon_\pi}{X\cos(\theta)E/a_\mu}, \tag{2.42}$$

for muons in Earth's atmosphere. Plugging in the two cases of interaction or decay dominated pion production the muon spectra follow the power laws of

$$\phi_\mu^{\mathrm{int,Earth}}(E,X) \propto E^{-(\gamma+1)} \tag{2.43}$$

and

$$\phi_\mu^{\mathrm{decay,Earth}}(E,X) \propto E^{-\gamma} \tag{2.44}$$

respectively. The change in exponent is due to the efficiency of energy transfer, when one compares interactions and decays with interactions being the less efficient channel.

In the case of the solar atmosphere, the muon decay can not be neglected, since we expect all muons to decay before reaching the Earth. Solving the ODE, the resulting energy spectra for muons in the interactions and decay cases are

$$\phi_\mu^{\mathrm{int,Sun}}(E,X) \propto E^{-\gamma} \tag{2.45}$$

and

$$\phi_\mu^{\mathrm{decay,Sun}}(E,X) \propto E^{-\gamma+1} \tag{2.46}$$

respectively. The neutrino spectra, since they are produced by the decay of pions and muons, will then approximately follow their parents energy spectra. The previous calculations show that with relatively simple assumptions, we can already estimate the energy dependence of particle fluxes using cascade equations. The method does not reproduce the stochastic nature of single interactions, nor low energy effects making it unusable for single shower simulations and low energy calculations. For average flux calculations and high energies though, such as is the case for neutrino detectors, this methodology provides a fast and efficient flux model. The other approach is using Monte Carlo methods, such as in the tool WimpSim [53], which can prove to be computationally expensive. Figure 2.14 shows the results when using the previously described method for the Sun's and Earth's atmospheric neutrino fluxes. These are similar to those calculated by the WimpSim authors.

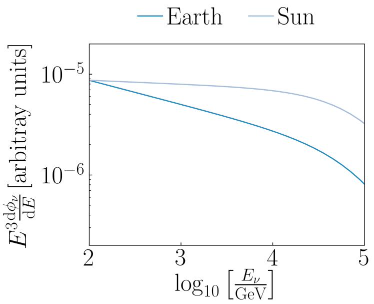

Figure 2.14: Example of the calculated neutrino fluxes from the solar atmosphere (light blue) and earth's (dark blue). Here the method described in this section was used to estimate the particle fluxes. Due to undefined normalization factors, the flux has arbitrary units. The primary particle model used here is H4a [19]. One can clearly see the difference in energy dependence between the two. This difference can for example be utilized by neutrino telescopes to measure the solar atmospheric neutrino flux.

This fast approach proves extremely useful for theoretical modelling and estimation. From the few lines of calculations shown here, we have calculated the fluxes in figure 2.14, motivating a search for a solar atmospheric neutrino flux which was done in [54]. This example shows the power of this methodology to estimate backgrounds and signals in neutrino, gamma ray and cosmic ray experiments. In Chapter (6) we will show what is possible using this approach, when using a full numerical framework.

Matrix Form

To make the solving of the cascade equations less computationally expensive, we discretize the energy grid logarithmically

$$E_i = E_0 \cdot 10^{d_i}. \tag{2.47}$$

This descretization requires an appropriate discretizaion of the individual terms in the cascade equation, while upholding momentum and energy conservation. To this end we introduce some additional definitions

- State vector: $\vec{\Phi} = \left(\vec{\Phi}^p\ \vec{\Phi}^n\ \vec{\Phi}^{\pi^+} ...\right)^T$. This state vector includes the state of each particle species used in the calculation.
- Each state: $\vec{\Phi}^p = \left(\Phi^p_{E_0}\ \Phi^p_{E_1}\ ...\ \Phi^p_{E_N}\right)^T$. These are the discretized fluxes of the particles of interest at the energies given by the logarithmic energy grid.
- Interaction coefficient: $c_{l(E_l)\to h(E_h)} = \Delta E_l \frac{\mathrm{d}N_{l\to h}(E_l)}{\mathrm{d}E_h}(E_h)$. These coefficients are defined using the average production rate given the parent's energy bin E_l and the child's E_h. ΔE_l is the parent's bin width.
- Decay coefficient: $d_{l(E_l)\to h(E_h)} = \Delta E_l \frac{\mathrm{d}N^{dec}_{l\to h}(E_l)}{\mathrm{d}E_h}(E_h)$. These coefficients are defined using the average production rate given the parent's energy bin E_l and the child's E_h. ΔE_l is the parent's bin width.

Using these definitions and neglecting the energy loss term we can rewrite the cascade equation 2.24 to

$$\begin{aligned}\frac{\mathrm{d}\Phi^h_{E_i}}{\mathrm{d}X} = &-\frac{\Phi^h_{E_i}}{\lambda^h_{int,E_i}} + \sum_{E_k\geq E_i}^{E_N}\sum_l \frac{c_{l(E_l)\to h(E_h)}}{\lambda^l_{int,E_k}}\Phi^{\vec{l}}_{E_k} \\ &-\frac{\Phi^h_{E_i}}{\lambda^h_{dec,E_i}(X)} + \sum_{E_k\geq E_i}^{E_N}\sum_l \frac{d_{l(E_l)\to h(E_h)}}{\lambda^l_{dec,E_k}}\Phi^{\vec{l}}_{E_k},\end{aligned} \tag{2.48}$$

where the summations run over the energy bins and particle species. As a next step we wish to remove the summation by rewriting the above equation into a matrix form. To this end, we arrange the interaction lengths λ_{int} into a diagonal matrix

$$\Lambda_{int} = \mathrm{diag}\left(\frac{1}{\lambda^p_{int,E_0}} \dots \frac{1}{\lambda^p_{int,E_N}}, \frac{1}{\lambda^n_{int,E_0}} \dots \frac{1}{\lambda^n_{int,E_N}}, \frac{1}{\lambda^{\pi^+}_{int,E_0}} \dots \frac{1}{\lambda^{\pi^+}_{int,E_N}}, \dots\right) \tag{2.49}$$

We can rewrite the decay lengths in the same way by factoring out the density $\lambda_{dec} = \rho(X)\tilde{\lambda}_{dec}$

$$\Lambda_{dec} = \mathrm{diag}\left(\frac{1}{\tilde{\lambda}^p_{dec,E_0}} \dots \frac{1}{\tilde{\lambda}^p_{dec,E_N}}, \frac{1}{\tilde{\lambda}^n_{dec,E_0}} \dots \frac{1}{\tilde{\lambda}^n_{dec,E_N}}, \frac{1}{\tilde{\lambda}^{\pi^+}_{dec,E_0}} \dots \frac{1}{\tilde{\lambda}^{\pi^+}_{dec,E_0}}, \dots\right) \tag{2.50}$$

As a final step we rearrange the interaction and decay coefficients into interaction and decay matrices

$$\vec{C}_{l\to h} = \begin{pmatrix} c_{l(E_0)\to h(E_0)} & \dots & \dots & c_{l(E_0)\to h(E_N)} \\ 0 & c_{l(E_1)\to h(E_1)} & \dots & c_{l(E_1)\to h(E_N)} \\ 0 & \dots & \dots & \dots \\ 0 & \dots & 0 & c_{l(E_N)\to h(E_N)} \end{pmatrix}, \tag{2.51}$$

and

$$\vec{D}_{l\to h} = \begin{pmatrix} d_{l(E_0)\to h(E_0)} & \dots & \dots & d_{l(E_0)\to h(E_N)} \\ 0 & d_{l(E_1)\to h(E_1)} & \dots & d_{l(E_1)\to h(E_N)} \\ 0 & \dots & \dots & \dots \\ 0 & \dots & 0 & d_{l(E_N)\to h(E_N)} \end{pmatrix}. \tag{2.52}$$

Note that the matrices are diagonal due to energy conservation, $E_l \geq E_h$. The total coupling matrix for the c couplings $\vec{C}$ (and similarly for $\vec{D}$) is then

$$\vec{C} = \begin{pmatrix} \vec{C}_{p\to p} & \vec{C}_{n\to p} & \vec{C}_{\pi^+\to p} & \dots \\ \vec{C}_{p\to n} & \vec{C}_{n\to n} & \vec{C}_{p\to \pi^+} & \dots \\ \vec{C}_{\pi^+\to p} & \vec{C}_{\pi^+\to n} & \vec{C}_{\pi^+\to \pi^+} & \dots \\ \dots & \dots & \dots & \dots \end{pmatrix}. \tag{2.53}$$

Together the resulting cascade equation is

$$\frac{\mathrm{d}}{\mathrm{d}X}\vec{\Phi} = \left[(-\vec{1} + \vec{C})\vec{\Lambda}_{int} + \frac{1}{\rho(X)}(-\vec{1} + \vec{D})\vec{\Lambda}_{dec}\right]\vec{\Phi}. \tag{2.54}$$

This form lends itself to fast and efficient ODE solving, since now the coupled differential equation can be treated as a matrix multiplication. This lends itself, assuming the necessary stability of the system, to using simple explicit Euler methods when solving the equation. The stability of the equations are defined by the interaction lengths of the particles. In figure 2.15 we show the interaction lengths of the two most relevant particles in hadronic particle showers, the pion and kaon. Since the interaction and decay lengths give a measure of how far these particles travel on average before interacting or decaying, these values approximately correspond to the allowed step size when solving the differential equation. Note that at high energies the interaction lengths are far lower than the decay lengths. For this reason, for the purpose of modeling hadronic cascades, pions and kaons are quasi stable particles and fluxes from these particles are dubbed conventional. Particle fluxes produced by heavier mesons, with charm components or heavier, are dubbed prompt component.

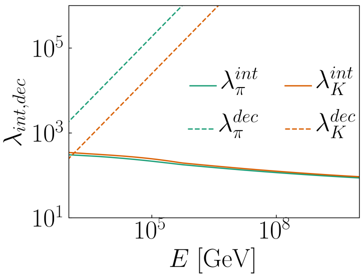

Figure 2.15: Here we show the interaction lengths of the main drivers of hadronic cascades, the pion and kaon. Their interaction lengths define the stability of the equation system and the step sizes allowed for precise solving of the cascade equations.

Method of Moments

To uphold particle number and energy conservation after discretizing the differential equation we employ the Method of Moments [55]. This entails calculating the appropriate particle flux when injecting single particles or calculating the correct averages for the production rates. Here we give a brief overview of the Method of Moments.
Let X be a random variable. The expectation value of functions, g, of X can be calculated, using the pdfs $f_Y(y)$ of Y with $Y = g(X)$

$$E_g(X) = EY = \int_{-\infty}^{\infty} y f_Y(y) \mathrm{d}y. \tag{2.55}$$

The n-th central moment μ_n, of X (or $F_X(x)$) is

$$\mu_n = E(X - \mu)^n, \tag{2.56}$$

where $\mu = EX$. Note that the second central moment of X is its variance $\mathrm{Var}X = E(X - EX)^2$. In EmCa the second moment method is used, to uphold particle numbers and energy conservation. Here we show how this applies to injecting discrete particles into the cascade equation. First the moments per particle in the three bins around the initial particles' energies are calculated. This is used to construct a matrix E_{mom}

$$E_{mom} = \begin{pmatrix} \Delta E_{i-1} & \Delta E_i & \Delta E_{i+1} \\ E_{i-1}\Delta E_{i-1} & E_i \Delta E_i & E_{i+1}\Delta E_{i+1} \\ E_{i-1}^2 \Delta E_{i-1} & E_i^2 \Delta E_i & E_{i+1}^2 \Delta E_{i+1} \end{pmatrix}, \tag{2.57}$$

where ΔE_i denotes the bin width and i is the bin number in which the single particle's energy would lie. Next, the moments of the initial particles are calculated and denoted as b

$$b = \begin{pmatrix} N \\ N E_{prim} \\ N E_{prim}^2 \end{pmatrix}, \tag{2.58}$$

where N is the primary particle number and E_{prim} their energy. As a final step to calculate the initial equivalent flux, ϕ_0, the equation

$$\phi_0 = E_{avg} b, \tag{2.59}$$

is solved.

For hadronic cascades all of these components are dealt with in the python package MCEq [51]. In figure 2.16 we show an example simulation result using this package for the surface above the IceCube detector. For historical reasons we have split the components into conventional (from pions and kaons) and prompt (heavier mesons) components. Note that the spectrum of the prompt component is harder than that of the conventional one. This is a result we have already seen in the analytical example in section 2.2. There and here, the decay components have harder spectra than those from particle interactions. For this reasons, particle with charm components, which decay instantly for the purposes of cascade modeling, are treated separately from pions and kaons, which are quasi stable. Figure 2.16 shows the typical result used for background and signal calculations by IceCube and other muon and or neutrino detectors. In the next chapter we will discuss how such calculations can be used in an experimental analysis using BOREXINO data. Afterwards we will show new improvements to the current modeling scheme by introducing a new model for the electromagnetic particle cascades, improving the precision of flux calculations. Afterwards we will discuss two new types of searches made possible by precise cascade modeling.

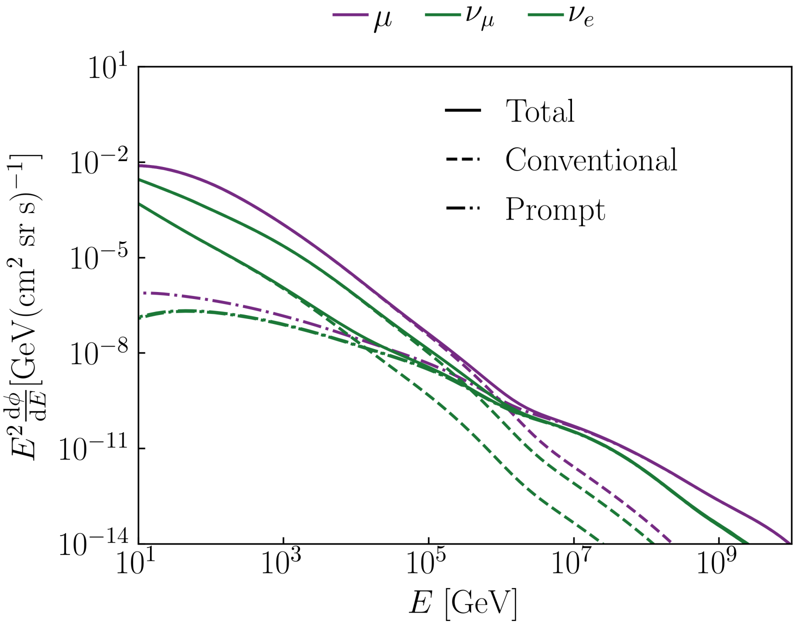

Figure 2.16: The muon and neutrino particle fluxes above the IceCube detector, simulated using MCEq [51]. We split the components into the historical prompt and conventional components. The latter of which is produced by pions and kaons and the other by heavier mesons.

Modulation of the Cosmic Muon Signal in Ten Years of Borexino Data

3

3.1 Introduction 19
3.2 Parametrization 19
3.3 BOREXINO 20
3.4 Results 20
3.5 Conclusion 22

3.1 Introduction

The modulation of neutrino and muon fluxes have been studied by IceCube [56, 57], MACRO [58], LVD [59] and other experiments. In this Chapter we describe a new analysis performed on ten years of Borexino data [60] with a primary focus on how the theoretical calculations described in the previous chapter were used.
We expect a modulation of the atmospheric muon flux due to temperature changes in the course of a year, causing density shifts in the atmosphere. This directly effects the slant depth variable, X in equation 2.24, increasing or decreasing the maximum value depending on the density change. Using MCEq [51], which employs cascade equations, we can calculate the expected muon flux changes above the IceCube detector, shown in figure 3.1. There we see changes of up to 20% between the different months. The atmosphere above IceCube is more volatile than above Gran Sasso, having larger changes in the temperature. For this reason we expect smaller seasonal variations at the BOREXINO detector.

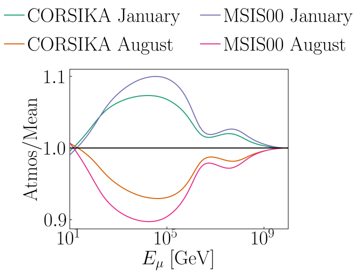

Figure 3.1: The seasonal flux change of muons when compared to the US Standard atmosphere [25] using the model employed by CORSIKA [46] and the NRLMSISE-00 [26, 63] model for different months.

3.2 Parametrization

These shifts in particle flux are typically parametrized using an effective temperature T_{eff}. Following [61, 21, 62] the muon flux for energies above 100 GeV can be parametrized as

$$\phi_\mu(E_\mu, \theta) = \phi_N(E_\mu)\left(\frac{A_\pi}{1 + B_\pi \cos\theta E_\mu/\epsilon_\pi} + \frac{A_K}{1 + B_K \cos\theta E_\mu/\epsilon_K}\right). \tag{3.1}$$

Here ϕ_N is the primary flux of nucleons. The first term corresponds to the production by pions and the second one by kaons. Other sources, such as heavier mesons are neglected. A and B are constants defined by the branching ratio, while $\epsilon_{\pi,K}$ are the characteristic critical energies discussed in section 2.2. Reflecting the results from the cascade equations, when $E_{\pi,K} < \epsilon_{\pi,K}/\cos\theta$ the meson decay is the dominant process and muons are produced with the same spectral index as the cosmic rays. At higher energies interactions dominate and the resulting spectrum is one power steeper. These critical energies depend on the density of the medium, thus the temperature. A correlation coefficient, α between the temperature, energy and muon flux is then defined as

$$\alpha_\mu(E_\mu, \theta) = \frac{T}{\phi_\mu(E_\mu, \theta)} \frac{\partial \phi_\mu(E_\mu, \theta)}{\partial T}. \tag{3.2}$$

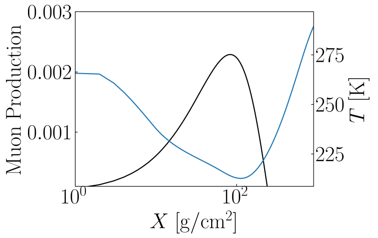

Figure 3.2: The muon production spectrum above BOREXINO using MCEq and NRLMSISE-00. These are the functions used in the calculation of T_{eff} in equation 3.4

This coefficient is then used to correlate the effective temperature T_{eff} with the muon rate, R_μ, change

$$\frac{\Delta R_\mu}{\langle R_\mu \rangle} = \alpha_T \frac{\Delta T_{\text{eff}}}{\langle T_{\text{eff}} \rangle}. \tag{3.3}$$

Note that for true detector rates the effective area needs to be folded into the definition of α. The effective temperature T_{eff} is then defined as

$$T_{\text{eff}}(E, \theta) = \frac{\int \mathrm{d}X P_\mu(E, \theta, X) T(X)}{\int \mathrm{d}X P_\mu(E_\mu, \theta, X)}. \tag{3.4}$$

Here X is the slant depth and P_μ the muon production spectrum. In figure 3.2 we show an example of the functions used to calculate T_{eff}.

While the effective temperature is insensitive to the ratio between kaons and pions, α is not. For this reason one can use seasonal modulations to measure the kaon to pion ratio.

3.3 BOREXINO

In the case of BOREXINO, which is a deep underground detector, only muons above a certain threshold energy, E_{thr} will reach the detector. Using the transformations shown in [64], equation 3.2 can be written as

$$\alpha_\mu(E_\mu, \theta) = \frac{E_{\text{thr}}}{\phi_\mu(E_\mu, \theta)} \frac{\partial \phi_\mu(E_\mu, \theta)}{\partial E_{\text{thr}}} - \gamma. \tag{3.5}$$

Here γ is the spectral index of the primary spectrum, when assuming a single power law. Inserting the parametrization from equation 3.1, we can write α as

$$\alpha_\mu(E_\mu, \theta) = \frac{1}{D_\pi} \frac{1/\epsilon_K + A_K (D_\pi/D_K)^2/\epsilon_\pi}{1/\epsilon_K + A_K (D_\pi/D_K)/\epsilon_\pi} \tag{3.6}$$

where we have used parametrizations from [64, 58] to make them specific for the surface above BOREXINO. This entails setting $E_\mu \approx E_{\text{thr}}$ and the primary spectrum to $\propto E_{\text{thr}}^{-\gamma}$. Here $D_{\pi,K}$ are defined as

$$D_{\pi,K} = \frac{\gamma}{\gamma+1} \frac{\epsilon_{\pi,K}}{1.1 \langle E_{\text{thr}} \cos\theta \rangle}. \tag{3.7}$$

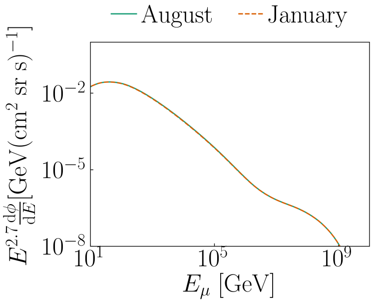

Figure 3.3: The atmospheric muon flux above BOREXINO modeled using MCEq [51] and the ECMWF dataset [27]. There is barely a noticeable difference between the months.

3.4 Results

The usually employed Monte Carlo simulations used by BOREXINO use ECMWF atmospheric data [27]. We added an interface to MCEq, so that the calculations can be compared. Running MCEq to model the atmospheric muon flux for August and January we obtain figures 3.3 and 3.4. The relative amplitude of the months are approximately 1%, depending on the energy of interest. When compared to the experimental results from [60] of 1.3% this agrees very well. When compared to figure 3.1 where we compare the seasonal changes above IceCube, the changes are minimal. This is due to the comparatively stable atmosphere in Europe, when compared to the south pole.

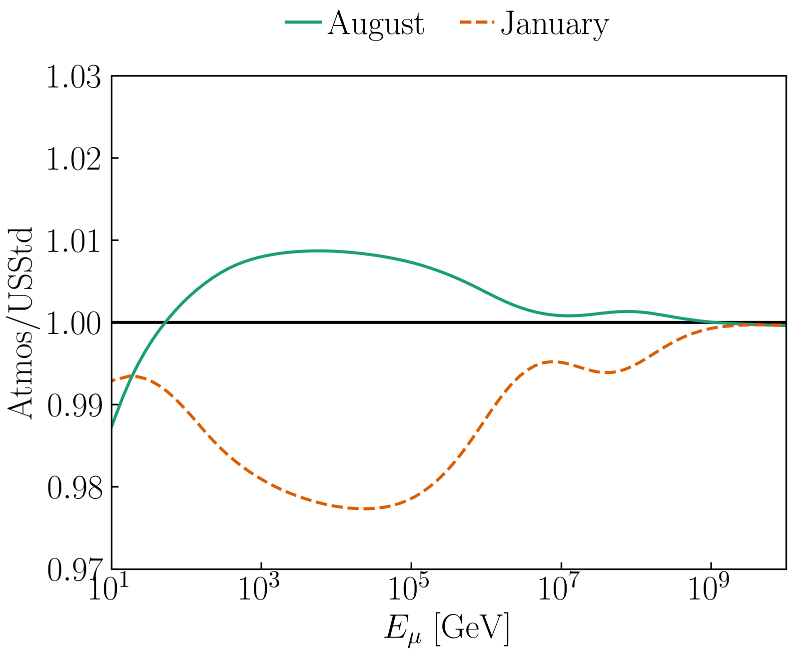

Figure 3.4: The atmospheric muon flux above BOREXINO modeled using MCEq [51] and the ECMWF dataset [27]. Here we show the changes between the months when compared to the US Standard model [25]. The relative differences of each month are approximately 1%.

With these simulation results we have all components to calculate T_{eff} and α_T. In figure 3.5 we show the theoretical and experimental results for α_T. We neglected the errorbars for the experimental results in the figure.

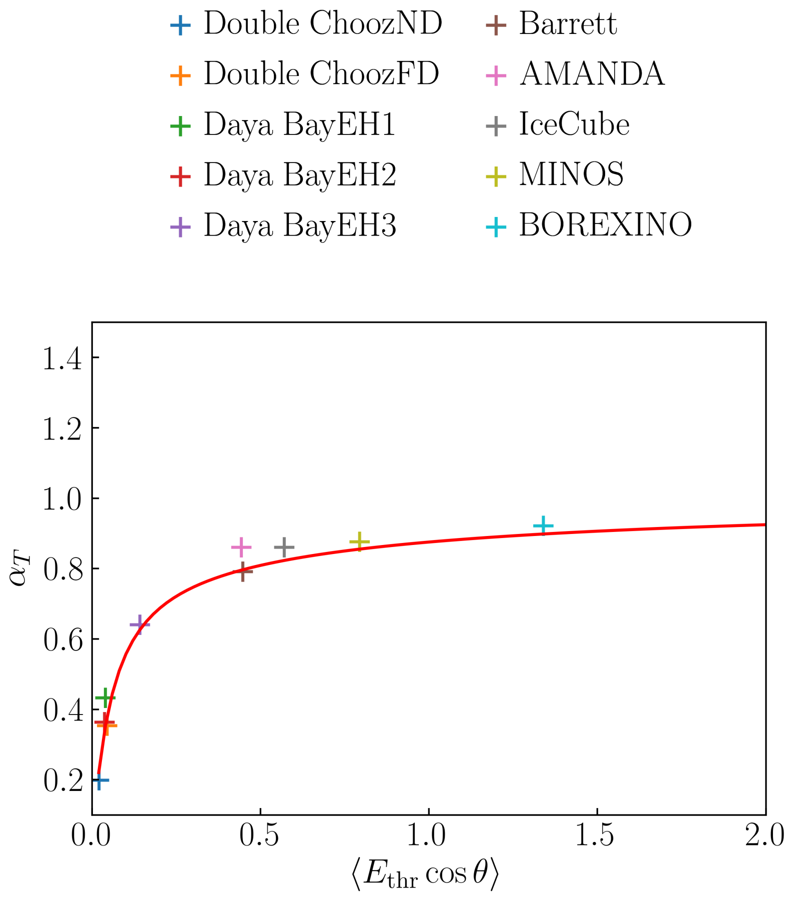

Figure 3.5: The theoretical and experimental results for α_T for $r_{K/\pi} = 0.149$ [65] We include the experimental results from other measurements [60]. The results from the paper discussed here are on the far right. In red we show the theoretical prediction using equation 3.2. Experimental errors are not shown in the plot.

To estimate the kaon to pion ratio, $r_{K/\pi}$ we can now compare the theoretical and experimental values for α_T depending on the plugged in value for the ratio. Since the experimental measurement measures T_{eff}, which has a weak dependence on the ratio, we can compare the prediction and measurement and define the crossing area (within the simulation and experimental errors). Figure 3.6 shows the resulting plot.

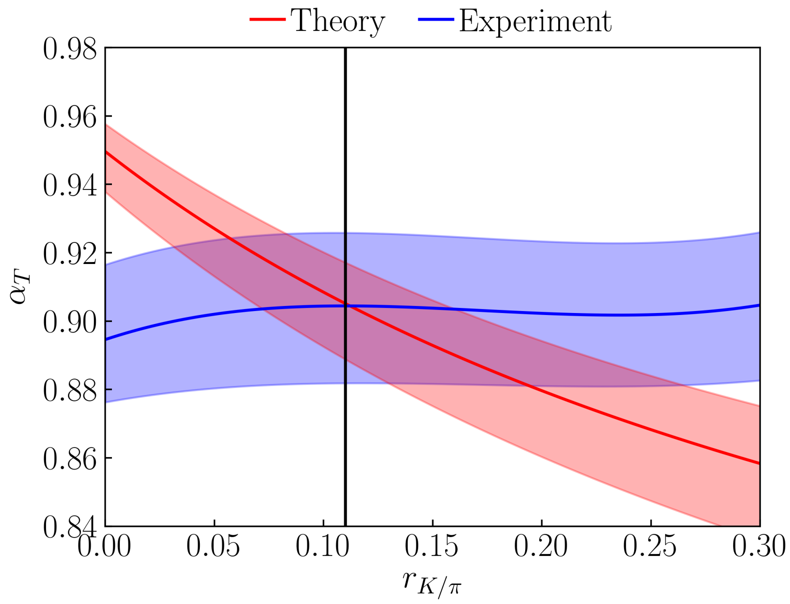

Figure 3.6: Prediction of $r_{K/\pi}$ using BOREXINO data (blue) and the theoretical prediction (red). The shaded regions define the 1σ contours. The crossing region defines the approximate measurement of $r_{K/\pi}$ with a best fit value of $r_{K/\pi} = 0.11$. The black line shows the best fit value.

When including the errors the obtained value the ratio is

$$r_{K/\pi} = 0.11^{+0.11}_{-0.07}. \tag{3.8}$$

This ratio is predicted to hold for a center of mass energy of approximately $\sqrt{s} = (190 \pm 28)$ GeV for collisions of a proton on a nucleon (air) target. For this an average primary collision energy of 18 TeV was used. While the uncertainties are large, due to the comparatively low statistics when compared to IceCube, the minimal threshold energy leads to an expected higher center of mass energy, setting the highest limit for fixed target measurements.

This type of analysis can be done ’out-of-the-box’ with current tools when experimental data is available. In the next section, we will be introducing new models and methods, increasing the range and precision of cosmic ray, neutrino and gamma ray experiments.

3.5 Conclusion

Here we have shown, that by using precise particle cascade modeling techniques, we are capable of answering fundamental particle production questions, such as the K/π ratio. This value is of great importance for the modeling of any high energy strong interaction, required by most particle physics models today.
In the next section we will improve the precision of our cascade models,

by constructing a new electromagnetic model. To this end, we will build a new framework which provides interaction models and the methods required to solve cascade equations. Together with the hadronic models we have used until now, this will allow for a full description of particle cascades in the atmosphere.

EmCa - Electromagnetic Cascades

4

4.1 Coupled Cascade Equations 27
4.2 Theoretical Model 27
Material Effects 32
4.3 Numerical Implementation . 34
Ionization 36
Code 38
4.4 Comparisons 41
CORSIKA 41
EGS4 42
4.5 Three Dimensions 43
Landau approximation . . . 43
Molière Treatment 45
Numerical implementation . 46
4.6 Conclusions 47

Electromagnetic cascades are an ideal testing ground for different modeling schemes of particle showers. The limited number of particles, $e^{\pm}$, γ and if of interest μ have only very few relevant interactions. Due to this a very simple model was developed by Heitler [66, 67]. In this model it is assumed that only Bremsstrahlung, pair production and ionization define the shower's characteristics. A diagram of pair production is given in figure 4.1. Bremsstrahlung is related to pair production by crossing symmetry. In both processes one additional particle is produced, either a photon or an electron, doubling the total number of particles. This means after n interactions, there will be 2^n particles. After each interaction the parent's energy is split equally between the children. Using this simplified view, together with the definition of a splitting length d

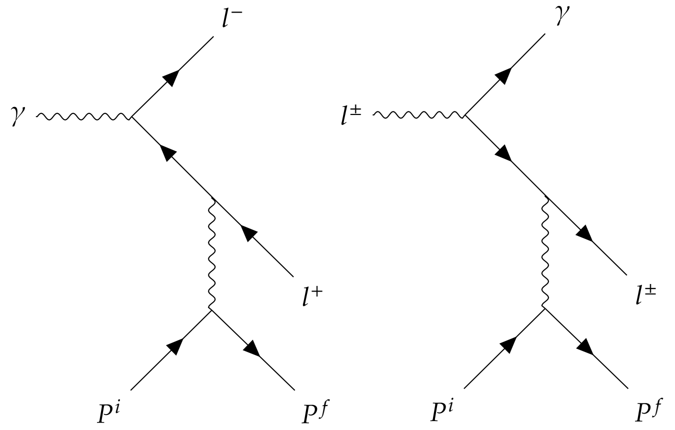

(a) Pair Production **(b)** Bremsstrahlung

Figure 4.1: Diagrams of pair production, $\gamma + Z \rightarrow l^- l^+ +$ anything and Bremsstrahlung. Bremsstrahlung is related to pair production by crossing symmetry. These are the most relevant interactions in electromagnetic cascades at high energies. Note the requirement of an additional nucleus for the processes.

$$d = X_0 \ln 2, \tag{4.1}$$

where X_0 is the radiation length of the material, one can now construct a Heitler model.

After n splitting lengths, a distance x of

$$x = n X_0 \ln 2 \tag{4.2}$$

is traveled by the shower and it has $N = e^{x/X_0}$ particles. The cascade stops, when ionization losses start to dominate. This happens at the critical energy E_{crit} [68], which for air is 86 MeV. With this simplified view, we can now make predictions for the maximum number of particles and the depth at which this number is reached. Since the energy is split equally among the children, the maximum number of particles, N_{max}, is defined by

$$E_0 = E_{\text{crit}} N_{\text{max}}. \tag{4.3}$$

Here E_0 is the primaries energy. From this we can now derive the position of the maximum using $N = 2^n$

$$X_{\text{max}} = X_0 \ln\left(\frac{E_0}{E_{\text{crit}}}\right). \tag{4.4}$$

While very simplified, this model gives a very precise prediction of the position of the shower maximum. On the other hand, this model does not capture the full picture when it comes to the absolute particle count, due to neglecting ionization and other losses. We will now discuss how to model this in a more precise manner.

As mentioned previously, there are different approaches to simulating particle cascades. One is the use of Monte Carlo methods to simulate on an event by event basis, as used in CORSIKA [46] or EGS5 [47]. While Monte Carlo methods have proven successful, they come with a high computational cost. If an average particle flux at high energies (above 1 GeV) is of interest, an iterative approach using cascade equations offers a similar precision to Monte Carlo calculations without the computational expense [21, 48]. This allows for rapid testing and scanning of different models and their parameters. Cascade equation approaches are implemented, for example, in MCEq [51] and CONEX [50]. The python package EmCa*, which we introduce here uses similar numerical methods to those employed in MCEq for the calculation of particle cascades and provides an electromagnetic model, allowing for the simulation of electromagnetic showers. As a framework, it is designed to be easily extendable, allowing a user to include their own interaction models, density models, and materials. Additionally, since the calculations are computationally inexpensive, testing and prototyping can be done at a much faster pace than with Monte Carlo methods. Note that unlike the direct approach used here, it is possible to write an adjoint cascade theory as described in [69].

We will start with a description of the relevant parts of the cascade equations, followed by the used electromagnetic model. We designed the interaction model to be valid for a broad range of elements and many orders of magnitude in energy, starting at 10 MeV up to energies where photo-hadron interactions become relevant. Afterwards, in section (4.3) the numerical implementation and code is discussed. Afterwards we compare results using EmCa to Monte Carlo simulations in section (4.4).

---

* https://github.com/MeighenBergerS/emca

4.1 Coupled Cascade Equations

Using the slant depth, introduced in section 2.2, the transport equations for an electromagnetic particle i are

$$\begin{aligned}\frac{\mathrm{d}\Phi_i(E,X)}{\mathrm{d}X} = &-\frac{\Phi_i(E,X)}{\lambda_i(E)} \\ &-\frac{\partial}{\partial E}\left(\mu(E)\Phi_i(E,X)\right) \\ &+\sum_l \int_E^\infty \mathrm{d}E_l \frac{1}{\sigma(E_l)} \\ &\times \left(\frac{\mathrm{d}\sigma_{l(E_l)\to i(E)}}{\mathrm{d}E}\frac{\Phi_l(E_l,X)}{\lambda_l(E_l)}\right).\end{aligned} \tag{4.5}$$

In the above equation, E is the energy of the particle flux, σ the cross section, λ the interaction length and μ a loss parameter. The first two terms describe losses due to interactions and ionization, respectively. The last one is a source term containing the production of particle i by particle l where the sum runs over all particles.

In the case of EmCa the considered particles are γ, $e^{\pm}$, and $\mu^{\pm}$. Note that for this reason, the decay terms described in section 2.2 can be safely ignored. Muons were added to the cascade to allow the electromagnetic cascade to couple back to hadronic showers.

For the simulation the density of the background medium is required at each step. This requires a depth-dependent model of air. In the following simulations we use the U.S. Standard Atmosphere [25].

4.2 Theoretical Model

The electromagnetic model implemented in EmCa contains four types of interactions, namely pair production, Bremsstrahlung, Compton scattering, and ionization. The differential cross sections used for pair production and Bremsstrahlung were taken from [70]. Other calculations of these interactions are Bethe and Heitler's [71], which is the foundation of the modern understanding of pair production, or Migdal's derivations [72], which includes the LPM effect. More recent calculations allow the treatment of targets of finite thickness done for example by Zakharov [73] and Baier and Katkov [74, 75]. Klein's comparison of pair production in different regimens [76] offers an overview of these calculations.

The advantage of the cross sections by Tsai is that they do not possess an explicit density dependence and therefore allow the numerical treatment described in section (4.3). Density effects, such as Landau-Pomeranchuk-Migdal (LPM) [77, 78] and dielectric [79, 80] effects, are treated separately, as described in the next subsection.

For pair production, $\mathrm{d}\sigma/\mathrm{d}E$ has the form

$$\begin{aligned}\frac{k}{\alpha r_0^2}\frac{\mathrm{d}\sigma}{\mathrm{d}E} = &\left[\frac{4}{3}x^2 - \frac{4}{3}x + 1\right] \\ &\times\left[Z^2(\phi_1 - \frac{4}{3}\log Z - 4f)\right. \\ &\left.\quad + Z(\psi_1 - \frac{8}{3}\log Z)\right] \\ &- \frac{2}{3}x\left[Z^2(\phi_1 - \phi_2) + Z(\psi_1 - \psi_2)\right]\end{aligned} \tag{4.6}$$

and for Bremsstrahlung

$$\begin{aligned}\frac{k}{\alpha r_0^2}\frac{\mathrm{d}\sigma}{\mathrm{d}k} = &\left[y^2 - \frac{4}{3}y + \frac{4}{3}\right] \\ &\times\left[Z^2(\phi_1 - \frac{4}{3}\log Z - 4f)\right. \\ &\left.\quad + Z(\psi_1 - \frac{8}{3}\log Z)\right] \\ &- \frac{2}{3}(1-y) \\ &\times\left[Z^2(\phi_1 - \phi_2) + Z(\psi_1 - \psi_2)\right].\end{aligned} \tag{4.7}$$

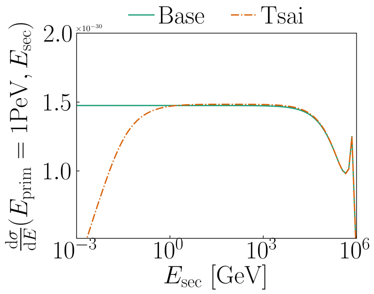

Figure 4.2: The difference the inclusion of screening makes on the differential cross section for pair production. In green the full screening approximation was used, while in orange the full cross section.

In equations 4.6 and 4.7, ϕ_i and ψ_i describe screening effects, Z is the atomic number of the background medium, α the fine structure constant and r_0 the classical electron radius. f is a Coulomb correction which is defined as

$$f(z = (\alpha Z)^2) = z\sum_{n=1}^{\infty}\frac{1}{n(n^2+1)}. \tag{4.8}$$

For convenience we introduce $x = E/k$ and $y = k/E$, with E being the electron energy and k the photon energy. To calculate the screening functions, we use a Thomas-Fermi-Molier model (TFM), as given in [70]. These screening functions describe the shielding of the nucleus's charge due to the surrounding electrons. For higher energies ($E > 10$ GeV) these functions become constant, which is called the "full screening" scenario. The difference between the full screening scenario and the total cross section is shown in figure 4.2. There we clearly see that for the production of low energy electrons the differential cross sections differ.

In this case it is safe to set $\phi_i = \phi_i(0)$ and $\psi_j = \psi_j(0)$. In the TFM the individual screening factors are defined as

$$\phi_1 = 2(1 + \log(a^2 Z^{2/3} m_e^2)) - 2\log(1 + b^2) - 4b\arctan(b^{-1})$$

$$\phi_2 = 2(2/3 + \log(a^2 Z^{2/3} m_e^2)) - 2\log(1 + b^2) + 8b^2(1 - b\arctan(b^{-1}) - 0.75\log(1 + b^{-2}))$$

$$\psi_1 = 2(1 + \log(a'^2 Z^{4/3} m_e^2) - 2\log(1 + b'^2) - 4b'\arctan(b^{-1})$$

$$\psi_2 = 2(2/3 + \log(a'^2 Z^{4/3} m_e^2)) - 2\log(1 + b'^2) + 8b'^2(1 - b\arctan(b'^{-1}) - 0.75\log(1 + b'^{-2})).$$

The occurring parameters are defined as follows

$$
\begin{aligned}
a &= 111.7Z^{-1/3}/m_e \\
a' &= 724.2Z^{-2/3}/m_e \\
b &= 0.55846\gamma \\
b' &= 3.6201\epsilon \\
\gamma &= \tfrac{200\delta}{m_e Z^{1/3}} \\
\epsilon &= \tfrac{200\delta}{m_e Z^{2/3}} \\
\delta &= |\tfrac{m_e^2 k}{2E(k-E)}|
\end{aligned}
$$

It is useful to define the unit radiation length X_0. This is a material constant defining when an electron's energy has fallen to $1/e$ its original energy when passing through a material. It is defined as

$$X_0^{-1} = \alpha r_0^2 N_A A^{-1}\left[Z^2\left(\phi_1(0) - \frac{4}{3}\ln Z - 4f\right) + Z\left(\psi_1(0) - \frac{8}{3}\ln Z\right)\right]. \tag{4.9}$$

Here N_A is Avogadro's constant and A the atomic mass number of the material. This is a recurring value when dealing with electromagnetic cascades, for it can be measured directly experimentally. Additionally, one can use the radiation length to simplify the cross sections in the full-screening approximation

$$\frac{\mathrm{d}\sigma_{\text{pair}}}{\mathrm{d}E} \approx \frac{A}{N_A X_0 k}\left(1 - \frac{4}{3}x(1-x)\right) \tag{4.10}$$

and

$$\frac{\mathrm{d}\sigma_{\text{brems}}}{\mathrm{d}k} = \frac{A}{N_A X_0 k}\left(y^2 - \frac{4}{3}y + \frac{4}{3}\right). \tag{4.11}$$

Note that the cross section for Bremsstrahlung can not be integrated due to the divergence for $k \longrightarrow 0$. Typically this is treated with a low energy cut-off but we will show later, that by introducing material effects this infrared divergence can be removed.

The differential cross section for pair production can be integrated and has the form

$$\sigma_{\text{pair}} = \frac{7}{9}\frac{A}{X_0 N_A}. \tag{4.12}$$

This means in the high energy limit, we expect the cross section to become constant. Using

$$\lambda = \frac{A}{N_A}\frac{1}{\sigma}, \tag{4.13}$$

we can derive the interaction length of photons due to pair production

$$\lambda_{\text{pair}} = \frac{9}{7}X_0. \tag{4.14}$$

Figure 4.3 shows a plot of the differential cross sections for the different processes for a primary energy of 1 PeV.

The corresponding integrated cross sections are shown in figure 4.5, where the channel $e \longrightarrow e$ was dropped since the integrated cross section is the same as $e \longrightarrow \gamma$. We show the resulting interaction lengths for photons and electrons in figure 4.4. We include the radiation length as shown in PDG [52], which we scaled according to equation 4.14 to make the comparison. We see that the interaction lengths agree well for high energies, with the differences at lower energies to be expected, since the definition of the radiation length is not applicable in those regimes. Muon pair production due its natural low energy cutoff can be treated in a simpler fashion, since screening is irrelevant. For this reason, a different cross section, described in [81], is implemented. The form of the differential cross section is

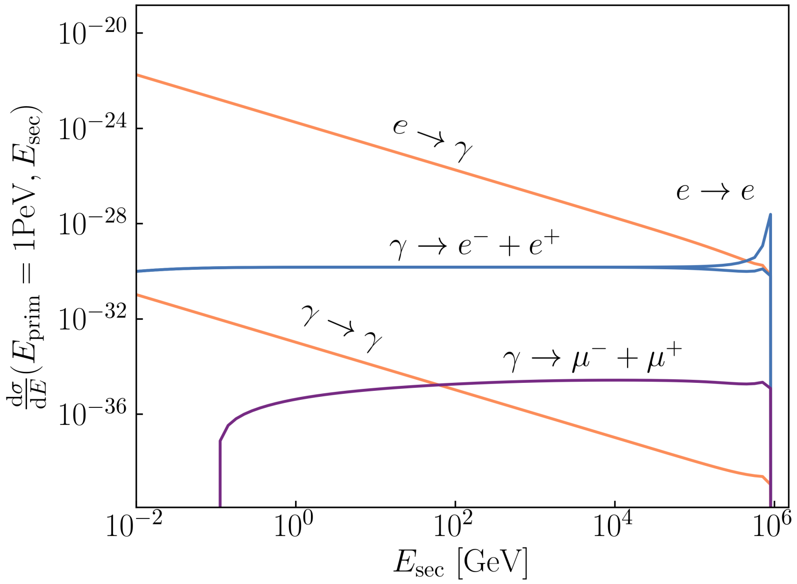

Figure 4.3: The differential cross sections for some of the interactions implemented in EmCa. The processes are Bremsstrahlung, pair production and Compton scattering. Note that the Bremsstrahlung cross section is split into to parts. The self regeneration and the production of photons.

$$\frac{d\sigma_\mu}{dE} = \frac{4\alpha r_e^2 Z^2}{k}\left(1 - \frac{4}{3}(x - x^2)\right)\log(W). \tag{4.15}$$

Where x = E_μ/k and the weight factor W is defined as

$$W = \frac{BZ^{-1/3}}{D}\frac{m_\mu}{m_e}\frac{1 + (D\sqrt{e} - 2)\frac{\delta}{m_\mu}}{1 + BZ^{-1/3}\sqrt{e}\frac{\delta}{m_e}}. \tag{4.16}$$

In turn the parameters are $B = 202.4$ and $D = 1.49$ for hydrogen and $B = 183$ and $D = 1.54A^{0.27}$ otherwise. Finally $\delta = \frac{m_\mu^2}{2k(x-x^2)}$ and $\sqrt{e} = 1.6487$. Note that as expected, the shapes of the differential cross sections for muon and electron pair production are similar. An added benefit of this definition of the cross section is that it is implemented in CORSIKA as well, allowing for a direct comparison.

For the pair production of electrons by muons, we use the simple formulas from [82]

$$\nu\frac{\mathrm{d}\sigma}{\mathrm{d}\nu} = \frac{7}{9}\frac{\alpha}{\pi}4Z^2\alpha r_0^2 \ln\left(\frac{184.15}{Z^{1/3}}\frac{m_\mu}{m_e}\right)\left[(1 + z^2)\ln\left(1 + \frac{1}{z^2}\right) - 1\right]. \tag{4.17}$$

Here ν is the energy of the produced electrons and z is defined as

$$z = \frac{\nu}{E}\frac{m_\mu}{4m_e}, \tag{4.18}$$

with E being the muon's energy. For the Bremsstrahlung differential cross section of muons we follow [83]

$$\begin{aligned}\frac{\mathrm{d}\sigma}{\mathrm{d}y} =& \alpha\left(2Z\frac{m_e}{m_\mu}r_0\right)^2\left(\frac{4}{3}-\frac{4}{3}y+y^2\right)\frac{\Phi(\delta)}{y} \\ &+\alpha Z\left(2\frac{m_e}{m_\mu}r_0\right)^2\left(\frac{4}{3}-\frac{4}{3}y+y^2\right)\frac{\Phi_{\mathrm{in}}(\delta)}{y}.\end{aligned} \tag{4.19}$$

Here the first term describes the contribution due to the nucleus off of which the muon is scattering and the second term the contribution form electrons. Note the similarities between this equation and the one for electrons. The Φ are defined as

$$\Phi(\delta) = \ln\left(\frac{Bm_\mu Z^{-1/3}/m_e}{1+\delta\sqrt{e}BZ^{-1/3}/m_e}\right) - \Delta_n(\delta) \tag{4.20}$$

and

$$\Phi_{\mathrm{in}}(\delta) = \ln\left(\frac{m_\mu/\delta}{m_\mu\delta/m_e^2+\sqrt{e}}\right) - \ln\left(1+\frac{m_e}{\delta BZ^{-2/3}\sqrt{e}}\right). \tag{4.21}$$

Finally Δ_n is defined as

$$\Delta_n = \ln\left(\frac{D_n}{1+\delta(D_n\sqrt{e}-2)/m_\mu}\right). \tag{4.22}$$

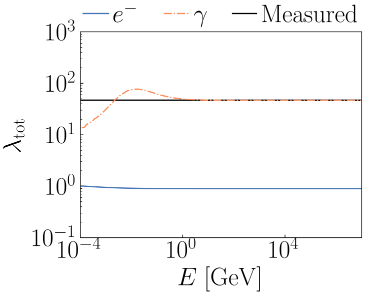

Figure 4.4: The interaction lengths for electrons and photons. We include the measured interaction length for photons by scaling the measured radiation length from PDG [52].

Compton scattering needs to be added for secondary spectra with a low energy cutoff below 100 MeV, when this channel becomes relevant compared to pair production. Figure 4.5 shows the total cross sections for the implemented processes. At low energies the total cross section for Compton scattering dominates over those from pair production. For Compton scattering the Klein-Nishina cross section [84] is used, which is a generalized version of Compton- and Thomson-scattering. It has the form

$$\frac{\mathrm{d}\sigma}{\mathrm{d}k} = \frac{\pi r_0^2}{m_e}\frac{Z}{\kappa^2}\left(\epsilon+\frac{1}{\epsilon}-\frac{2}{\kappa}\frac{1-\epsilon}{\epsilon}+\frac{1}{\kappa^2}\left[\frac{1-\epsilon}{\epsilon}\right]^2\right), \tag{4.23}$$

with $\epsilon = k/k_0$, $\kappa = k_0/m_e$, where $k_0 = E_{\mathrm{prim}}/m_e$ and $k = k_{\mathrm{sec}}/m_e$. Due to the nature of two body scattering processes when integrating over equation 4.23 a minimal energy needs to be introduced $k_{\mathrm{min}} = k_0/(2\kappa+1)$.

For the description of ionization losses we use the energy loss tables generated by ESTAR [85], which describe μ in equation 4.5. The collision stopping powers in those tables are calculated using [86, 87]. Note that ionization losses dominate the tail of a particle shower's development. When comparing interaction models, such as the one found in EmCa or EGS5, a typical difference in a shower's development is the tail. This is usually due to differing definitions in the ionization losses. For comparisons with other models, we have implemented their respective definitions of the ionization losses.

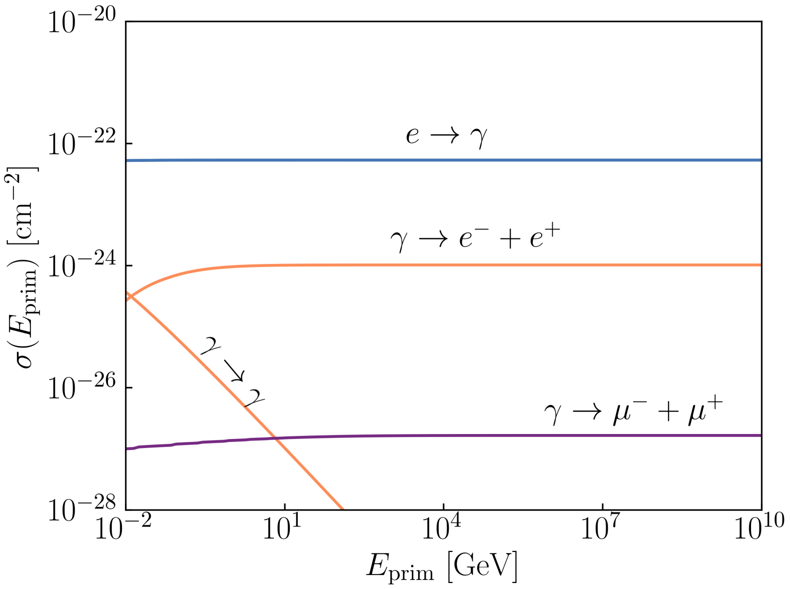

Figure 4.5: The integrated cross section for the different production channels. Other interactions only play a subleading role in the energy ranges of interest and can be ignored.

Material Effects

To allow for a higher range of validity in energy we account for additional material effects, i.e. dielectric suppression [79, 80] and the LPM effect [72, 78].

The dielectric effect is treated as a suppression factor, $S_{\mathrm{die}}(k)$, of the differential cross section of the form

$$S_{\mathrm{die}}(k) = \frac{k^2}{k^2 + (\gamma \cdot \hbar\omega_p)^2}, \tag{4.24}$$

where ω_p is the plasma frequency of the material. Due to the density dependence of $\omega_p \propto \sqrt{\rho}$ the differential cross sections become density dependent. The point at which the dielectric effect becomes relevant can be estimated by calculating the ratio $r = \omega_p / m_e$. For air at standard density $\omega_p(\mathrm{Air}) = 6.6 \times 10^{-10}$ GeV and $r \approx 10^{-6}$, which leads to the differential cross section starting to be suppressed at about $E_{\mathrm{sec}} = E_{\mathrm{prim}} \times 10^{-6}$. In atmospheric showers this does reduce the production of low energy photons at the start of the shower. Later in the shower development, where far more low energy photons are produced, the difference becomes negligible.

In most cases the dielectric effect can safely be ignored in air. There is one major advantage of including this effect. Due to the inclusion of the dielectric effect the cross section for Bremsstrahlung no longer diverges for $k \longrightarrow 0$, allowing for precise calculations of the total cross section. Thus, even for air showers, where there is no direct physical effect, the dielectric effect allows for the calculation of the total cross section, without the introduction of a nonphysical low energy cutoff.

On the other hand for materials with a larger Z, metals for example, typical values of $r \approx 10^{-4}$ result in a larger relevance of the dielectric effect.

The LPM effect suppresses the interaction cross sections at high energies. This can be accounted for by adding a suppression term [78] of the form

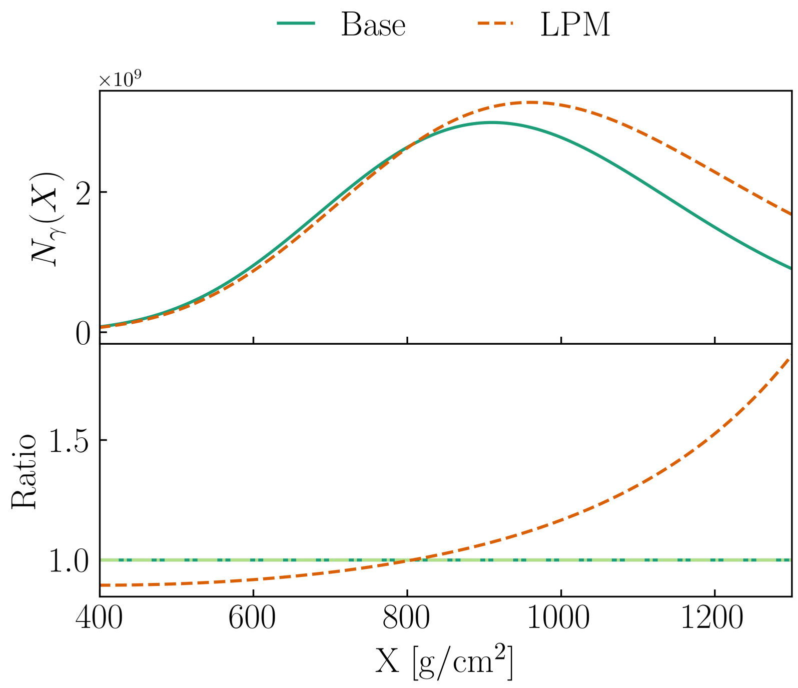

Figure 4.6: The particle number changes to an atmospheric shower due to the LPM effect. Plotted is the total number of particles in a 10 EeV γ primary initiated shower in air. The low energy cutoff was chosen to be 86 MeV. The LPM effect causes a retardation of the shower development.

$$S_{\mathrm{LPM}} = \sqrt{\frac{kE_{\mathrm{LPM}}}{E(E-k)}}, \tag{4.25}$$

with

$$E_{\mathrm{LPM}} = \frac{7.7\ \mathrm{TeV} X_0}{\rho}, \tag{4.26}$$

to the differential cross section. This again would introduce a density dependence to the cross section. Due to the employed numerical methods, discussed in section (4.3), we wish to avoid this and instead treat the LPM effect by re-scaling the interaction lengths λ_{Pre}, defined in equation 4.13, according to

$$\lambda_{\mathrm{True}} = \left(\frac{E_{\mathrm{prim}}}{E_{\mathrm{LPM}}}\right)^{1/2} \lambda_{\mathrm{Pre}}, \text{ for } E_{\mathrm{LPM}} < E_{\mathrm{prim}}. \tag{4.27}$$

This allows the shape of the differential cross section to remain density independent, and the interaction length only needs to be re-scaled according to the current density. In figure 4.6, we show the consequences of including the LPM effect (orange) for air showers when compared to the baseline theory (green) without it.

These material effects change the amount of energy carried by electrons, which is relevant to fluorescence experiments such as Auger [88] and TA [89]. Fluorescence is generated by collision losses of charged particles in the atmosphere. By including these effects, the energy in the electron part of the shower is reduced, reducing fluorescence. Not including these effects would lead to an overestimation of the deposited energy of atmospheric cascades. We will discuss this in the next chapter.

4.3 Numerical Implementation

Similar to MCEq, the cascade equations are discretized on a logarithmic energy grid in EmCa. The particle fluxes are arranged in a state vector $\vec{\Phi}$ of the form

$$\vec{\Phi} = \left(\vec{\Phi}^{e^-}, \vec{\Phi}^{e^+}, \vec{\Phi}^{\gamma}, \vec{\Phi}^{\mu^-}, \vec{\Phi}^{\mu^+}\right)^T \tag{4.28}$$

with sub-vectors of the form

$$\vec{\Phi}^{i} = \left(\Phi^{i}_{E_0}, \Phi^{i}_{E_1}, ..., \Phi^{i}_{E_N}\right)^T . \tag{4.29}$$

The differential, $\frac{\mathrm{d}\sigma_{li}}{\mathrm{d}E}$ and total cross sections, σ_l, are arranged in a matrix $\mathbf{C}_{li}$ with elements

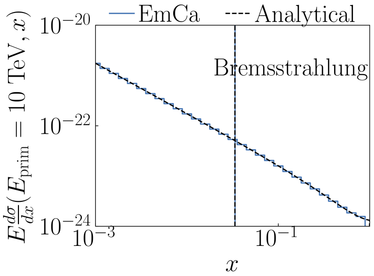

Figure 4.7: Binned (EmCa) version of the differential cross section for $e \longrightarrow \gamma$ and its analytical form. The functions are plotted against the fractional energy $x = E_{\mathrm{sec}}/E_{\mathrm{prim}}$ of the secondary particle. The dashed vertical lines are the position of the average of the binned and analytic versions. The high agreement is achieved by including first and second moments in the calculations.

$$c_{l(E_l)i(E_i)} = \Delta E_l \frac{1}{\sigma(E_l)} \langle \frac{\mathrm{d}\sigma_{l(E_l)\to i(E_i)}}{\mathrm{d}E_i} \rangle \tag{4.30}$$

and shape

$$\mathbf{C}_{li} = \begin{pmatrix} c_{l(E_0)i(E_0)} & \cdots & c_{l(E_1)i(E_0)} \\ 0 & \cdots & c_{l(E_1)i(E_N)} \\ \cdots & \cdots & \cdots \\ 0 & \cdots & c_{l(E_N)i(E_N)} \end{pmatrix}. \tag{4.31}$$

Note that due to energy conservation $\mathbf{C_{li}}$ is an upper triangular matrix. In the above calculations bin averaged differential cross sections are defined in equations (4.32, 4.33).

Due to the nature of electromagnetic cascades evolving very quickly and having only a limited amount of possible interactions, numerical errors as small as 0.1% affect the shower development. As a cross-check, the calculation of σ and $\frac{\mathrm{d}\sigma}{\mathrm{d}E}$, from equation 4.5, are kept separate. Integrations of the differential cross sections are performed in fractional energy space by substituting the secondary's energy E_{sec}, with $x = \frac{E_{\mathrm{sec}}}{E_{\mathrm{prim}}}$. Figure 4.9 shows the differential cross section for $e \longrightarrow e$ in fractional energy space. Integrations are then performed on $\frac{1}{E_{\mathrm{prim}}} \frac{\mathrm{d}\sigma}{\mathrm{d}x}(x, E_{\mathrm{prim}})$. In this scheme $\sigma(E)$ is calculated by integrating from 0 to 1.

We average $\frac{\mathrm{d}\sigma}{\mathrm{d}E}$ and its first and second moments for each energy bin. This means for each energy bin three integrals are performed,

$$\begin{aligned} \mu^0_{l,i} &= \langle \frac{\mathrm{d}\sigma}{\mathrm{d}E_i}(E_l, E_i) \rangle_{l,i} = \int \frac{\mathrm{d}\sigma}{\mathrm{d}E_i}(E_l, E_i)\mathrm{d}E_i \\ \mu^1_{l,i} &= \langle \frac{\mathrm{d}\sigma}{\mathrm{d}E_i}(E_l, E_i) \rangle^{\mathrm{Mom}\ 1}_{l,i} = \int E_i \frac{\mathrm{d}\sigma}{\mathrm{d}E_i}(E_l, E_i)\mathrm{d}E_i \\ \mu^2_{l,i} &= \langle \frac{\mathrm{d}\sigma}{\mathrm{d}E_i}(E_l, E_i) \rangle^{\mathrm{Mom}\ 2}_{l,i} = \int E_i^2 \frac{\mathrm{d}\sigma}{\mathrm{d}E_i}(E_l, E_i)\mathrm{d}E_i . \end{aligned} \tag{4.32}$$

The integrals are calculated over the bin widths using a Tanh-Sinh quadrature, and defining the maximum of the function as an integration node. Then for each bin, defined by the center E_i and the width ΔE_i, the equation

$$\begin{bmatrix} \Delta E_{i-1} & \Delta E_i & \Delta E_{i+1} \\ E_{i-1}\Delta E_{i-1} & E_i \Delta E_i & E_{i+1}\Delta E_{i+1} \\ E_{i-1}^2 \Delta E_{i-1} & E_i^2 \Delta E_i & E_{i+1}^2 \Delta E_{i+1} \end{bmatrix} \times \begin{bmatrix} x_1 \\ x_2 \\ x_3 \end{bmatrix} = \begin{bmatrix} \mu_{l,i}^0 \\ \mu_{l,i}^1 \\ \mu_{l,i}^2 \end{bmatrix}, \tag{4.33}$$

is solved. This methodology has the advantage of conserving energy and particle number, as discussed in subsection 2.2.

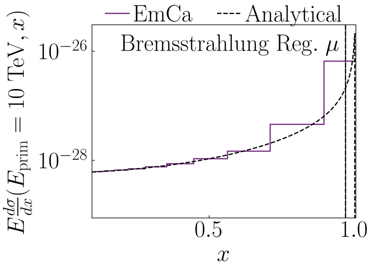

Figure 4.8: Binned (EmCa) version of the differential cross section for $\mu \rightarrow \mu$ and its analytical form. The functions are plotted against the fractional energy $x = E_{\text{sec}}/E_{\text{prim}}$ of the secondary particle. The dashed vertical lines are the position of the average of the binned and analytic versions. The high agreement is achieved by including first and second moments in the calculations.

In figures 4.9, 4.7 and 4.8 we compare the binned differential cross sections EmCa uses to the analytic ones, for the most unstable process, Bremsstrahlung . The vertical lines show the position of the average of each version, which shows a very high agreement. The functions are plotted against the fractional energy carried by the secondary particle $x = E_{\text{sec}}/E_{\text{prim}}$. The interaction matrices from equation 4.31 are then grouped together in a single matrix **C** of the form

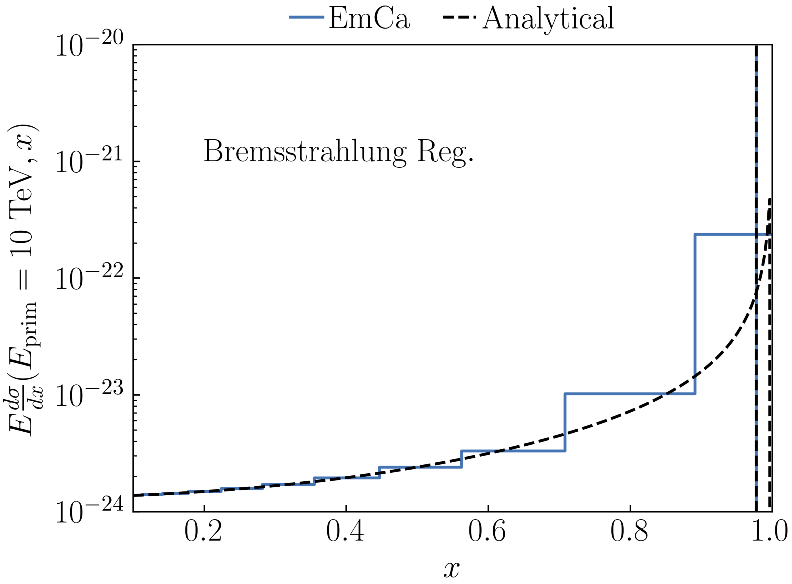

Figure 4.9: Binned (EmCa) version of the differential cross section for $e \rightarrow e$ and its analytical form. The functions are plotted against the fractional energy $x = E_{\text{sec}}/E_{\text{prim}}$ of the secondary particle. The dashed vertical lines are the position of the average of the binned and analytic versions. The high agreement is achieved by including first and second moments in the calculations.

$$\mathbf{C} = \begin{pmatrix} \mathbf{C}_{e^-e^-} & \dots & \mathbf{C}_{\mu^+e^-} \\ \mathbf{C}_{e^-e^+} & \dots & \mathbf{C}_{\mu^+e^+} \\ \dots & \dots & \dots \\ \mathbf{C}_{e^-\mu^+} & \dots & \mathbf{C}_{\mu^+\mu^+} \end{pmatrix}. \tag{4.34}$$

The interaction lengths are organized into a diagonal matrix $\mathbf{\Lambda}_{\text{int}}$ of the form

$$\begin{aligned} \mathbf{\Lambda}_{\text{int}} = \text{diag}(&\frac{1}{\lambda_{int}^{e^-}(E_0)}, \cdots, \frac{1}{\lambda_{int}^{e^-}(E_N)}, \\ &\frac{1}{\lambda_{int}^{e^+}(E_0)}, \cdots, \frac{1}{\lambda_{int}^{e^+}(E_N)}, \\ &\cdots). \end{aligned} \tag{4.35}$$

Finally, the ionization loss term is treated by discretizing the loss parameter μ in energy and approximating the differential using a seven-point stencil method. These steps are discussed more in-depth in the next subsection. The resulting operator is written as **L**. Approximating equation 4.5 using the above definitions results in

$$\frac{\mathrm{d}\vec{\Phi}}{\mathrm{d}X} = (-\mathbf{L} + (-1 + \mathbf{C})\mathbf{\Lambda}_{\mathrm{int}})\,\vec{\Phi}. \tag{4.36}$$

Combining the terms, besides $\vec{\Phi}$, results in a single derivative operator. Figure 4.10 shows the non-zero elements of this resulting operator. Note the upper triangular shape of all block-matrices due to energy conservation. Zero elements in the upper triangle are typically caused by kinematic constraints. To solve equation 4.36 we use an explicit Euler solver. An integration step has the form

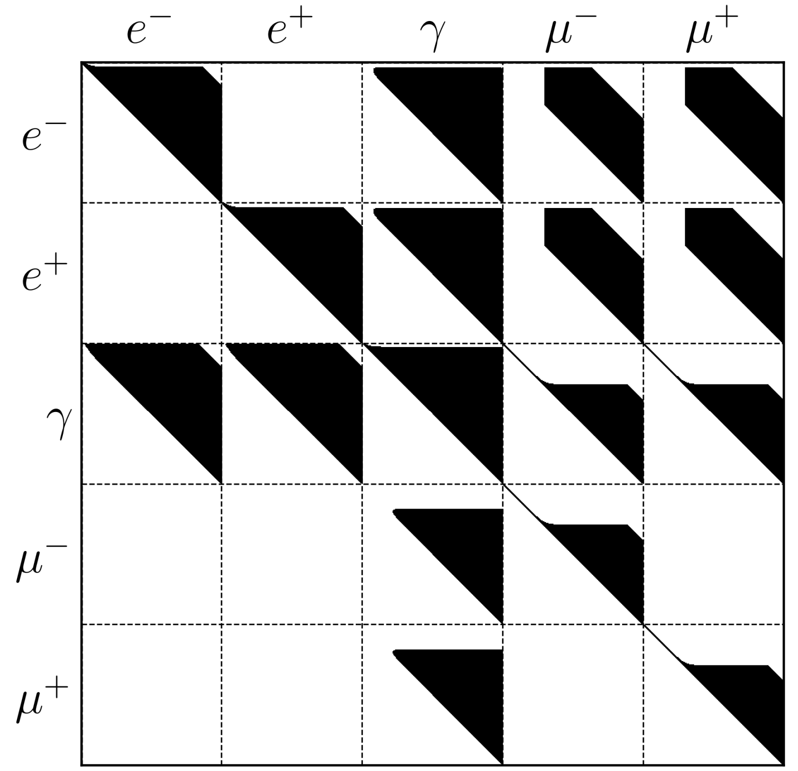

Figure 4.10: The non-zero values of the equation matrix. Each non-zero block corresponds to a specific interaction, e.g. the first block (e^-, e^-) describes the electron self-interaction. The upper triangular shapes are cause by energy conservation. The x axis corresponds to increasing primary energies, while the y axis to increasing secondary energies. The zero elements in the upper triangles are usually caused by kinematics constraints of the underlying interaction process.

$$\begin{aligned}\vec{\Phi}(X + \Delta X) =& (-\mathbf{L} + (-1 + \mathbf{C})\Lambda_{int}) \\ & \times \vec{\Phi}(X)\Delta X.\end{aligned} \tag{4.37}$$

Ionization

Ionization losses are treated as a continuous loss term in the cascade equation. This turns the ordinary differential equation into a partial one. Implying the need for an implicit solver method. To avoid this, the continuous loss terms are discretized using a seven-point stencil method.

In this approximation, a derivative of a function $f(x)$ is written as

$$\begin{aligned} \frac{\partial f}{\partial x} \approx \frac{1}{60h}\big(& -1f(x-3h) + 9f(x-2h) \\ & -45f(x-h) + 0f(x+0h) \\ & +45f(x+h) - 9f(x+2h) \\ & +1f(x+3h)\big), \end{aligned} \tag{4.38}$$

where h is the used step size. The differential operator, $\mathbf{L}$ is then calculated by multiplying the approximation for ∂_E on the left with $\frac{1}{E}$ and from the right with $\mu(E)$. Applying this definition to the ionization losses, the discretized form can be written as

$$\partial_E \mu(E)\Phi = \mathbf{L}\Phi. \tag{4.39}$$

The $1/E$ term appears due to the use of a logarithmic energy grid, and $\mathbf{L}$ is calculated using the above mentioned stencil method. A comparison between the ESTAR tables (red), the binned version in EmCa (blue) and an energy loss simulation using EmCa (green) is shown in figure 4.11. The resulting energy losses from the simulation show a high agreement, $\approx 3\%$, with the ESTAR table results. In EmCa the recommended low energy cutoff is defined by E_{crit} using Rossi's definition [68]. E_{crit} is the point at which collision losses start to dominate the electron energy losses over radiative ones. The critical energy is defined as

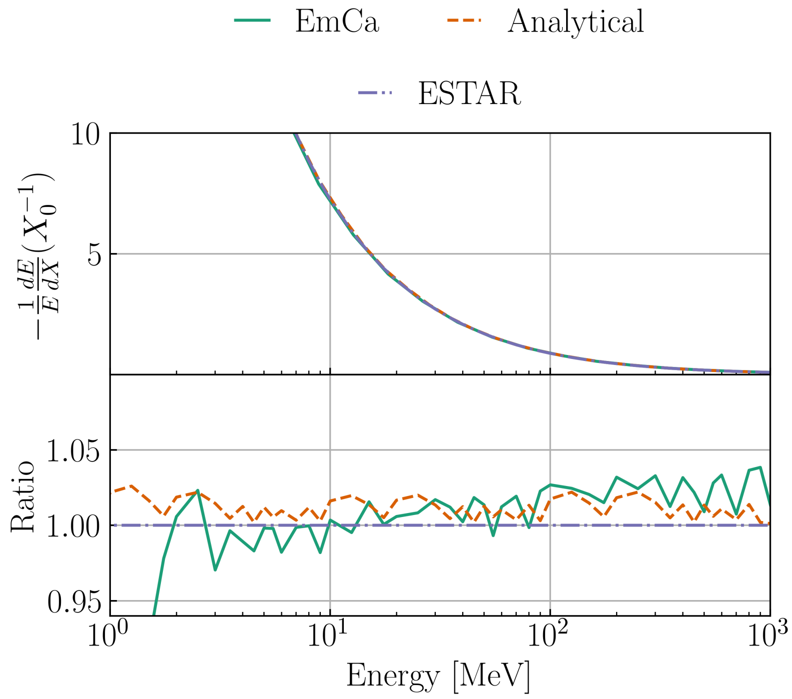

Figure 4.11: The ionization loss function implemented in EmCa. The tables from ESTAR (purple), the binned version in EmCa (orange) and energy loss simulation results (green) are compared. To simulate the average energy losses, electrons with different energies are injected into the material and propagated through it, while all radiative losses are switched off. Using the average energy loss per integration step we normalize it to X_0. The 'spikes' in the ratio plot are due to the discretization employed in EmCa.

$$E_{\text{crit}}^{gas} = \frac{710\text{ MeV}}{Z + 0.92}, \tag{4.40}$$

and

$$E_{\text{crit}}^{solid} = \frac{610\text{ MeV}}{Z + 1.24}. \tag{4.41}$$

For air the critical energy is 86 MeV.

Code

All of these functions are grouped together in the Python package EmCa. The general overview of the structure of the code is given in figure 4.12. We will give an overview of the code itself, by following the steps when it is run.

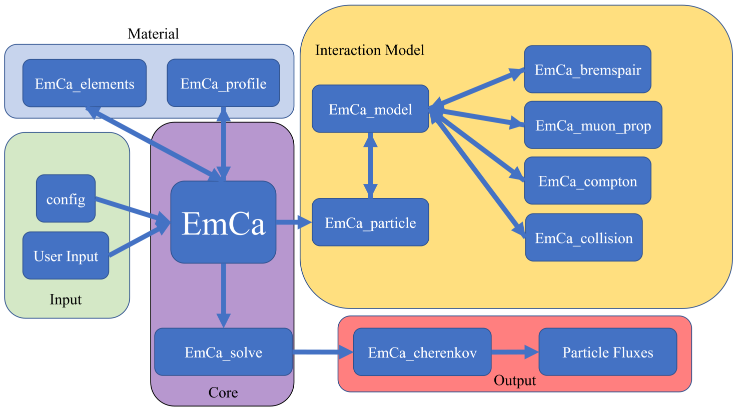

Figure 4.12: The structure of the EmCa package. The modules are kept independent of each other, allowing for easier modification.

Input

First the inputs by the user are collected, either as direct inputs or in the configuration file *config.py*. There are multiple options, such as the interaction model, currently 3 are implemented

- *Tsai_Full*: The fully implemented version of the cross sections discussed here. This is the standard interaction model used.
- *Tsai_Max*: The same model as the one above in the full screening approximation. This is a useful model to run cross checks and high energy simulations.
- *BH*: A Bethe-Heitler interaction model [71] based on the one implemented in EGS4 and in turn in CORSIKA. This allows for a direct comparison of the interaction models in a single framework.

It is also possible to turn individual interactions off at this step, as well as ionization losses. For the simulation run itself a primary flux, or individual particle with an injection angle need to be defined. Should a different material as Earth's atmosphere be used, this needs to be defined at this step as well. An example of the code for this step, when one wishes to use the *Tsai_Max* model with an electron primary and 1 PeV of energy is the following

```python
from emca import EmCa, config

config['run']['initial flux'] = None
config['run']['primary type'] = 11
config['run']['primary energy'] = 1e6
config['general']['interaction model'] = 'Tsai_Max'
```

Core

Once the user inputs are defined the class *EmCaRun* from *EmCa.py* can be initialized. This is the core class of the simulation package and offers the main interface. From here all of the parameters, user inputs are passed to the other modules, and their results are in turn collected. For a general user, this is the only module they will need to interact with. Once this class has been initialized, the simulation is ready to start, with the actual equation solving being handled in *EmCa_solve*. The code steps for this are short

```
emca_run = EmCa.EmCaRun()
emca_run.solve()
```

Material

The file *EmCa_elements.py* collects the necessary material properties for a simulation run. Should a user wish to model a material, which is not included in the package, it would need to be added here. In *EmCa_profile* the density of the material is defined. Currently there are two options, the atmospheric model based on the US Standard Atmosphere or a homogeneous medium.

Interaction Model

EmCa_particle is the core module for the simulation of the particle flux. This module creates the interaction model and particles based on the user input. Every particle is defined by its interaction length and interaction matrices. These need to be constructed by integrating over the analytical forms of the differential cross sections. These in turn are collected in a class *EmCa_model*, which handles the necessary normalizations and transformations. The files *EmCa_bremspair*, *EmCa_muon_prop* and *EmCa_compton* store the corresponding analytical differential cross section. Should a user want to implement a new interaction cross section, it would need to be added as a function to the corresponding file. *EmCa_collision* deals with the construction of the ionization loss matrix.

The construction of these interaction and loss matrices are by far the most computationally expensive steps in the simulation chain. For this reason the matrices are stored as pickle files after construction. Reusing the interaction matrices drastically cuts down on calculation time. Unless the material or energy grids are changed, recalculating the interaction matrices should not be necessary and the model construction step can be skipped.

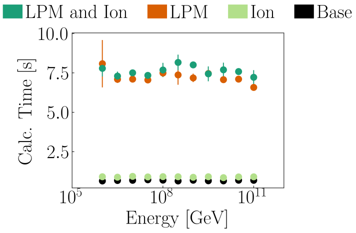

Figure 4.13: Here we show the required simulation times for electromagnetic showers in the atmosphere initiated by electron primaries with different energies. We also show how modeling ionization and the LPM effect change the required simulation times. The computationally most expensive step is the modeling of the LPM effect. This requires a new interaction length at every simulation step due to the scaling factor.

Output

After the equation matrices are constructed and the cascade equation is solved, the simulation is finished and the user can access the particle fluxes at arbitrary points along the shower path. Should the option be set, an additional simulation step is performed in *EmCa_cherenkov*, namely the calculation of light yields due to Cherenkov radiation. The calculation itself is done by applying the Frank-Tamm formula [90].

The EmCa package comes with a few examples, with which all of the plots pertaining to electromagnetic cascades in this thesis were created. Here we show a full example simulation code using EmCa

```
# Importing the module and config file
from emca import EmCa, config

# Setting some user parameters
config[’run’][’initial flux’] = None
config[’run’][’primary type’] = 11
config[’run’][’primary energy’] = 1e6
config[’general’][’interaction model’] = ’Tsai_Max’

# Initializing the class
emca_run = EmCa.EmCaRun()

# Running the simulation
emca_run.solve()

# Total number of particles at each step in X
particle_number = {}
for particle in config["part and int"][’particles’]:
    particle_number[particle] = np.sum(emca_run.results[particle]
     * emca_run.e_bin, axis=1)
```

In figure 4.14 we plot the output from this piece of code. Note that we performed an integration to obtain the total particle counts. The outputs from EmCa are the differential particle fluxes, independent of the type of injection.

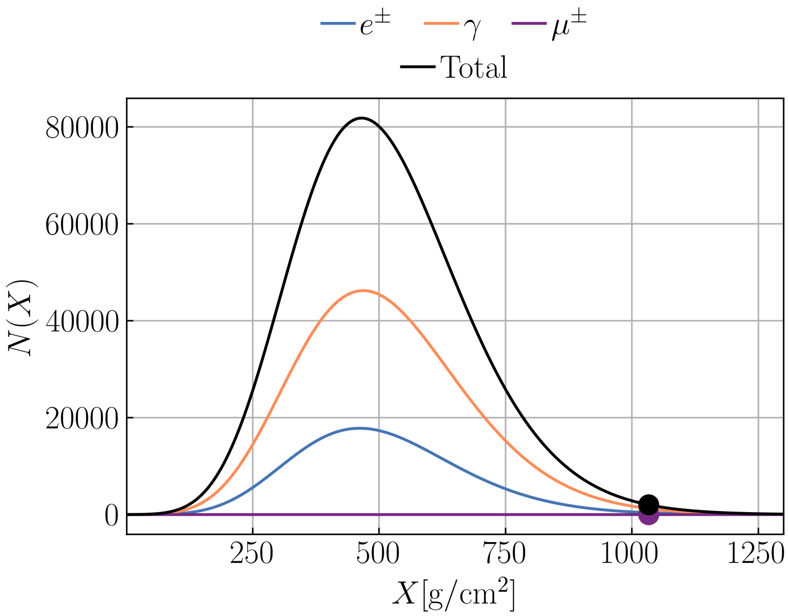

Figure 4.14: An example simulation run of an electromagnetic shower initiated by a 1 PeV electron in the atmosphere. It shows the total (black) photon (orange), electron (blue) and muon (purple) counts for different depths X. The large dots near 1000 represent an observer at the surface.

As a final example we give the calculation time for showers initiated by electrons with different energies in figure 4.13. We include how modeling ionization and the LPM effect change the simulation time. Even in the worst case, when both have been switched on, an entire atmospheric cascade can be modeled in under 10 seconds. This time can be further cut down by compiling numpy using mkl or other cpu specific libraries.

4.4 Comparisons

In the following we compare results using EmCa, including all previously mentioned effects, to CORSIKA air shower simulations for highly energetic particles and EGS4 [91] for low energetic ones.

CORSIKA

We show a comparison between particle numbers taken from [50] and EmCa for two different low energy cuts in figure 4.15. On the left, the cut was set to 1 MeV and on the right to 1 GeV. EmCa shows a high agreement with the CORSIKA results in both cases. In the 1 MeV cutoff case, there is a discrepancy between the CONEX (CE) / Hybrid results and the CORSIKA (MC) / EmCa ones. In [50] this was attributed to three-dimensional effects and corrected with a scaling factor. Due to the agreement between EmCa and the CORSIKA results, without the need for such a scaling, we believe the differences are not due to any additional effects.

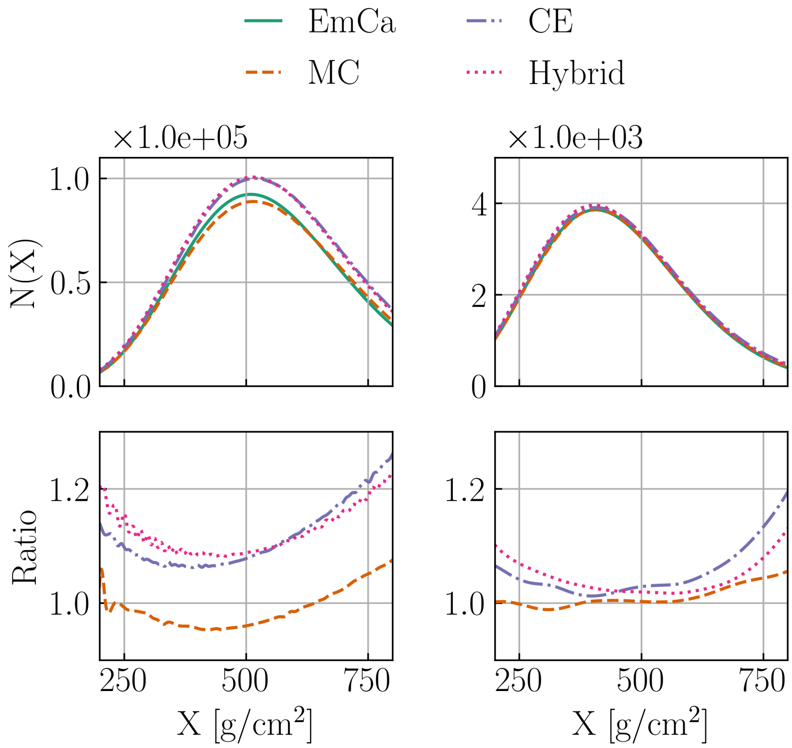

Figure 4.15: Comparison between the $e^- + e^+$ results from [50] and EmCa with a primary photon of 100 TeV. Left particles above 1 MeV were tracked and on the right particles above 1 GeV. Results using different methods were plotted: Monte Carlo (CORSIKA, yellow), cascade-equations (CONEX, blue), hybrid (CORSIKA + CONEX, pink) and EmCa (green). The deviations are calculated as a ratio to EmCa.

Additionally we compared the average development of the shower maximum, $X_{\max}$, of photon-initiated showers. In figure 4.16 a comparison between EmCa and the results shown in [92], where CORSIKA (MC) was used, is shown. The drop off in agreement at higher energies is a result of the approximation used in EmCa to treat the LPM effect, defined in equation 4.27. The theory line is calculated using the Heitler Model, in which the shower maximum is approximated by equation 4.4 which was

$$X_{\max} = X_0 \ln\left(\frac{E_{\text{prim}}}{E_{\text{crit}}}\right), \tag{4.42}$$

where for all calculations $E_{\mathrm{crit}} = 86$ MeV. In the theoretical model the LPM effect is not accounted for, which explains the discrepancy at high energies.

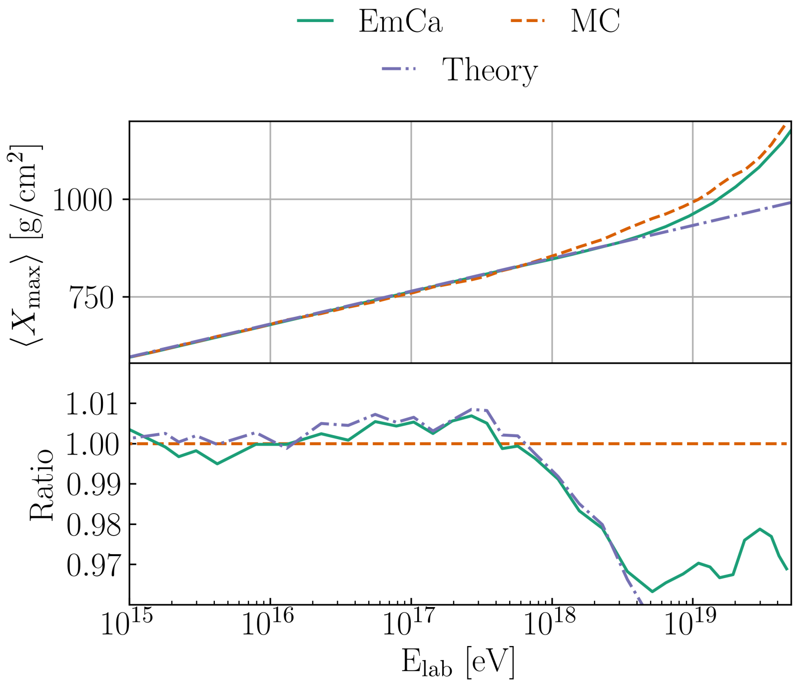

Figure 4.16: The development of $X_{\max}$ for photon-initiated showers dependent on energy are shown. The results using EmCa are compared to those from [92] using CORSIKA (MC). Ratios are shown in the bottom plot.

EGS4

In figure 4.17 we compare particle number calculations of EmCa and EGS4, in iron. The low energy cutoff was set to 1.5 MeV. In the simulation an electron with 30 GeV was injected into a uniform block of iron. The agreement between EmCa and EGS4 is very high.

These results show the precision of the EmCa package, while being computationally inexpensive. In the next chapter we will discuss how this can be used to test new models and their effects, such as the one presented here. Before that, we will give a short introduction of one possibility of expanding the cascade equations for the electromagnetic cascade to three dimensions.

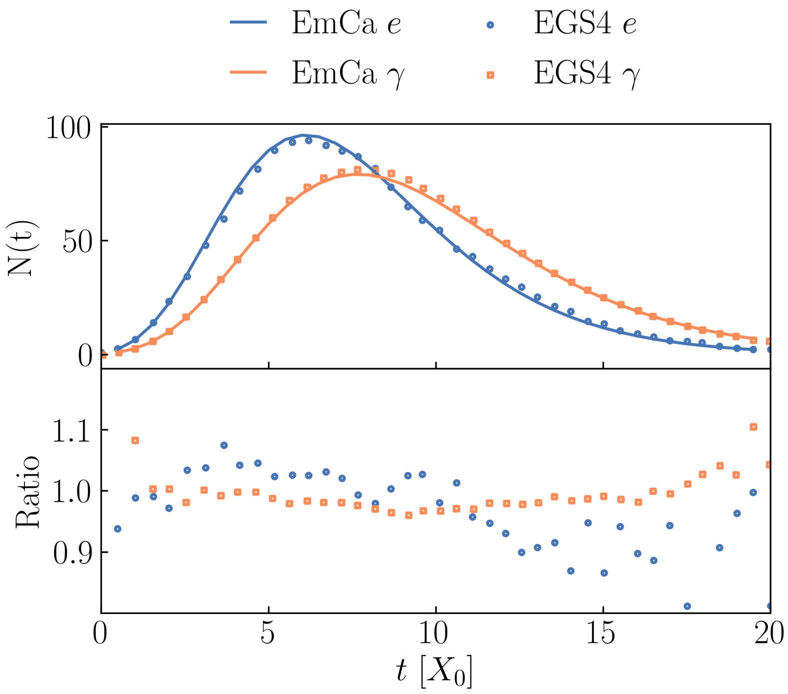

Figure 4.17: Comparison between the EGS4 and EmCa results of a electron initiated 30 GeV shower. Data for the EGS4 results are taken from [52]. The particle numbers between the simulations show a high agreement, with the deviation between the two being under 10% for most of the shower. The x-Axis is plotted in units of radiation length.

4.5 Three Dimensions

In this section a three dimensional treatment as outlined in [93] will be discussed and the steps necessary to adapt it to the matrix equation method are shown. We will introduce two approximations, starting with the Landau approximation.

Landau approximation

The three dimensional cross-section can be treated with the Landau approximation. In this approximation it is assumed that multiple scattering dominates (an infinite amount of small scatterings) and single scatterings can be ignored. In the Landau approximation the electron ($e^{\pm}$) and the photon flux cascade equation are written as

$$\partial_X \phi^i + \theta \partial_r \phi^i = \hat{\Gamma}^i_j \phi^j + \frac{E_s^2}{4E^2}(\partial^2_{\theta_1} + \partial^2_{\theta_2})\phi^i. \tag{4.43}$$

Where the operator $\hat{\Gamma}^i_j$ describes the losses and gains through particle interactions and ionization, as discussed in this chapter. Above Cartesian coordinates are used with $r = (x, y)$ and $\theta = (\theta_1, \theta_2)$. Additionally a small angle approximation was made in the derivation of the above equation leading to the lack of trigonometric functions. Since in the Landau approximation it is assumed that multiple scattering dominates the lateral distribution $\hat{\Gamma}^i_j$ will have no angular dependence and the small angle approximation is valid in this case.

Derivation

When charged particles pass through matter they will be deflected due to Coulomb scattering, which according to [93] is the main source for the lateral and angular spread of the shower. To add scattering to the photon flux, the Compton scattering interaction treatment would need to be extended. For now we assume this can be neglected. For the shower development, except at the very beginning, the opening angle for pair production and Bremsstrahlung should be negligible, especially since these processes are suppressed at low energies. Traversing a material of thickness x, the transport equation for the particle distribution function f is

$$\partial_x f = \int \left[f\left(\theta - \theta'\right) - f(\theta)\right] \sigma(\theta')\mathrm{d}\theta'. \tag{4.44}$$

Given the condition that the particle is injected at a specific angle θ at the start, the initial condition is $f = \frac{\delta(\theta)}{2\pi\theta}$ at $x = 0$. In the above equation $2\pi\theta'\sigma(\theta')\mathrm{d}\theta'\mathrm{d}x$ is the probability of the particle being deflected by an angle between θ' and $\theta' + \mathrm{d}\theta'$ while traversing $\mathrm{d}x$.
The scattering probability is given by the MOTT formula, in the small angle approximation by

$$2\pi\theta\sigma(\theta)\mathrm{d}\theta\mathrm{d}x \approx 4N_A \frac{Z^2}{A} r_0^2 \frac{m_e^2 c^2}{p^2\beta^2} \frac{2\pi\theta\mathrm{d}\theta}{\theta^4}\mathrm{d}x. \tag{4.45}$$

To solve the differential equation one applies a Hankel transformation and expands the Bessel function in a Taylor series. In order to be able to drop higher order terms in θ ($O(\theta^4)$) the scattering probability needs to have the form

$$2\pi\sigma(\theta)\theta\mathrm{d}\theta = \lim_{\alpha\to 0} \frac{E_s^2}{p^2\beta^2c^2}\frac{\delta(\theta-\alpha)}{\alpha^2}\mathrm{d}\theta, \tag{4.46}$$

where the scattering energy

$$E_s = \sqrt{4\pi 137} m_e c^2 \approx 21\mathrm{MeV}, \tag{4.47}$$

was introduced for simplicity. The above scattering probability means the calculations are only valid when one has an infinite amount of small scatterings and can not deal with discrete scattering processes. By expanding the differential equation

$$\int \left[f\left(\theta - \theta'\right) - f(\theta)\right] \sigma(\theta')\mathrm{d}\theta' = \frac{1}{4}\langle\theta^2\rangle \left(\partial_\theta^2 + \frac{1}{\theta}\partial_\theta\right) f + \ldots \tag{4.48}$$

with $\langle\theta^2\rangle = \frac{E_s^2}{p^2\beta^2c^2}$. The differential equation can now be written as

$$\partial_x f = \frac{1}{4}\frac{E_s^2}{p^2\beta^2c^2}\left(\frac{1}{\theta}\partial_\theta\theta\partial_\theta\right) f. \tag{4.49}$$

For the three-dimensional case this equation needs again to be solved for y. Performing the integral results in

$$f = \frac{p^2\beta^2c^2}{\pi E_s^2} e^{-\frac{p^2\beta^2c^2\theta^2}{E_s^2 x}}. \tag{4.50}$$

The normalized distribution function for different primary energies is shown in figure 4.18. As expected the "spread" rises for lower energies. For the calculation of the average spread of atmospheric showers this approximation should be more than sufficient.

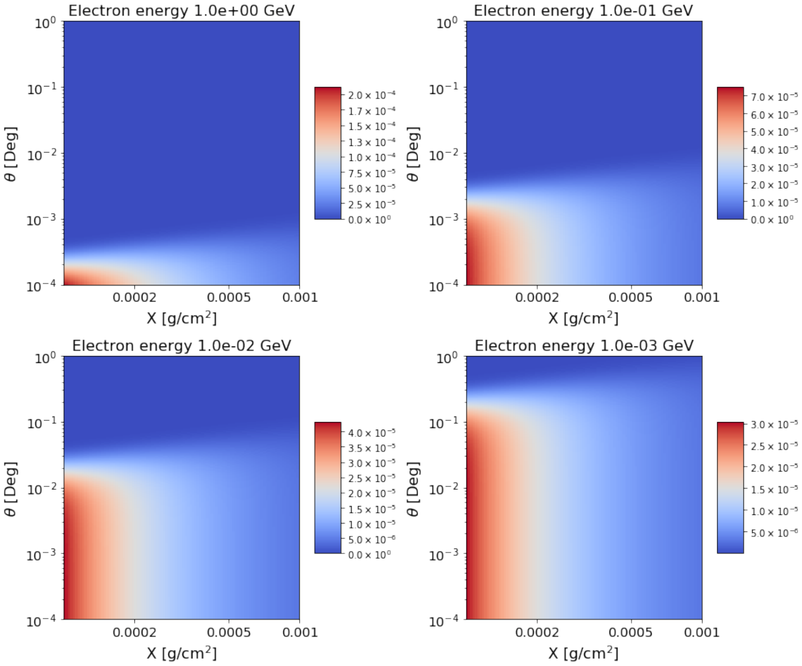

Figure 4.18: The theoretical angular spread of electrons passing through matter at different energies in the Landau approximation. The colors denote the scattered fraction of the total flux for a given scattering angle θ. The figures were normalize to one along the y axis.

Molière Treatment

Without the Landau approximation the integral from 4.44 cannot be solved as trivially and the general solution is

$$\partial_X \phi^i + \theta \partial_r \phi^i = \hat{\Gamma}^i_j \phi^j + \int \left[\phi^i(\theta - \theta') - \phi^i(\theta)\right] \sigma(\theta') \mathrm{d}\theta'. \qquad (4.51)$$

We will follow Molière in the treatment of this integral. His solution adds higher order terms to the one derived in the Landau approximation and rescales the scattering energy

$$f(\theta) = f^{(0)} + \frac{1}{\Omega} f^{(1)} + \frac{1}{\Omega} f^{(2)} + \ldots, \qquad (4.52)$$

where

$$f^{(0)} = \frac{1}{\pi} \frac{E^2}{K^2 x} e^{-\frac{E^2 \theta^2}{K^2 x}} \qquad (4.53)$$

with $K = \sqrt{\Omega} E_s'$. Furthermore Ω is defined by the equation

$$\Omega - \log \Omega = \log \left(\frac{E_s'}{E X_a} \right)^2 - 0.154, \qquad (4.54)$$

with

$$E_s' = \frac{E_s}{2\sqrt{\log(191 Z^{-\frac{1}{3}})}}, \qquad (4.55)$$

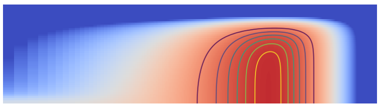

Figure 4.19: Cartoon of the lateral development of an electromagnetic shower. For this plot the emission angles were not tracked and only the distribution of electrons at each depth step is plotted. This is made using the Landau approximation.

and

$$X_a^2 = \theta_{min}^2 \left[1.13 + 3.76 \left(\frac{Ze^2}{\hbar c} \right)^2 \right]. \tag{4.56}$$

θ_{min} is the minimal possible scattering angle. Plugging in all definitions for air

$$\Omega_{air} = 15.2; \; K_{air} = 19.3\text{MeV}. \tag{4.57}$$

The first order term is

$$\frac{1}{\Omega} f^{(1)} \approx \frac{1}{4\pi \log(191 Z^{-\frac{1}{3}})} \left(\frac{E_s'}{E} \right)^2 \frac{x}{\theta^4}, \tag{4.58}$$

which describes the majority of the contribution from single scattering. The higher order terms drop off quickly and can be neglected. An example distribution is shown in 4.20. Note that the distributions are broader than their single scattering counterparts. The energy dependence remains similar.

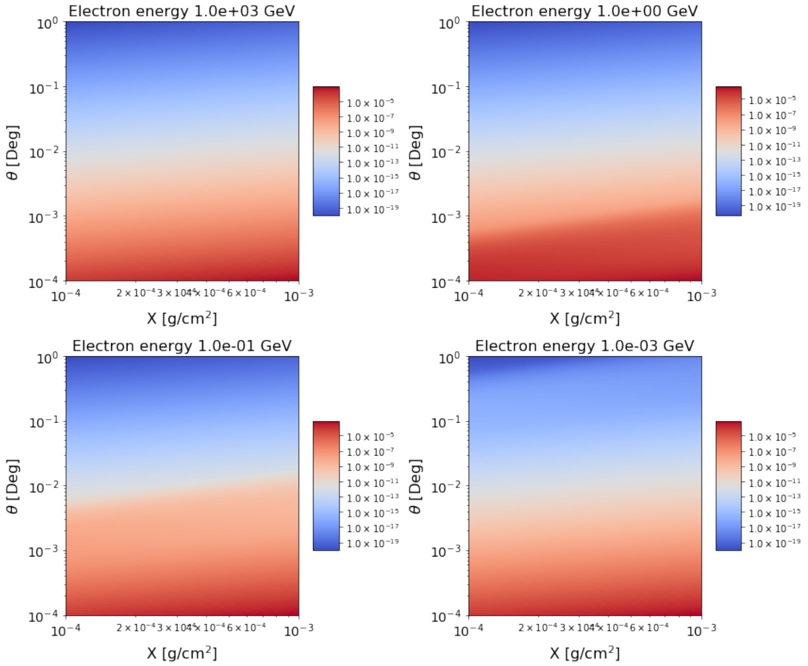

Figure 4.20: The theoretical angular spread of electrons passing through matter at different energies in the Moliere approximation. The colors denote the scattered fraction of the total flux for a given scattering angle θ. The figures were normalize to one along the y axis.

Numerical implementation

Adding the previously mentioned angular distributions to EmCa leads to figures 4.19. In that figure the angular spread of the particles was not tracked and only the distribution at each depth step is plotted. The next step is to allow for re-scattering, basically tracking of the angle and adding new scattering angles to it. This entails adding and subtracting the angles from the previous ones. Re-scattering will be treated by binning the flux at each step and adding the new scattering angles to it by re-binning. For that an algorithm needs to be defined. As a first step the scattering matrix is applied in each step and the resulting particles are re-binned to account for the previous angles. The Landau results are shown in figure 4.21. The Moliere results are shown in figure 4.22

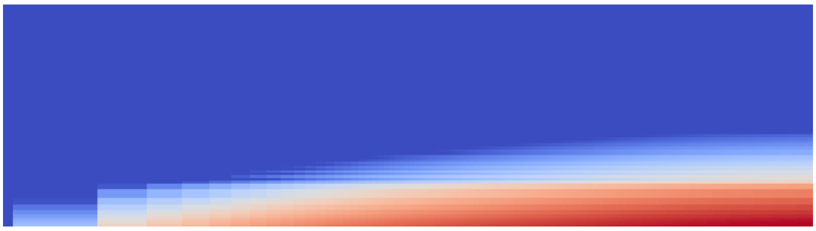

Figure 4.21: Cartoon of the lateral development of an electromagnetic shower in the Landau approximation. The colors correspond to the distribution of particles at a given depth point. Note that the shower shows a far lesser spread than the one modeled using the Moliere approximation in the plot below.

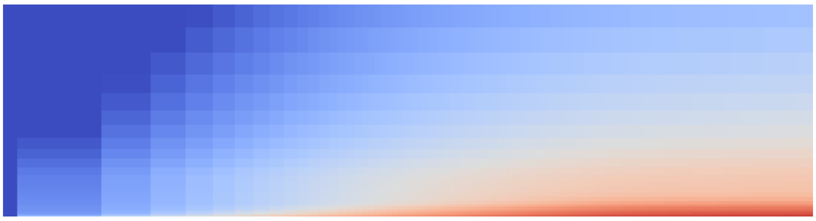

Figure 4.22: Cartoon of the lateral development of an electromagnetic shower in the Moliere approximation. The colors correspond to the distribution of particles at a given depth point. When compared to the Landau calculation, we can see the importance of single scattering. These single deflections contribute to more extreme cases of the lateral shower distribution.

This topic still requires further study and comparisons to experimental data. Currently these calculations are only implemented in the developmental version of EmCa. Should these methods work, 3D electromagnetic cascades could almost be modeled in full, without the need for Monte Carlo methods. The final component required to replace them, would be the stochastic nature of the particle shower, especially at the very beginning. Preliminary tests using stochastic differential equation seem promising but require further study.

4.6 Conclusions

Here we have introduced an entirely new framework dubbed EmCa, which provides new and old electromagnetic interaction models and is capable of solving cascade equations in different materials. We have shown that this framework is capable of modeling electromagnetic cascades as well as Monte Carlo methods, while also disproving that traditional discrepancies between cascade equation methods and Monte Carlo ones are due to 3D effects. The new model we have introduced has removed the usually required low energy cut-off, which is due to the infrared divergence of Bremstrahlung. We have done this by including material effects, specifically the dielectric effect, which suppresses the production of low energy photons. Finally we have shown the next steps, namely 3D modeling, which if pursued and successful, would make cascade equations nearly as versatile as Monte Carlo approaches.

In the next chapter, we will show the effect this new interaction model can have on cosmic ray experiments. Due to minor differences in screening treatment between Tsai and Bethe-Heitler models, the measured cascade energy by fluorescence experiments will shift.

Fluorescence from Electromagnetic Cascades

5

Models 49
5.1 Fluorescence 50
5.2 Results 51

As discussed in the previous chapter, EmCa provides three different interaction models, which we use to test the model dependence of atmospheric muons coming from electromagnetic cascades. They differ in their description of pair production and Bremsstrahlung. Here we will discuss how these differences change the shower's measured energy. Due to the differences in the charged atmospheric flux between the models, we also expect a change in the fluorescence. In the final section we will discuss these changes and their relevance to fluorescence experiments.

Models

Tsai's calculations offer a more precise and intrinsic treatment of screening effects, unlike cross sections based on Bethe and Heitler's calculations. This leads to discrepancies in the cross sections. The differential cross sections for pair production using the different models is shown in Figure (5.2). The major difference between the Tsai model using the full screening approximation (Base) and the others, is due to the approximation not being valid anymore for the production of sub GeV particles. The difference between the full Tsai model (Tsai) and the Bethe-Heitler (BH) results are the most relevant for the current discussion. While these discrepancies are minor, the large number of particles and interactions act multiplicative on them. Bremsstrahlung, unlike pair production, has only a very slight screening dependence. The difference between the models changes the rate, at which photons interact, increasing the number of

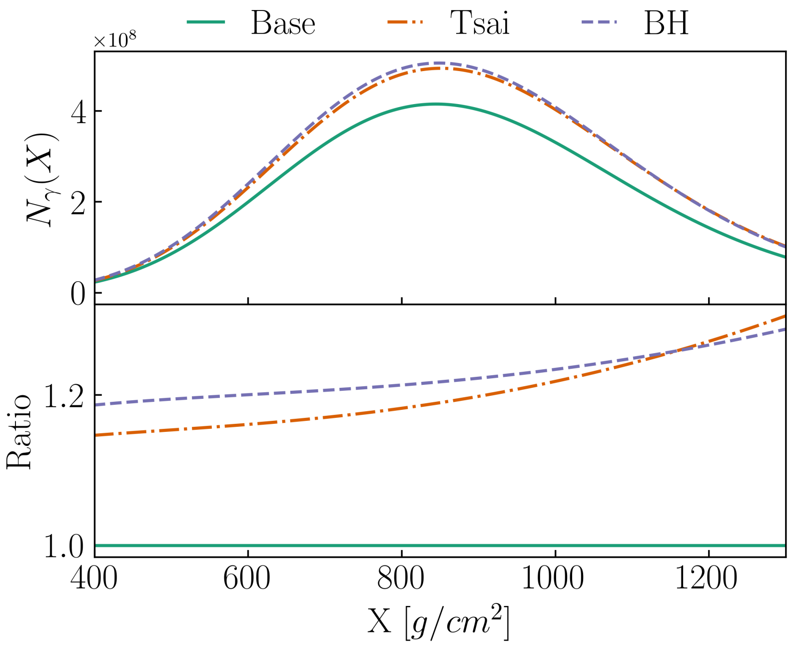

Figure 5.1: The number of photons in an atmospheric shower initiated by a primary 10 EeV photon. Green, solid shows the full screening approximation (Base), light orange dashed-dotted the full Tsai model (Tsai) and in purple dashed the Bethe-Heitler model (BH). The bottom plot shows the ratio between the photon numbers using the different models, with Base uses as the reference.

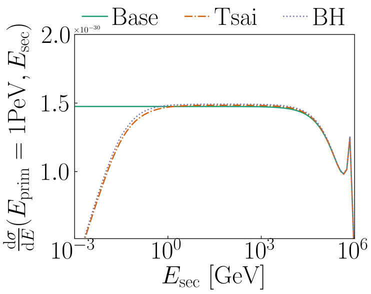

Figure 5.2: The differential cross section for pair production for the different models. Green, solid shows the full screening approximation (Base), light orange dashed-dotted the full Tsai model (Tsai) and in purple dashed the Bethe-Heitler model (BH). The primary photon's energy was set to 1 PeV.

photons when accounting for screening. This is shown in Figure (5.1) for an electromagnetic cascade in the atmosphere, initiated by a 10 EeV photon, where we set the cut off energy to 86 MeV. This is the critical energy E_{crit} according to Rossi [68]. Below which collision losses start to dominate the loss of electrons in air. The collision losses, for all models, are modeled using ESTAR [85]. The differences between the models shrink, when increasing the low energy cut off and increase when setting it even lower. The average difference between the full Tsai model and the Bethe-Heitler model is 2.5% for the depicted shower with a maximal difference of 3.7%.

5.1 Fluorescence

The fluorescence technique [94] is employed by multiple experiments, such as Auger [88] and TA [89], to measure the energy of a primary cosmic ray. Natural fluorescence occurs when particle showers pass through the atmosphere causing nitrogen to fluorescence. These emissions can in turn be used to estimate the total energy of the cascade. We run electromagnetic shower simulations to model the deposited energy, or calometric energy, E_{cal}, from fluorescence. The deposited energy is estimated as

$$E_{\text{cal}} = \alpha \int_0^\infty N_{\text{ch}}(X)\text{d}X. \tag{5.1}$$

In the above equation $N_{\text{ch}}(X)$ is the number of charged particles at a given slant depth X. In [94] $\alpha = 2.19$ MeV, which we also use. Here we give a quick introduction how one obtains this equation following [94]. In an electromagnetic shower, the primaries energy can be approximated by

$$E_{\text{em}} \approx \int_\epsilon^\infty \Delta E(k) N_e(k)\text{d}k. \tag{5.2}$$

Here k is the kinetic energy of the electrons, $N_e(k)$ their differential energy specturm and $\Delta E(k)$ their energy loss via ionization inside of a given detector. ϵ is the threshold energy of the detector, with the above equation becoming exact with $\epsilon \longrightarrow 0$. This equation can be rearranged to include the atmospheric shower slant depth X. To this end the differential energy spectrum N_e is written as a function of X

$$N_e(k) = \int_0^\infty N_e(X) n_e(k, X) \frac{\text{d}X}{\Delta X(k)}. \tag{5.3}$$

$\Delta X(k)$ is the mean free path of the electrons, $N_e(X)$ the total number of electrons and n_e the normalized energy spectrum. Plugging this into the definition of the shower's energy results in

$$E_{\text{em}} \approx \int_0^\infty N_e(X) \left(\int_\epsilon^\infty \frac{\Delta E}{\Delta X}(k) n_e(k, X)\text{d}k \right) \text{d}X. \tag{5.4}$$

Often the age parameter S instead of the slant depth X is used. It is defined as

$$S(X) = \frac{3(X - X_1)}{(X - X_1) + 2(X_{\text{max}} - X_1)}. \tag{5.5}$$

Here X_1 is the depth of the first interaction. The mean ionization loss rate $\alpha(S)$ of electrons is then

$$\alpha(S) = \int_{\epsilon}^{\infty} \frac{\Delta E}{\Delta X}(k)\tilde{n}_e(k, S)\mathrm{d}k. \tag{5.6}$$

With this we can rewrite the shower's energy as

$$E_{\text{em}} \approx \langle\alpha\rangle_S \int_0^{\infty} N_e(X)\mathrm{d}X. \tag{5.7}$$

We denote $\alpha = \langle\alpha\rangle_S$ for simplicity. This is the equation we will use in the next section to estimate the deposited energy.

5.2 Results

From figure 5.1 we already know that more photons are being produced in the Bethe-Heitler model than in the Tsai model. For this reason we expect, that less electrons are being produced in the latter model as well, since there are less photons available to produce them. Figure 5.3 confirms this expectation. Figure 5.4 shows the simulation results for the deposited energy. Here we assume the electromagnetic showers develop fully before reaching the detector. The differences between the Bethe-Heitler and Tsai models shown vary between 3% and 4%. This means currently, due to the Tsai model being a more exact model, EGS4 and by extension CORSIKA, estimate electromagnetic shower energies as too

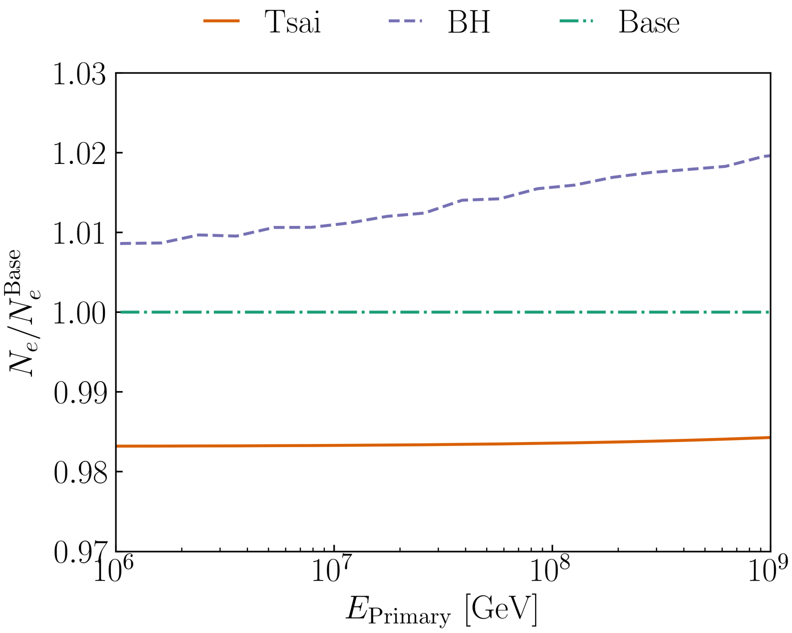

Figure 5.3: The total number of electrons for different primary energies when compared to the base model. Green, solid shows the full screening approximation (Base), light orange dashed-dotted the full Tsai model (Tsai) and in purple dashed the Bethe-Heitler model (BH). There is approximately a 3% difference in the electron counts between the Bethe-Heitler model and the Tsai model.

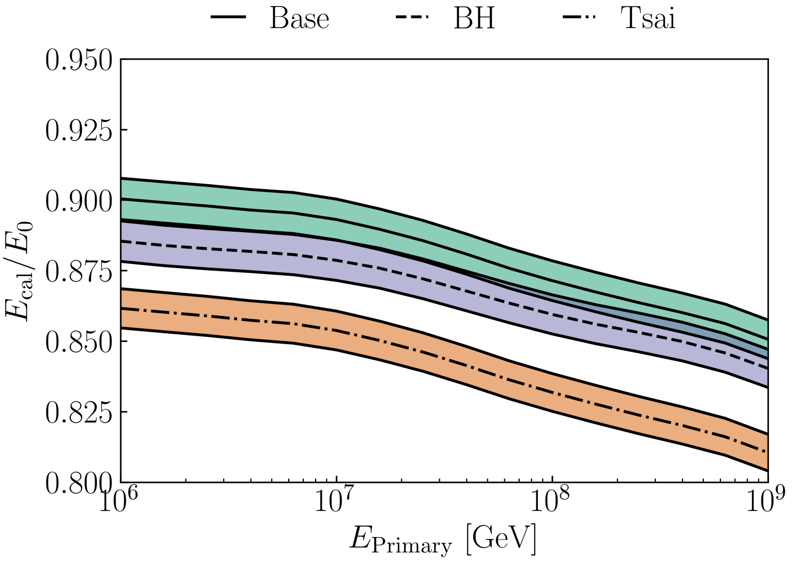

Figure 5.4: The deposited energy compared to the injected primary photon energy. Shown are the simulation results for fully developed showers for the different interaction models. We plot the effect a 1% shift in α causes using the bands. The different models are plotted as: Solid green, the full screening approximation (Base); Dashed dotted orange the full Tsai model (Tsai); Dashed purple the Bethe-Heitler model (BH). The Bethe-Heitler model and the Tsai model show a discrepancy of between 3% and 4%.

high. Since electromagnetic cascades provide the majority of fluorescent light, due to electrons comprising most of the charged particles in the course of a showers development, these discrepancies will also hold true for hadronic showers. The absolute unaccounted for error this causes in hadronic showers is difficult to quantify and requires further study.

This shows the need for exact shower modeling, even for electromagnetic showers, which traditionally have been thought of as completely understood. Using tools such as EmCa, allows for rapid benchmarking of new electromagnetic models and their implications for experimental measurements.

While we have treated traditional searches and modeling until now, in the next chapters we will show how exact modeling can be used to push the capabilities of neutrino detectors into new fields. In the next chapter we will use precise modeling of energy loss and particle production to set constraints on new physics using neutrino detectors, specifically the IceCube detector.

New Constraints on Supersymmetry Using Neutrino Telescopes

6

6.1 Production 54
6.2 Propagation 55
6.3 Background 57
6.4 Detector Response 57
6.5 Events 59
6.6 Energy and Angular Cut . . 60
6.7 Results 60

New long-lived particles are an integral part of many theories beyond the Standard Model (SM). Supersymmetry, for example, predicts the existence of the stau, the supersymmetric partner of the tau lepton. The stau is long-lived in scenarios in which the gravitino is the lightest among all supersymmetric partners, and the stau is the next-to-lightest. In this case, and provided R-parity is conserved, the stau can only decay into a gravitino and a tau lepton. The width of this decay is suppressed by the scale of supersymmetry breaking (for a review, see [95]). As a result, the stau lifetime can be as long as several seconds, minutes or even years, depending on the model parameters. The most sensitivity searches for the stau have been performed at the Large Hadron Collider by the ATLAS and CMS collaborations. Using the mass of the stau ($m_{\tilde{\tau}}$) as a free parameter, they reported $m_{\tilde{\tau}} \geq 430$ GeV and $m_{\tilde{\tau}} \geq 240$ GeV at 95% C.L. respectively [96]. For these limits in particular, the stau's mass is the only parameter of interest, due to the assumed Drell-Yan production.

Stau searches have also been proposed in the context of megaton-mass neutrino telescopes. Highly energetic cosmic particles (cosmic rays and neutrinos) colliding with nucleons in the Earth's atmosphere are capable of producing staus. These in turn would then appear as charged particles in the detectors. In particular, they would appear as charged particles propagating through the detector, so-called tracks. For such events, other particles producing charged tracks would act as a background, mainly atmospheric muons and muons produced by neutrinos. Figure 6.6 shows the relative fluxes at the surface. The orders of magnitude difference between the stau flux and background makes disentangling them difficult, even for a low stau mass of 100 GeV. The neutrino flux is divided into its primary contributors. These are the astrophysical flux, the conventional flux from the decay of π and K mesons and the prompt flux from the decay of heavier mesons. One proposed strategy to disentangle staus from the background is to search for stau pairs. Due to the highly relativistic boosting, the two staus would move in the same direction, cross the detector simultaneously, and thus give rise to two parallel tracks — a smoking-gun signature. [97, 98, 99, 100, 101, 102]. However, current telescopes can not distinguish these events from the overwhelming background, single tracks from cosmic ray muons ($hN \to \mu X$) and/or from charged-current muon neutrino interactions ($\nu N \to \mu X$), unless the two stau tracks have a large separation (in IceCube by $\sim$ 135 meters [103, 104]). Thus, the majority ($\sim$ 99.9 %) of the potential stau particles would go undetected.

In this chapter we discuss how neutrino telescopes, in particular IceCube, can exploit a different signature to observe, on a statistical basis, a stau signal. At the energies of interest, staus are expected to be significantly more penetrating than muons of the same energy, because they essentially do not lose energy through stochastic processes [101]. Hence, for nearly horizontal trajectories, tens of kilometers of ice shield IceCube from the vast majority of muons but not from staus. We thus search for an excess of track events over the background expected from muons crossing the detector horizontally at a zenith angles near ∼ 90°. In contrast to previous works, this new analysis does not rely on an identifiable double track signature and thus less stringent event selection criteria. We demonstrate the potential strength of the method by analyzing one year of publicly available IceCube data [105, 106]. In order to identify this stau component, we utilize differences in the corresponding energy and angular distributions compared to the contributions from muons.

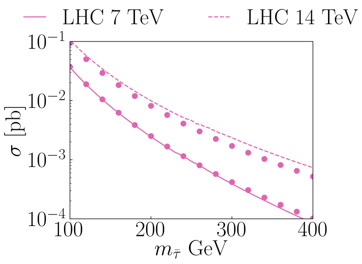

Figure 6.1: The stau cross section modeled using MadGraph's built in MSSM model. We compare the simulation results (dots) to those from [111] (lines) at different collision energies.

6.1 Production

We compute the stau production cross section using MadGraph [107, 108]. It is a tree level event generator modeling particle interactions based on a Lagrangian. It comes with a built in MSSM model, which we use to model the cross section. We interface MadGraph with the LHAPDF6 [44] library and use the CT10nlo [109] pdf and NNPDF30_nnlo_nf_5_pdfas from NNPDF3.0 [110]. Here we assume pure Drell-Yan production. Figure 6.1 shows the resulting cross sections for two LHC energies when compared with the calculations from [111]. Our simulations lie slightly under their calculations, making our estimates conservative.

We then require the total cross section of hadrons with air. We follow the parametrization used in [112]. For energies above 10 TeV, the total hadron-air cross section can be approximated by

$$\sigma_{h\mathrm{air}} \approx C_0^h + C_1^h \ln\left(\frac{E}{\mathrm{GeV}}\right) + C_2^h \ln^2\left(\frac{E}{\mathrm{GeV}}\right). \tag{6.1}$$

The C_i^h depend on the hadron of choice. The parameters for the above equation are given in table 6.1. Plugging these parameters into equation

Table 6.1: The parametrization used for the hadron air total cross sections.

h	C_0^h [mb]	C_1^h [mb]	C_2^h [mb]
N	185.7	13.3	0.08
π	100.5	16.9	0.00
N	79.7	13.9	0.05

6.1. Note that the total cross sections are in the mb range, while the stau production cross section is in the pb range. For this reason the energy deposit into this new BSM component can be neglected when averaging over multiple particle showers. For single showers this is not the case. Should staus be produced, we would expect that most of the primaries' energies is deposited into their production. For this reason a more precise analysis could use the lack of other arriving particles to discern a stau signal. This approach requires an in-depth understanding of the used detector, which escapes the scope of this thesis. Since the stau cross section is marginal when compared to the total cross sections with air, the probability of producing a stau in a collision is

$$P_{\tilde{\tau}}^{\mathrm{h}}(E) \approx \frac{A\sigma_{\tilde{\tau}}^{\mathrm{h,nucleon}}}{\sigma_{\mathrm{total}}^{\mathrm{h,air}}}. \tag{6.2}$$

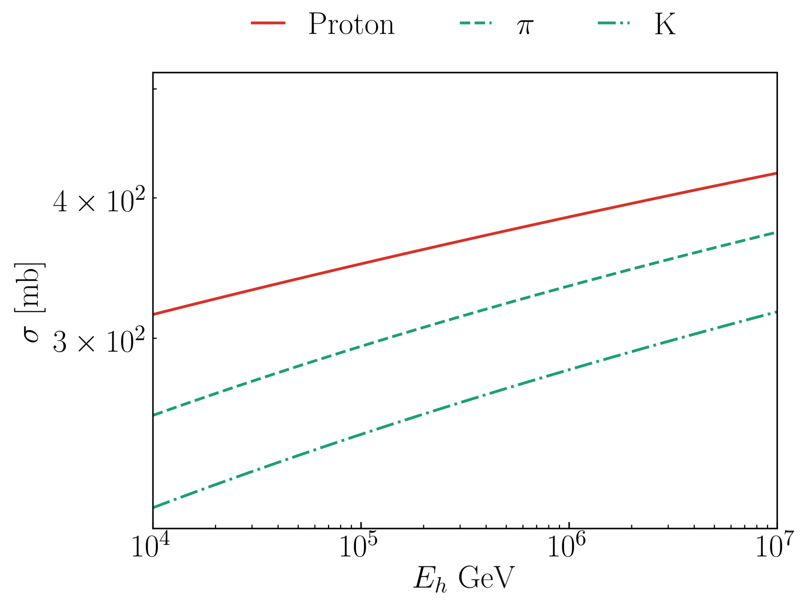

Figure 6.2: The hadron-air cross sections using the approximation from equation 6.1. Note that these are on the mb scale, while the stau cross sections is in the range of pb.

where $\sigma_{\tilde{\tau}}^{\text{h,nucleon}}$ is the total stau production cross-section from the collisions of a hadron h with a nucleon in the atmosphere, $\sigma_{\text{total}}^{\text{h,air}}$ is the total cross-section of h with air, and $A = 14.6$ is the average number of nucleons in a nucleus of air. This production probability needs to be folded with the number of hadrons in the atmosphere at different shower depths. To model their fluxes we use MCEq.

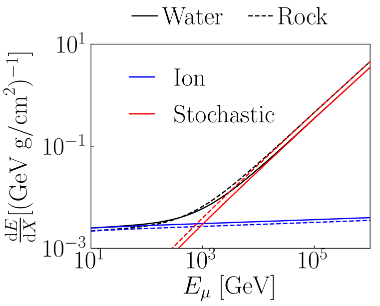

Figure 6.3: The energy loss of the muon according to [113, 114, 115] for water and rock. In red we show the radiative or stochastic losses of the muon, while in blue the ionization losses. The crossing point of the two is termed the critical energy point E_{crit}.

6.2 Propagation

After production we now need to propagate the staus to the detector. This requires propagation through the atmosphere, rock and, in the case of IceCube, through the ice. The average energy loss of a particle traversing a distance X is given by [101]

$$-\frac{\mathrm{d}E}{\mathrm{d}X} = a(E) + b(E)E, \tag{6.3}$$

where a and b are dependent on the material and particle. $a(E)$ describes the ionization or collision losses of the particle while $b(E)$ the radiative or stochastic losses. Ionization losses are at first order independent of the particle's mass meaning we can use the same $a(E)$ as for muons. Concerning $b(e)$, there are three contributing interactions. Pair production of electrons, Bremsstrahlung and photonuclear interactions. The first two have already been discussed for muons and electrons, with equation 4.17 and equation 4.19 describing these processes for muons specifically. From these two equations we can already see, that the differential cross sections scale as

$$\frac{\mathrm{d}\sigma^{\text{Pair}}}{\mathrm{d}E} \propto \frac{m_e}{m_l}, \quad \frac{\mathrm{d}\sigma^{\text{Brems}}}{\mathrm{d}E} \propto \left(\frac{m_e}{m_l}\right)^2, \tag{6.4}$$

where m_l is the mass of the particle of interest. This makes the energy loss due to Bremsstrahlung negligible when compared to pair production for

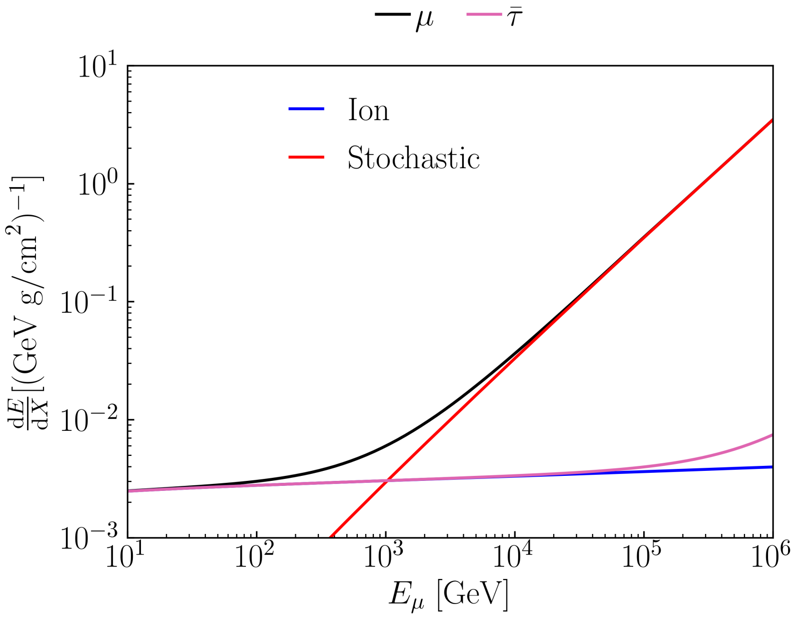

Figure 6.4: The energy loss of the stau using the scaled muon losses for water. In red we show the radiative or stochastic losses of the muon, while in blue the ionization losses. The total muon loss is shown in black, while the stau's loss in pink.

the stau of high masses ($m_{\tilde{\tau}} > 100$ GeV). This leaves pair production and photonuclear interactions. From[101] we see that the photonuclear cross section scales as m_l/m_e as well, putting it on par with pair production. This means the stau's energy loss can be approximated by the scaled muon energy loss

$$-\frac{dE_{\tilde{\tau}}}{dX} = a_\mu(E) + b_\mu(E)E\frac{m_\mu}{m_{\tilde{\tau}}}. \tag{6.5}$$

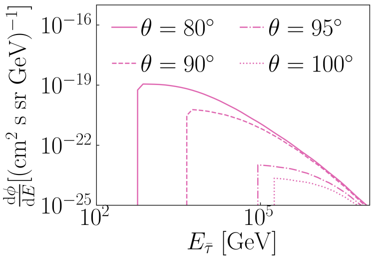

Figure 6.5: Here we show the stau flux at the IceCube detector for different zenith angles. There is a large drop in the flux between 90° and 95° degrees zenith angle. This is due to the additional rock the staus have to pass through.

We can now compare how the stau lose energy, which we show in figure 6.4. There we see that the staus' energy loss follows the ionization losses of the muon closely for most energies. By solving the above differential equation we can now calculate the loss of staus between their production point and the detector. While the stau lose very little energy when passing through material, for large zenith angles θ, the amount of material they need to pass through to reach the IceCube detector can exceed 100 km. For this reason at very high angles, below the horizon, we expect a sharp drop in the stau flux. Figure 6.5 shows this.

Due to the difference in the energy loss between muons and stau, we expect the stau to survive passing through far more material than the muons. This means with enough material, we would expect the staus to be the only charged particle reaching the detector. For this reason, in the following search not muons produced in the atmosphere, but muons produced by neutrino interactions will be the dominant background.

Additionally, due to the low energy loss by the staus, they will appear as minimally ionizing track, regardless of their mass. For this reason, the IceCube detector will reconstruct them as low energy muons with energies ranging between 500 GeV and 1 TeV. These values are simply due to the size of the IceCube detector and the corresponding amount of energy the staus can deposit therein.

6.3 Background

The background is composed of muons that produce a detector response indistinguishable from that of the staus. The muon backgrounds can be divided into two components according to whether muons are produced by a hadronic interaction in a cosmic ray airshower or by a neutrino interacting in the Earth. We simulate these contributions similarly to what we do for the staus. In addition to the cosmic-ray flux and composition used before, we now also include the flux of astrophysical neutrinos measured by IceCube [116]

$$\frac{\mathrm{d}\phi}{\mathrm{d}E} = 1.66^{+0.25}_{-0.27}\left(\frac{E}{100\ \mathrm{TeV}}\right)^{-2.53\pm0.07} \times 10^{-18}\ \left[\mathrm{GeV}^{-1}\ \mathrm{cm}^{-2}\mathrm{s}^{-1}\mathrm{sr}^{-1}\right]. \quad (6.6)$$

Combining these terms we can now show the different fluxes compared to the stau flux at the surface above the IceCube detector. Figure 6.6 plots this. From there we can see that the stau flux lies far below the other particle fluxes. This makes some additional steps necessary if we wish to constrain the stau flux.

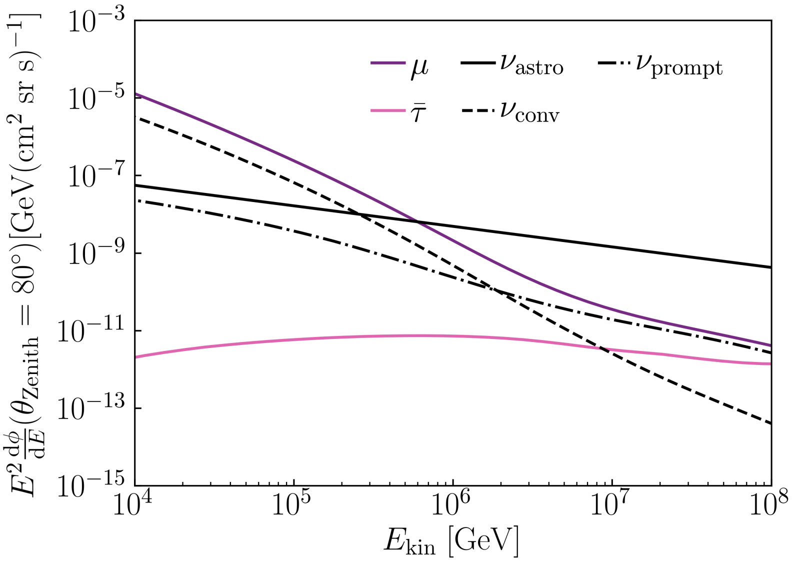

Figure 6.6: The different flux components at the surface above IceCube. We have included the predicted stau flux at 100 GeV mass. The black lines indicate the different neutrino components, astrophysical, conventional and prompt. The purple and pink lines show the muon and stau surface flux respectively.

6.4 Detector Response

To make a realistic prediction on the number of staus measured by the IcCube detector, we require three components. The energy reconstruction, angular reconstruction and effective area.

We include the effects of energy reconstruction as described in [117, 118] by constructing a function, mapping the true particle energy, E_{true}, to the reconstructed energy, E_{reco}, of the form

$$E_{\mathrm{reco}} = \begin{cases} \mathrm{LogNorm}(E_{\mathrm{true}}, \sigma_1, \mu_1) & E_{\mathrm{true}} < 1\ \mathrm{TeV} \\ \text{Linear interpolation} & E_{\mathrm{true}} \in [1, 10]\ \mathrm{TeV} \\ \mathrm{LogNorm}(E_{\mathrm{true}}, \sigma_2, \mu_2) & E_{\mathrm{true}} > 10\ \mathrm{TeV} \end{cases}. \quad (6.7)$$

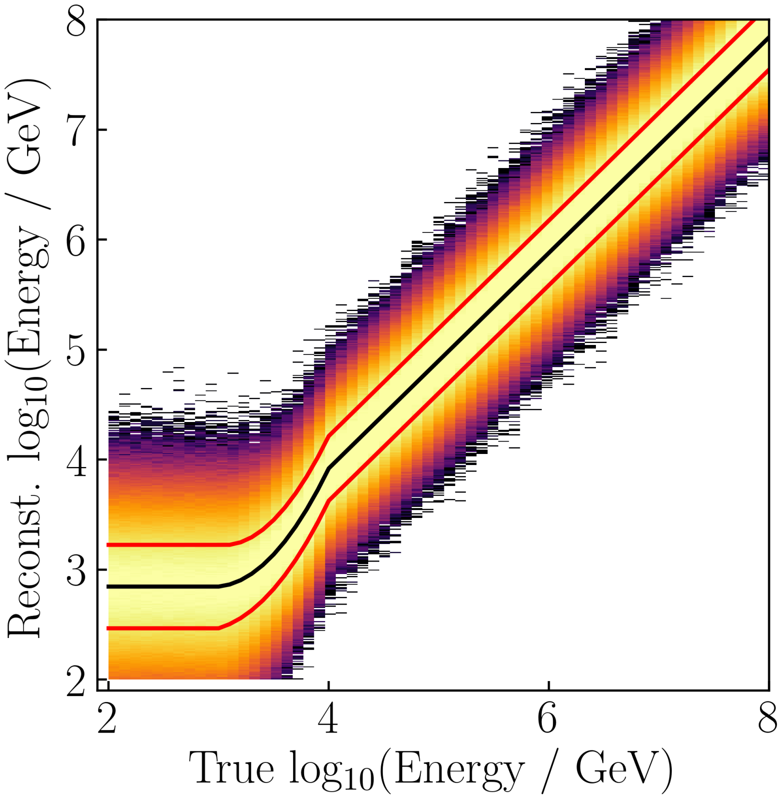

Figure 6.7: Our IceCube energy reconstruction model. Plotted are the probabilities of the reconstructed energy compared to the true energy. In black we show the mean value and in red the 1 σ deviation. Note the bias at low energies, which is relevant for the stau events, since we expect them to appear in these bins.

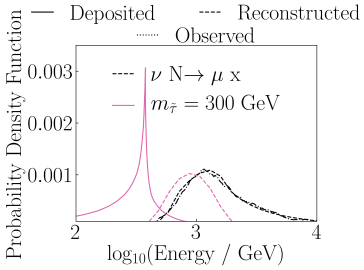

Figure 6.8: We plotted the deposited, reconstructed and observed energy distributions for the IceCube detector. The dotted lines represent the observed distribution, while the dashed lines the simulated ones. Note that we expect a slightly different energy distribution from the stau events when compared to those from neutrinos.

To get the specific values for σ and μ, we fitted the background prediction to the data for energies above 1 TeV. For such energies we do not expect any stau events. The results are $\sigma_1 = 0.4$, $\mu_1 = 700$ GeV, $\sigma_2 = 0.3$ and $\mu = E_{\mathrm{true}}$. The energy reconstruction distribution is shown in figure 6.7. These values agree well with those shown in [117]. To map the stau energies to their reconstructed energies, we map their energy deposit to muon energies with an equivalent loss according to equation 6.5 and then proceed as with the muons. Note that at low energies the reconstruction shows a bias towards higher energies. Since we expect most staus to fall into this category, they will usually be reconstructed with a higher energy, than they should be. This value is approximately 700 GeV. Applying this reconstruction to the simulated events we can compare the deposited energies, the reconstructed energies and the observed ones from data. In figure 6.8 we show the simulated and observed energy distributions. The reconstructed stau distribution is centered around 700 GeV in a Gaussian shape, slightly different from the standard model distribution shown in black. The latter of which agrees well with the observed one in data.

For the energy range of interest, $E \in [100\text{ GeV}, 1\text{ TeV}]$, the resolution with which IceCube can reconstruct this angle is 1°[119], and this is folded into our simulations by smearing the particle arrival directions accordingly. To calculate the contribution of neutrino-induced muons, we fold the 2D effective area, as a function of energy and declination, from [106] with the neutrino fluxes. The neutrino energy to muon energy mapping is approximated using the normalized 3D effective areas given in [118].
To make predictions for the stau component, we require a detector response to staus. We use the same approach as for the muons and divide the convolution by the total neutrino cross-section. The resulting

efficiency includes effects of muon propagation in the ice. These we compensate by scaling the results, so at 1 TeV the effective area for muons corresponds to the spatial area of the detector, 10^6 m^2. This results in a signal efficiency of 78%

6.5 Events

After re-sampling the flux with the previously mentioned angular and energy resolutions and folding the effective areas with the particle fluxes we obtain realistic event counts for the IceCube detector. Figure 6.9 shows the binned total event counts in one year before applying any cuts. As expected the muons show a steep drop towards higher angles, since they can not pass through the increasing amount of material. The staus are able to pass through it mostly unhindered, showing a flat distribution, only dropping of near the horizon. Before cuts, the staus still lie far below the expected background. Note that most of the background events are from atmospheric neutrinos. At these energies they provide most background events, while at higher energies we would expect the astrophysical ones to dominate.

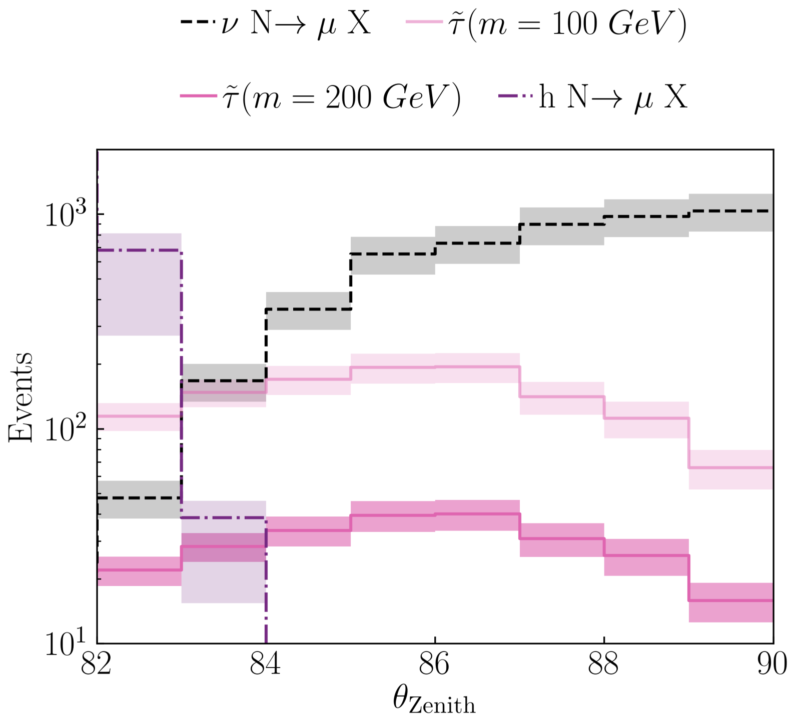

Figure 6.9: The total number of events binned in angle before cuts. We see the hard drop of atmospheric muons on the left, with the enhancement of neutrinos towards the horizon. The stau events still lie far below the expected background events for most angle bins.

Note the steep drop in stau events when increasing the mass. Since the production probability scales approximately with $m_{\tilde{\tau}}$ an increase of 2 in mass reduces the expected event count by approximately 4.

6.6 Energy and Angular Cut

As discussed previously, we expect most stau events to lie in the energy bin $E \in [100\ \text{GeV},\ 1\ \text{TeV}]$, as shown in figure 6.8. We use this and apply a hard energy cut of 1 TeV. While this is not the most efficient method, it does make our analysis robust against unaccounted for detector uncertainties. This cut leaves the stau count relatively untouched, while reducing the neutrino background by approximately a factor of 4.
We then apply angular cuts and require the reconstructed angle to follow $\theta_{\text{reco}} \in [85°, 90°]$. This are extremely hard cuts, since we expect the background to signal ratio to be optimal between 82° and 85° degrees with the optimum lying at 83°. Since we are working with public data, the reconstruction for down-going events ($\theta > 85°$) is difficult to reproduce. For this reason we choose a lower limit of 85°, since at those angles we expect the atmospheric muon background to be at most sub-leading.

6.7 Results

After applying all cuts, we arrive at figure 6.10. The ratio between background and signal events is now far more promising. Comparing our simulation results to data, the data points follow well the background-only distribution. The p-value of our data given the background-only hypothesis is 0.1, supporting our intuition that there is no evidence for a signal. Assuming the currently leading experimental limit on the stau mass ($m_{\tilde{\tau}}$ =430 GeV), we expect to retain 8 stau events. To extract a limit on the mass of the staus we perform a binned likelihood fit of the data shown in figure 6.10. The fit has one free parameter, the mass of the stau particle. The rates of the background components are fixed by our modeling. The best fit results in 0 stau events. Inverting a standard

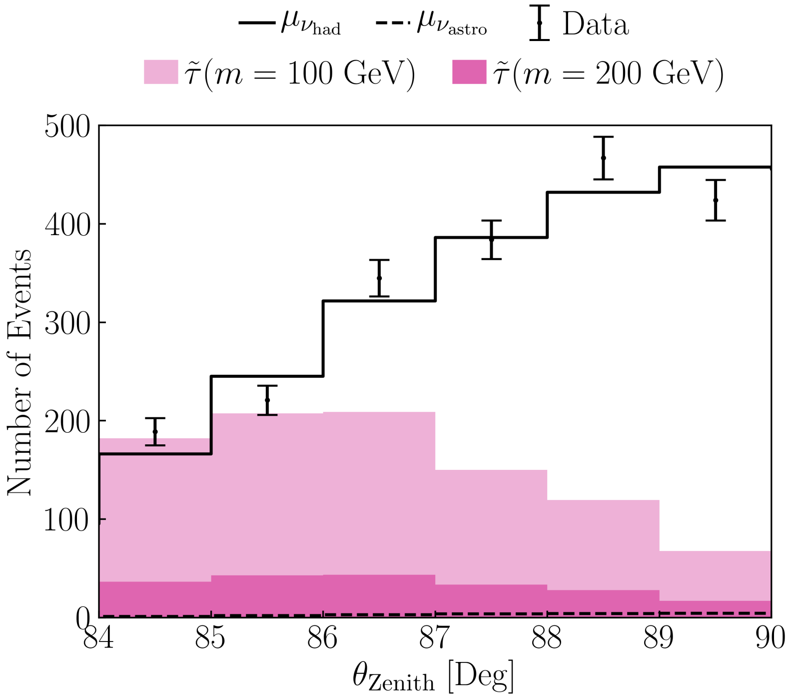

Figure 6.10: The number of events after applying energy and angular cuts. We include the 1 year publicly available IceCube data. Note the strong reduction in background events when compared to figure 6.9.

frequentist hypothesis test [120], we set a lower bound on the stau mass of $m_{\tilde{\tau}} > 320$ GeV at 95% C.L. This lies approximately 10% above the expected limit from simulations.

This type of analysis will only become better over time, due to the increasing exposure time of IceCube. In figure 6.11 we predict the limit setting capability of IceCube with more exposure time. From this we see that with the currently available data set of ten years, IceCube is capable of competing with collider constraints [96], being capable of setting a 450 GeV lower mass bound. This means neutrino detectors offer not only complimentary constraints on new physics, but are also capable of setting the most stringent limits. Furthermore, several neutrino telescopes, such as P-ONE [12], KM3NeT [13], GVD [14] and IceCube-Gen2 [121], are currently taking data or are in preparation. While their designs are different, they are all based on the detection of the Cherenkov light emitted by charged particles traveling through water or ice. The analysis performed in this work using data from IceCube can be extended to these upcoming datasets as well. Finally, this search strategy is not limited to the stau particle but can be utilized to search for other long-lived, charged particles beyond the Standard Model.

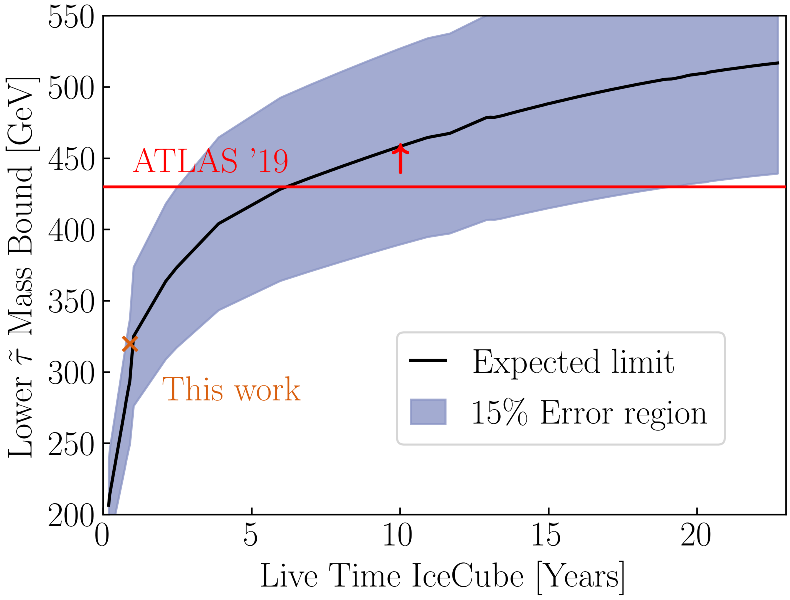

Figure 6.11: The increasing limit setting capability of IceCube with time. Here we also show the currently most stringent constraint on the stau mass set by ATLAS [96]. From this we can see, that with ten years of data, which are currently available, IceCube is capable of competing with collider constraints.

We can now move away from direct measurements of beyond the Standard model physics and move to indirect detection. In the next section we will predict IceCube's sensitivity to a new antiproton component, which could be produced by the decay of dark matter.

Antiprotons | 7

7.1 Decaying Dark Matter 63
7.2 Atmospheric Showers 65
7.3 Astrophysical Neutrinos . . 65
7.4 Results 65
7.5 Conclusion 68

Previously we discussed how the primary cosmic ray flux is modeled, see Section 2.1. There are known additional sub-leading components, such as antiprotons. These have been measured for energies below 100 GeV, for example by AMS-02 [122]. For higher energies only upper limits exist e.g. by HAWC [123] and ARGO-YBJ [124]. Here, we discuss the possibility and sensitivities of IceCube to constrain the antiproton flux at high energies. This is a relevant topic for the study of high energy cosmic ray composition and dark matter. In the latter case, there are models which for example predict that decaying dark matter produces a new source of antiprotons. In the next section we will roughly outline this process.

7.1 Decaying Dark Matter

Dark matter may accumulate in halos around massive objects, such as our galaxy. Here, we estimate the arriving antiproton flux from decaying galactic dark matter (DM) following [125]. Assuming a cylindrical stationary diffusion model [126], the flux of antiprotons, $\phi_{\bar{p}}(T)$, with kinetic energy T, is given by

$$\phi_{\bar{p}}(T) = \frac{v(T)}{4\pi} G(T) \frac{\mathrm{d}N}{\mathrm{d}T}(T). \tag{7.1}$$

Here v describes the velocity, G the Green's function and $\mathrm{d}N/\mathrm{d}T$ the source spectrum. We assume the DM decays as

$$\chi \rightarrow W^{\pm} l^{\mp} \tag{7.2}$$

and use the PYTHIA MonteCarlo event generator version 8.3 [45] to estimate the antiproton source spectrum. Using the MIN, MED and MAX propagation models [127], the Green's function can be parametrized as [125]

$$G(T) = \exp\left(a_0 + a_1 \log(T) + a_2 \log(T)^2 + a_3 \log(T)^3\right) \times 10^{14}\ \mathrm{s}. \tag{7.3}$$

Figure (7.1) shows the resulting flux of antiprotons arriving at the Earth. While the potential flux of high energy antiprotons decreases with rising energy, the proton spectrum drops faster. This leads to an increasing ratio between the primary proton and antiproton fluxes, shown in Figure (7.2). The increasing ratio between $\bar{p}$ and p is due to the lack of acceleration mechanisms at ultra high energies. Decaying dark matter would be the main contributor of protons and antiprotons at these very high energies. For the sensitivity study we will use the decay of W bosons as the source of antiprotons, motivated by models such as the one described in this section. This allows us to introduce a more realistic primary spectrum of antiprotons, should such a source exist.

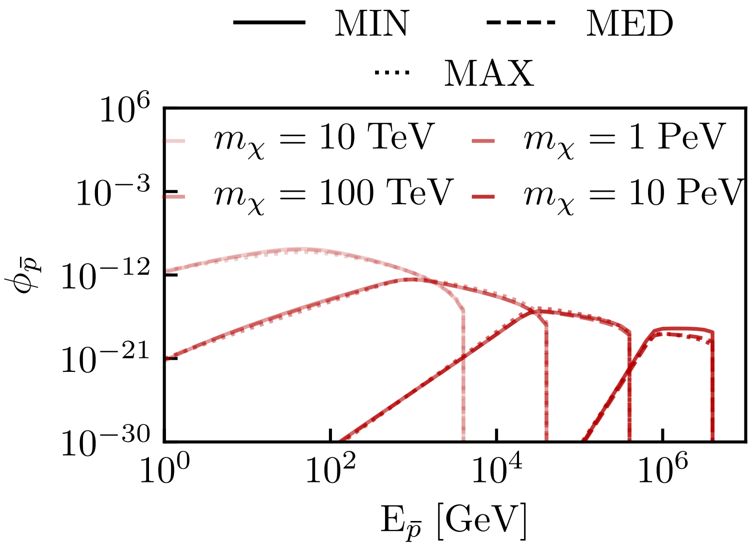

Figure 7.1: The predicted antiproton flux at earth, produced by DM with mass m_χ. The shape of the spectra remains similar for all masses, with only the position shifting according to the DM mass. Here the different propagation models, MIN, MED and MAX are shown as solid, dashed and dotted lines respectively.

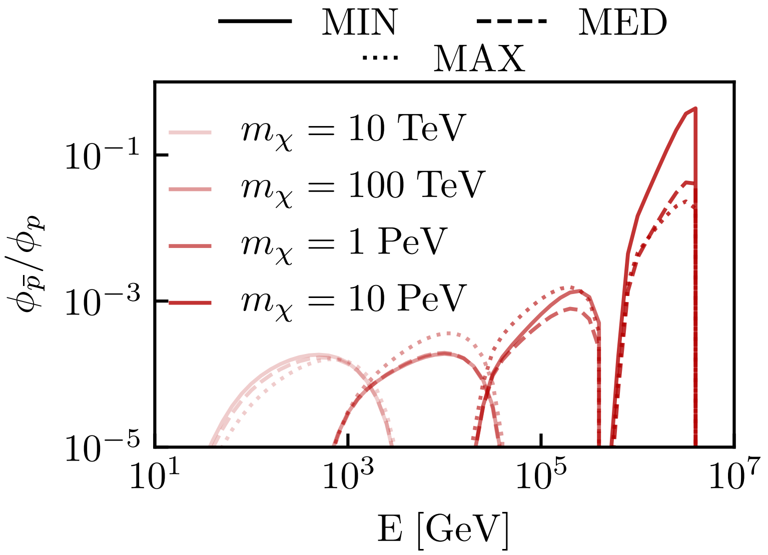

Figure 7.2: Ratio of antiprotons to protons at earth, assuming different dark matter masses. The ratio increases with increasing dark matter mass. Here, the different propagation models, MIN, MED and MAX are shown as solid, dashed and dotted lines respectively. Furthermore we use the H4a cosmic ray model [128].

7.2 Atmospheric Showers

For the propagation and showering of particles in Earth's atmosphere we use MCEq [51]. It solves cascade equations, see Section 2.2. We use the four population model H4a [128] as a primary model and SIBYLL2.3c [28] and EPOS-LHC [29] as interaction models.

7.3 Astrophysical Neutrinos

In addition to neutrinos produced by atmospheric showers, the main contribution in the high energy regime, are astrophysical neutrinos. As measured by IceCube [116], the astrophysical flux ϕ_ν^{astro} is given by

$$\frac{\mathrm{d}\phi}{\mathrm{d}E}(E) = 1.66^{+0.25}_{-0.27}\left(\frac{E}{100\ \text{TeV}}\right)^{-2.53\pm0.07} \times 10^{-18}\ \left[\text{GeV}^{-1}\ \text{cm}^{-2}\text{s}^{-1}\text{sr}^{-1}\right]. \tag{7.4}$$

This is the same flux we used in the stau analysis in the previous Chapter 6.

7.4 Results

As discussed in section 1, there is no signature difference between $p - p$ and $\bar{p} - p$ interactions at very high energies. For this reasons IceCube is not capable of discerning a difference between the two fluxes when purely measuring the isotropic neutrino flux. For this reasons the constraint IceCube is capable of setting is purely on an additional hadronic component, which may be composed of antiprotons. Figure 7.3 shows an example result when injecting a new hadronic component, h, at the top of the atmosphere. There, the additional component causes a large deviation to the traditionally expected neutrino flux. We can increase the injection spectra even further, and reproduce the astrophysical neutrino flux, as seen in Figure 7.4. While this contradicts neutrino measurements at lower energies, where the atmospheric flux dominates, the high energy neutrino flux, as measured by IceCube, could be explained in part by a new highly energetic h component. We can then interpret this new flux as being purely composed of antiprotons for the purposes of comparing with other experiments.

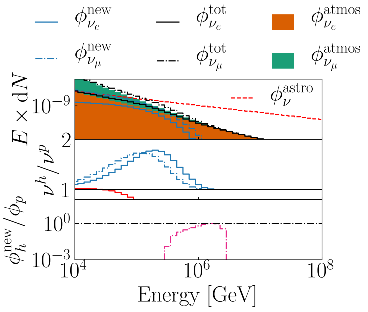

Figure 7.3: Predicted neutrino spectra from atmospheric showers with and without an additional h component. We have included the astrophysical neutrino flux (red). Here we are injecting a new h component in the shape of the secondary spectra from W decay. We show the electron and muon neutrinos using solid bar plots, orange and green respectively. The new flux caused by the h component is shown in light blue and the total resulting flux in black. The top plot shows the absolute values. The middle plot shows the ratios between the atmospheric (blue) and astrophysical (red) when including antiprotons. The bottom plot shows the injected h spectrum when compared to the cosmic ray proton flux.

To calculate IceCube sensitivities using 10 years of data, we introduce a low energy-cut of 1 TeV and restrict ourselves to $\theta_{\text{Zenith}} \in [0°, 90°]$, so-called down-going tracks. This avoids the difficulty of propagating the ν through the earth. Including higher angles would increase the sensitivity. We assume a flat effective area of 1 km^2 for all energies and angles. To set limits on the ratio between h and p, we invert the standard frequentist hypothesis test [120]. This results in Figure 7.5. There we show that IceCube is capable of setting limits of approximately 1 and 1/100 with 95% and 68% respectively for energies below 1 PeV. These would be the only and most stringent constraints on the ratio at these energies.

We can now compare the predicted IceCube limits to those set by HAWC [123] on the antiproton flux, shown in figure 7.6. The limits IceCube is

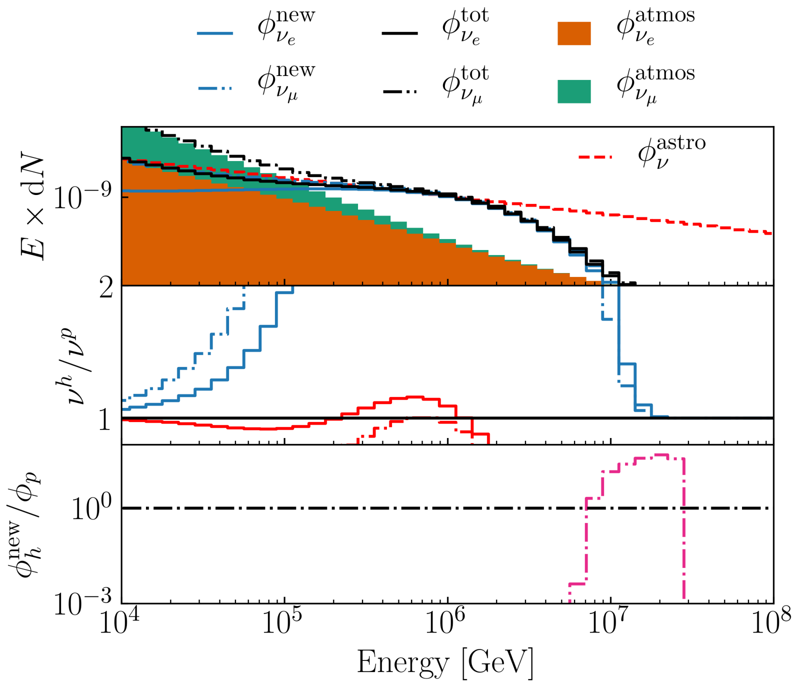

Figure 7.4: Predicted neutrino spectra from atmospheric showers with and without an additional h component. We have included the astrophysical neutrino flux (red). Here, we are injecting a new h component in the shape of the secondary spectra from W decay. We show the electron and muon neutrinos using solid bar plots, orange and green respectively. The new flux caused by the h component is shown in light blue and the total resulting flux in black. The top plot shows the absolute values. The middle plot shows the ratios between the atmospheric (blue) and astrophysical (red) when including antiprotons. The bottom plot shows the injected h spectrum when compared to the cosmic ray proton flux. Here we approximately reproduce the astrophysical neutrino flux, using a new h component.

capable of setting are less stringent at low energies than HAWC, but reach to far higher energies. At extremely high energies the astrophysical neutrino flux limits IceCube's capabilities, since this component may be partially produced by antiprotons.

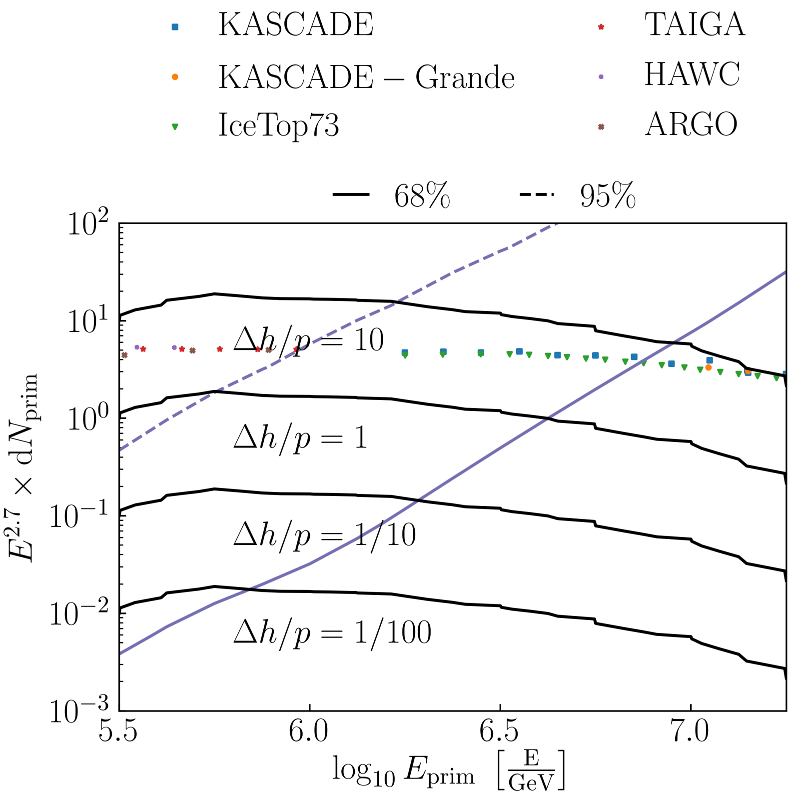

Figure 7.5: Predicted sensitivities of IceCube to the h/p ratio. The purple dashed and solid lines show the 68% and 95% confidence limits. The solid black lines visualize the different ratio levels between h and p. We have included experimental measurements of the primary nucleon flux by IceTop73 [129], KASCADE [130], KASCADE-Grande [6], ARGO [7], TAIGA [8] and HAWC [10].

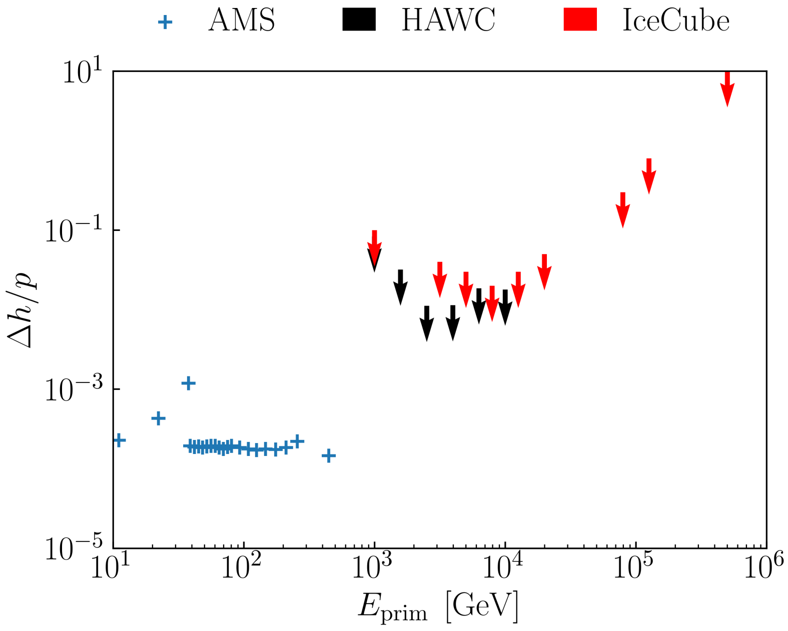

Figure 7.6: Predicted sensitivities of IceCube to the h/p ratio compared to constraints set by HAWC and measurements by AMS on the antiproton to proton ratio. While IceCube is cabale of setting constraints at higher energies and can reach similar constraints as HAWC at lower energies, these limits are on an additional nucleon flux, requiring an injection model for direct comparisons.

7.5 Conclusion

The results shown in Figure 7.5 shows the ability neutrino telescopes have to constrain the antiproton ratio at high energies. They offer an additional channel to cosmic ray experiments, to define the primary cosmic ray flux. Reaching and setting limits on the very energetic cosmic ray composition is of interest to decaying dark matter models, as shown in Section 7.1. Similar to the Stau analysis, the sensitivity of these types of searches will only increase with time (data). In addition, with new neutrino telescopes coming online [12, 13, 14] in the next few years, as well as the upgrades to existing ones [121], the sensitivities will be even further improved. This shows the versatility of neutrino detectors and the new and additional uses that can be drawn from them.

Currently we are working to further improving this study, by generalizing the injection, making it model independent, while also improving the interpretation of the results.

With new upcoming ocean based detectors these types of studies will become even more powerful due to the increase in exposure time. The ocean, unlike ice comes with its own problems, namely a new background component, bioluminescence. In the next chapter we will discuss how we can treat this new background component and even bridge the gap between the physics community and biologists.

Bioluminescence 8

8.1 Bioluminescence Triggers . 69
8.2 Population Modeling 70
8.3 Current Modeling 70
Discretization 72
8.4 Light Propagation 75
8.5 Fourth Day 75
8.6 Discussion 77
8.7 Simulation vs Data 81
8.8 Conclusion 82

Multiple of the new upcoming neutrino telescopes are based in the ocean, such as P-ONE [12] and KM3NeT [13]. Unlike IceCube-Gen2 [121] and its predecessor, Cherenkov telescopes in the ocean have to contend with an additional source of light, bioluminescence. Bioluminescence is optical light produced chemically by organisms in form of either flashes or a steady glow. The spectral distributions of these pulses peak in the range 450 nm to 490 nm [131, 132], which is near to the peak of the expected Cherenkov spectrum at 420 nm [133, 134]. This makes disentangling the two sources difficult. Studies from ANTARES [15] and KM3NeT show that neutrino telescopes are capable of measuring bioluminescence [135, 136]. While estimations of bioluminescence in neutrino telescopes have been done previously [137, 138], these were using approximations and mainly focused on emission due to encounters. Their rate was found to be $\approx 1\ \mathrm{h}^{-1}$. Here we model emissions due to encounters and shear stress [139]. The latter of which has a rate of ≈ 3 magnitudes larger, see figure 8.11. This makes precise water flow modeling around the detector a requirement. Previous studies were limited to specific cases of bioluminescence such as dolphin-stimulated [140] and nozzle throats [141]. Here, we construct a realistic bioluminescence model based on a water current simulation and a Monte Carlo model for the organisms. This framework can be applied to any desired geometry. The framework for the model is called *Fourth Day*[*] and is publicly available.

8.1 Bioluminescence Triggers

Two external sources causing organisms to flash are given by contact and shear forces. The first of which is a response to the organism colliding with another object. The second source, shear stress, is a defensive response to an applied shear force, such as water turbulence [138, 142, 143, 144, 145, 146]. This response has been observed in background currents as low as 5 mm/s [147], far lower than the cm/s velocities seen in deep ocean experiments. The emission probability due to shear stress follows a binomial distribution, with a successful emission probability denoted by P_{shear}. The emission probability is linearly related to the water current's gradient [148, 140, 149, 150]

$$P_{\mathrm{shear}} \propto \alpha \nabla \mathbf{u}. \tag{8.1}$$

Here $\mathbf{u}$ describes the flow velocity and α is a proportionality factor. For simplicity we assume α is a species dependent constant. These shear emissions make precise water current modeling a necessity, which we describe in Section (8.3). Another source of flashes are spontaneous emissions. These are rare, due to the high energy cost for the organisms [151] and for this reason we neglect it. Once an organism flashes, be it due

---

[*] `https://github.com/MeighenBergerS/fourth_day`

to an encounter or shear force, it will produce approximately $10^9 - 10^{13}$ photons [137]. These photons are then attenuated while traveling to the detector, as described in Section (8.4).

8.2 Population Modeling

The organisms are modeled using a Monte Carlo scheme. Each individual one is assigned a position and species. According to the species, the following set of properties is defined as probability distribution functions (pdf): Spectral emission, photon count, duration of emission, depth and movement. Figure 8.12 shows an example of time series pdfs used in a simulation. There two distinct time series are used for two different species of organisms. These distributions are then sampled. Both the density of organisms and the probability coefficient α in Equation (8.1) are treated as unknowns. For sites such as ANTARES the density of organisms is $\approx 0.02\ \mathrm{m}^{-3}$ [137], which can be used as a rough estimate. At each time-step the velocity and position of the organisms are updated according to the external flow velocity field together with their own sampled velocity distributions. Organisms that encounter an object – such as a detector – are assumed to emit light. If a given organism is not flashing due to an encounter, the binomial distribution with the emission probability from equation (8.1) is sampled. On a successful flash, the duration of the flash is again sampled from another species-dependent pdf. We assign a maximum emission energy to each organism, which is reduced when an emission occurs. This limits the total number of pulses they can emit at once.

8.3 Current Modeling

A typical shape of submerged neutrino detection unit is given by a spherical or vertically arranged cylindrical body with a round top and bottom. In order to model the flow past such detectors numerically, we consider for simplicity a two-dimensional horizontal cross-section of the problem. This way, we aim to obtain a realistic approximation to the flow at least past the detector's cylindrical middle part, noting that for the spherical top and bottom parts a full three-dimensional setup would be required. The model described in this section can in principle be extended readily to the three-dimensional case, albeit at the expected substantial increase in computational cost.

The flow is governed by the incompressible Navier-Stokes equations, which are given by a momentum equation and incompressibility condition of the form

$$\partial_t \mathbf{u} + (\mathbf{u} \cdot \nabla)\mathbf{u} + \nabla p/\rho - \nu \Delta \mathbf{u} = 0, \tag{8.2}$$

$$\nabla \cdot \mathbf{u} = 0, \tag{8.3}$$

for flow velocity $\mathbf{u} = (u(\mathbf{x}), v(\mathbf{x}))$ and pressure $p(\mathbf{x})$, where $\mathbf{x} = (x, y)$ denotes the space coordinate. ∂_t denotes the partial derivative with respect to time t, $\nabla = (\partial_x, \partial_y)$ the gradient, and further $\Delta = \partial_{xx} + \partial_{yy}$ denotes the diffusion operator. Finally, $\nu = \mu/\rho$ is given by the kinematic viscosity, for viscosity μ and density ρ. In the following, we will set $\mu = 0.001306$ Ns/m^2 and $\rho = 999.7$ kg/m^3, which corresponds to water at 10 degrees Celsius. Note that in terms of the flow's qualitative behaviour past the cylinder, we expect similar results for the typical temperature range of sea water[†].

We consider a rectangular domain Ω of length $L_x = 26$ m and width $L_y = 10$ m. The domain further includes a circular gap corresponding to the detector, which is placed at $\mathbf{x} = (2, 5)$ m and has a radius of 15 cm. To complete the model's description, we further require boundary and initial conditions. The former conditions are given by normal flow conditions of the form

$$\mathbf{u} = (u_{in}, 0), \ x = 0, \ y \in \left[0, L_y\right] \tag{8.4}$$

$$\mathbf{u} = (0, 0), \ \text{Detection Unit Boundary} \tag{8.5}$$

$$p = 0, \ x = L_x \tag{8.6}$$

for $u_{in} = 0.1$ m/s. Note that we will find these restrictions to be sufficient for our purposes of simulating the flow, and in particular no boundary condition is set e.g. for $\mathbf{u}$ at the outflow boundary. Finally, we consider initial conditions of the form

$$\mathbf{u}(\mathbf{x}, 0) = \mathbf{0}, \quad p(\mathbf{x}, 0) = 0, \tag{8.7}$$

noting that the velocity and pressure fields will adjust to the boundary conditions after the first time step in the numerical model.

The problem of flow past a circle has been studied extensively in literature (e.g. [152, 153, 154, 155, 156]), and its complexity depends on the inflow speed u_{in}, kinematic viscosity ν, and circle diameter d. These three parameters can be combined to the non-dimensional Reynolds number

$$Re = \frac{u_{in} d}{\nu}, \tag{8.8}$$

which can then be used to determine the type of flow [153]. In our case,

$$Re \approx 23,000, \tag{8.9}$$

and we expect to obtain a boundary layer – i.e. a thin layer in which the velocity decreases rapidly to the prescribed zero value at the boundary – around the circle, which is separated from the circle towards the circle's wake (see Figure 8.1). The layer's thickness is proportional to $\sqrt{\nu}$ [157], and for the above Reynold's number, the layer is laminar (i.e. non-turbulent). Pairs of trailing vortices are created and shed periodically between the separated boundary layer filaments near the circle's wake. The vortex shedding in turn creates a so-called Kármán vortex street of pairs of vortices in the circle's wake [156]. The periodicity of this process is represented by the non-dimensional Strouhal number $St = fd/u_{in}$, where f denotes the frequency at which vortex pairs are shed. St can be formulated as a function of Re, and for $Re \approx 23,000$, we expect $St \approx 0.2$ [153]. Finally, we note that for Reynold's numbers between 300

[†] In terms of the Reynolds number as described below, we have $Re \approx 16,000$ for 0°C, and $Re \approx 30,000$ for 20°C, which leads to the same turbulent regime as for the Reynolds number $Re \approx 23,000$ corresponding to 10°C.

and $30,000$, the vortex street is turbulent, in the sense that the vortex pairs interact strongly with each other and degrade the periodic pattern along the flow in the circle's wake (see Figures 8.1, 8.4).

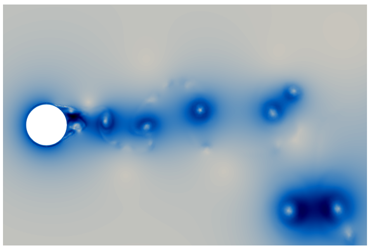

Figure 8.1: Magnitude of velocity field after 200 seconds, zoomed to circle. The boundary layer is separated from the circle, generating vortices which are shed in pairs and form a vortex street. Colour scheme: 0m/s (grey) to 0.25m/s (dark blue; see Figure 8.4). Taken from [139].

Discretization

We discretize the model in space using the finite element method. This way, we can readily use irregular meshes, which facilitate the domain's discretization near the circular gap corresponding to the detector, and which further allows for a varying resolution in the domain. In particular, for a higher efficiency in terms of computational cost, we employ a relatively fine resolution (1 cm) near the vortex shedding area, a slowly decreasing resolution along the circle's wake (2.5 cm, 5 cm, and 10 cm), and a coarse resolution (1 m) away from the circle and wake (see Figures 8.2, 8.3).

We consider Taylor-Hood finite elements for the velocity and density field [158], and further apply an Incremental Pressure Correction Scheme (IPCS, [159]) for the time discretization. Note that the above choice of resolutions in the domain's various regions leads to under-resolved areas; in particular, this includes the boundary layer at the circle, as well as vortices further along the wake. To avoid the corresponding instabilities [160], we also include a Streamline Upwind Petrov Galerkin (SUPG, [161]) method in the discretized velocity equation.

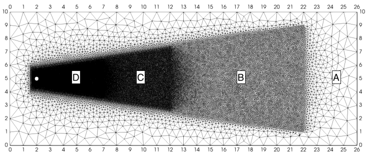

Figure 8.2: Mesh used for flow simulation. Regions A, B, C, and D correspond to a resolution of 1 m, 10 cm, 5 cm, and 2.5 cm, respectively. Near the circle, another refined region corresponds to a resolution of 1 cm (see Figure 8.3). x and y axes are given in meters. Taken from [139].

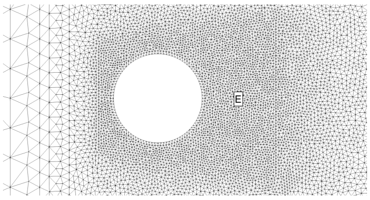

Figure 8.3: Mesh used for flow simulation, zoomed to region near gap corresponding to detector. Regions E corresponds to a resolution of 1 cm. Taken from [139].

The velocity space $\mathbb{V}_u$ is given by the space of vector-valued continuous piece-wise quadratic polynomials, and the pressure space $\mathbb{V}_p$ consists of scalar continuous piece-wise linear polynomials. Both of these spaces are further assumed to be restricted to functions that satisfy the boundary conditions (8.4) - (8.6). The momentum equation (8.2) is space-discretized according to

$$\begin{aligned}\langle \mathbf{w}, \partial_t \mathbf{u} \rangle + \langle \mathbf{w}, (\mathbf{u} \cdot \nabla)\mathbf{u} \rangle & \\ + P(\mathbf{u}, p; \mathbf{w}) & \qquad \qquad (8.10) \\ + \langle \tau(\mathbf{u} \cdot \nabla)\mathbf{w}, u_{res} \rangle = 0 & \qquad \forall \mathbf{w} \in \mathring{\mathbb{V}}_u,\end{aligned}$$

where $\langle ., . \rangle$ denotes the L^2-inner product, and $\mathring{\mathbb{V}}_u$ denotes the velocity space including boundary conditions. The term in the second line of (8.10) corresponds to the discrete Cauchy stress tensor

$$\sigma(\mathbf{u}, p) = 2\nu\epsilon(\mathbf{u}) - pI, \tag{8.11}$$

for symmetric gradient $\epsilon(\mathbf{v}) = (\nabla\mathbf{v} + \nabla\mathbf{v}^T)/2$ and 2×2 identity matrix I, and is given by

$$P(\mathbf{u}, p; \mathbf{w}) = \langle \sigma(\mathbf{u}, p), \epsilon(\mathbf{w}) \rangle. \tag{8.12}$$

Finally, the term in the third line of (8.10) corresponds to the SUPG stabilization, and the discretized momentum equation's residual appearing in it is given by

$$u_{res} = \partial_t \mathbf{u} + (\mathbf{u} \cdot \nabla)\mathbf{u} - \nabla \cdot \sigma(\mathbf{u}, p). \tag{8.13}$$

Further, the stabilisation parameter is set to

$$\tau = \frac{1}{2}\left(\left(\frac{2\kappa(x)}{\Delta t}\right)^2 + \left(\frac{2|\mathbf{u}|}{\Delta x}\right)^2 + 9\left(\frac{4\nu}{\Delta x^2}\right)^2\right)^{-\frac{1}{2}}, \tag{8.14}$$

where $\kappa(x) = 1$ for $x < 2.75$ m, and $\kappa(x) = 1/6$ otherwise. Δt and Δx denote the time step and (local) mesh size, respectively. This choice of τ is similar to one often considered in the literature (e.g. [162]), up to the additional parameter κ. In the model used in this section two sources of instabilities appeared frequently: first, towards the later stages of the wake, where the resolution is relatively coarser, vortices may become unstable. Second, the separated boundary layer filaments may become unstable. We found that different values of $\kappa(x)$ were suited best for these two types of instability, thus motivating the split used in τ as given above.

Next to the momentum equation, the incompressibility condition (8.3) is used to derive an equation for the pressure field. The latter equation then appears in the time-discretized scheme, where the momentum equation is first solved for to obtain a predicted velocity $\mathbf{u}^p$. Given the nonlinear advection term $(\mathbf{u} \cdot \nabla)\mathbf{u}$, this is done in an iterative manner according to

do $k = 1, ..., m$:

$$\begin{aligned}&\langle \mathbf{w}, (\mathbf{u}^{p,i+1} - \mathbf{u}^n)/\Delta t \rangle + \langle \mathbf{w}, (\bar{\mathbf{u}}^* \cdot \nabla)\bar{\mathbf{u}}^{p,i+1} \rangle \\ &\quad + P(\bar{\mathbf{u}}^{p,i+1}, p^n; \mathbf{w}) \qquad \qquad \qquad \qquad (8.15) \\ &\quad + \langle \tau(\mathbf{u}^n)(\bar{\mathbf{u}}^* \cdot \nabla)\mathbf{w}, \bar{u}_{res}) \rangle = 0 \qquad \forall \mathbf{w} \in \mathring{\mathbb{V}}_u,\end{aligned}$$

where $(\mathbf{u}^n, p^n)$ are the known fields of the current time step (starting from the initial conditions $(\mathbf{u}^0, p^0)$). Further, the mid-point averages $\bar{\mathbf{u}}^{p,i+1}$ and $\bar{\mathbf{u}}^*$ are given by

$$\bar{\mathbf{u}}^{p,i+1} = (\mathbf{u}^n + \mathbf{u}^{p,i+1})/2, \tag{8.16}$$

$$\bar{\mathbf{u}}^* = (\mathbf{u}^n + \mathbf{u}^{p,i})/2, \tag{8.17}$$

for unknown $\mathbf{u}^{p,i+1}$ to be solved for, and the current iteration's known guess $\mathbf{u}^{p,i}$. Note that in the first iteration, the latter guess is set to $\mathbf{u}^n$, while in each following one it is set to the velocity field computed in the previous iteration. Finally, we note that the residual in the SUPG term is time-discretized according to

$$\begin{aligned} \bar{u}_{res} =& (\mathbf{u}^{p,i+1} - \mathbf{u}^n)/\Delta t + (\bar{\mathbf{u}}^* \cdot \nabla)\bar{\mathbf{u}}^{p,i+1} \\ & - \nabla \cdot \sigma(\bar{\mathbf{u}}^{p,i+1}, p^n). \end{aligned} \tag{8.18}$$

Once the final predicted velocity $\mathbf{u}^p$ has been computed in the loop's last iteration, the pressure corresponding to the next time level $n+1$ is obtained by solving an update equation of the form

$$\Delta t \langle \nabla(p^{n+1} - p^n), \nabla q \rangle = -\langle \nabla \cdot \mathbf{u}^p, q \rangle, \tag{8.19}$$

for any test function $q \in \mathring{\mathbb{V}}_p$, where $\mathring{\mathbb{V}}_p$ is defined analogously to $\mathring{\mathbb{V}}_u$. Finally, given $(\mathbf{u}^p, p^{n+1})$, we compute a velocity field $\mathbf{u}^{n+1}$ according to

$$\langle \mathbf{u}^{n+1} - \mathbf{u}^p, \mathbf{w} \rangle = -\Delta t \langle \nabla(p^{n+1} - p^n), \mathbf{w} \rangle, \tag{8.20}$$

for any test function $\mathbf{w} \in \mathring{\mathbb{V}}_u$.

The simulation is run up to $t = 1200$ s, with a time step given by $\Delta t = 0.01$ s. The mesh is implemented using Gmsh [163], and the finite element discretization is based on the automated finite element toolkit Firedrake[‡] [166]. The latter uses the solver library PETSc (see e.g. [167, 168]) to compute the resulting systems of equations. A snapshot of the simulation at 200 seconds is given in figure 8.4, depicting the turbulent vortex street's degraded periodic pattern. We find that the Strouhal number is higher than anticipated, noting that for such turbulent flows many aspects of the numerical scheme impact the latter number. This includes subtle factors such as the distance of the side walls to the cylinder [169], and the precise mesh setup near the cylinder.

Finally, given the simulation, the velocity field as well as the magnitude of its gradient, i.e. $|\nabla \mathbf{u}(\mathbf{x}, t)|$, are saved after each simulated second Δt_s and passed on to the population simulation as described in Section (8.2). While ideally, the velocity field information would be passed on after each time step Δt, here we instead chose Δt_s to avoid large data storage requirements.

[‡] for further details, see [164, 165] or `http://firedrakeproject.org`

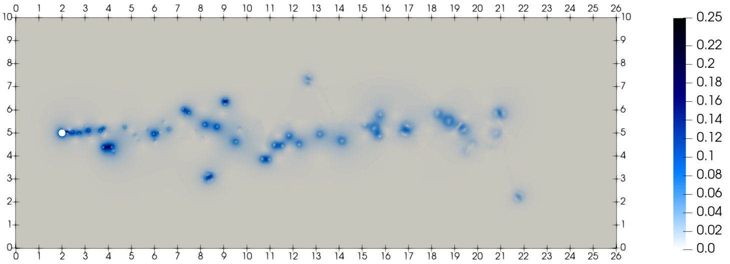

Figure 8.4: Velocity field magnitude after 200 seconds; scale in m/s. At $Re \approx 23,000$, the vortex street is turbulent, leading to a degraded periodic pattern. Axes labels are given in meters. Taken from [139].

8.4 Light Propagation

Once the population simulation has finished, the light from each organism's flashes are propagated to the detector. We attenuate the photon count using an attenuation factor, A, given by

$$A = \frac{\exp\left(-r \times l\right)}{4\pi r^2}. \tag{8.21}$$

Here r references the distance between the organisms, at the time of its emission, to the detector. For the wavelength dependent factor, l, we use values from [170]. For a distance of 10 meters the total photon count drops by approximately a factor of 1000. Given this exponential attenuation, flashes beyond 30 m distance are usually irrelevant for a detector.

8.5 Fourth Day

The Python package Fourth Day is designed in a modular fashion. An overview of the different modules is given in figure 8.5.

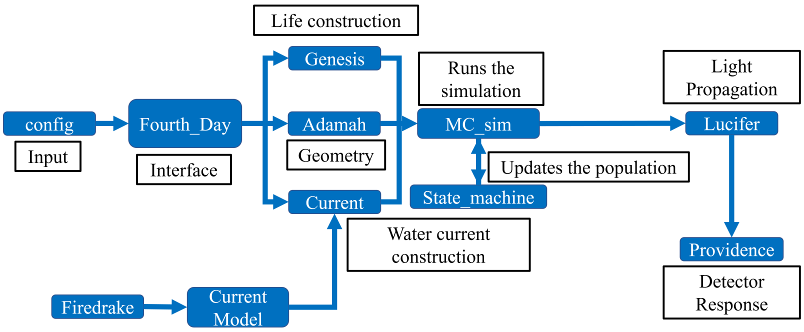

Figure 8.5: A scetch of Fourth Day's structure. We use Firedrake to model the water current. Any other code is also viable, as long as the output is given as a matrix defining the current at every spatial grid point.

The simulation parameters are defined in *config.py* and passed to the main interface *Fourth_Day*. This then distributes them to the three modules *Genesis*, *Adamah* and *Current*. In *Genesis* the organisms are created by assigning their individual properties, such as size, emission pdf, movement pdf and energy. *Adamah* constructs the simulation geometry, constructing the meshes for the detector and simulation area. These are used as boundaries for the simulation either stopping the modeling of the organisms when they exit the simulation area or disallow the propagation into the detector itself. Current translates the input water current grids. These should represent the water state on a discretized grid, providing the water velocity in every cardinal direction at each point. While Fourth Day currently models purely 2D states, by using 3D arrays at this step, the simulation code can be easily extended to three dimensions. After the organisms, geometry and water current are constructed, these are passed to *MC_sim*. This module constructs the starting population, by randomly sampling the space with organisms. This population state is then passed at every step to *State_machine* which updates the state by the desired time step. A state update is the computationally most expensive step, due to the need of propagating every single organism, sampling whether the organisms emit light and updating their energy. Collisions are also modeled here, but for low densities we recommend switching them off (an option in the config file). Doing this improves computational time drastically. After the simulation has finished, the states at each time step are collected and passed to *Lucifer*. An example state is shown in figure 8.6. In *Lucifer* the light is attenuated according to equation 8.21. The resulting photon counts are then folded with the detector response in *Providence*.

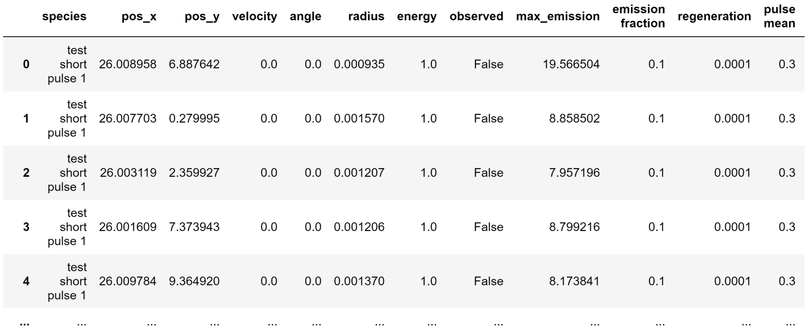

	species	pos_x	pos_y	velocity	angle	radius	energy	observed	max_emission	emission fraction	regeneration	pulse mean
0	test short pulse 1	26.008958	6.887642	0.0	0.0	0.000935	1.0	False	19.566504	0.1	0.0001	0.3
1	test short pulse 1	26.007703	0.279995	0.0	0.0	0.001570	1.0	False	8.858502	0.1	0.0001	0.3
2	test short pulse 1	26.003119	2.359927	0.0	0.0	0.001207	1.0	False	7.957196	0.1	0.0001	0.3
3	test short pulse 1	26.001609	7.373943	0.0	0.0	0.001206	1.0	False	8.799216	0.1	0.0001	0.3
4	test short pulse 1	26.009784	9.364920	0.0	0.0	0.001370	1.0	False	8.173841	0.1	0.0001	0.3
...	...	...	...	...	...	...	...	...	...	...	...	...

Figure 8.6: An example state of a simulation run. Here, we used custom organisms called "test short pulse 1" to cross check the resulting emission spectra.

The modular structure of Fourth Day allows for a large amount of customization by the user but also comes with a lot of presets, to make it more accessible. An example simulation run could look as follows

```python
# Module imports
from fourth_day import Fourth_Day, config

# Some scenario settings
config['scenario']['population size'] = 100 # Starting population
config['scenario']['duration'] = 600 # Simulation duration in seconds
config['scenario']['injection']['rate'] = 1 # Number of organism to inject per second
config['scenario']['detector'] = {
    "type": "Custom"
}
# Organisms
config['organisms']['emission fraction'] = 0.1 # Amount of energy used per flash
config['organisms']['alpha'] = 2.  # Proportionality factor for the probability
config['organisms']['photon yield'] = 1e10  # Number of photons emitted
```

```
config["organisms"]["filter"] = ’depth’  # Organism filter
config["organisms"]["depth filter"] = 1000  # Only organisms below 1000 m
# Some detector properties
config["geometry"]["detector properties"]["Custom"] = {
    "x_pos": 2.,
    "y_pos": 5.,
    "det num": 1,
    "x_offsets": np.array(
        [0.]
    ),
    "y_offsets": np.array(
        [0.]
    ),
    "angle offset": 0.,  # In which direction the detector points
    "opening angle": 360.,  # The opening angle
    "wavelength acceptance": [ # lower and upper wavelengths, the quantum efficiency
        [325., 600.,1.],
    ],
}
# Creating a fourth_day object
fd = Fourth_Day()
# Launching the simulation
fd.sim()
```

Above we created a simulation run, where the starting population is composed of 100 organisms. The simulation duration was set to 10 minutes and 1 additional organism is injected per second. Afterwards we set the detector to be of custom specifications. These will be set later. Following this, some organism properties are defined. First the amount of energy the organisms use per flash. 0.1 means they can flash 10 times before they run out of energy. One can also define the amount of energy organisms regenerate per second, standard is 0.1%. The emission proportionality factor from equation 8.1 was set to 2. A lower value would reduce the amount of flashes produced in the simulation run. The amount of photons per flash was set to a flat 1e10. A more involved simulation would assign a species dependent number. The organisms are now chosen by the depth where they can be found, in this case only organisms which can be found below 1000 m are allowed. Finally the customized detector is set up. First its position, number of detectors inside, offset from the central mass of these detectors and their angular offset are defined. Then the opening angle of the detector(s) are set to 360 degrees. As a last step the wavelength acceptance is defined to be $\lambda \in [235\ \text{nm},\ 600\ \text{nm}]$ with a quantum efficiency of 100%. This means we are modeling a perfect detector with a 360° field of view in this run.

8.6 Discussion

Running a simulation for a perfect detector with a 360° field of view (FoV), we can confirm the expectations and estimates from [137, 138], that most of the light is generated downstream of the module. As shown in figure 8.1, downstream the flow will be most turbulent. Together with Equation 8.1, the organisms will be flashing predominantly after drifting into the module’s wake. Figure 8.7 emphasizes this point. In the top plot the range of the gradient was chosen to emphasize the vortices, while in the bottom plot to visualize the area where flashes due to shear stress are possible.

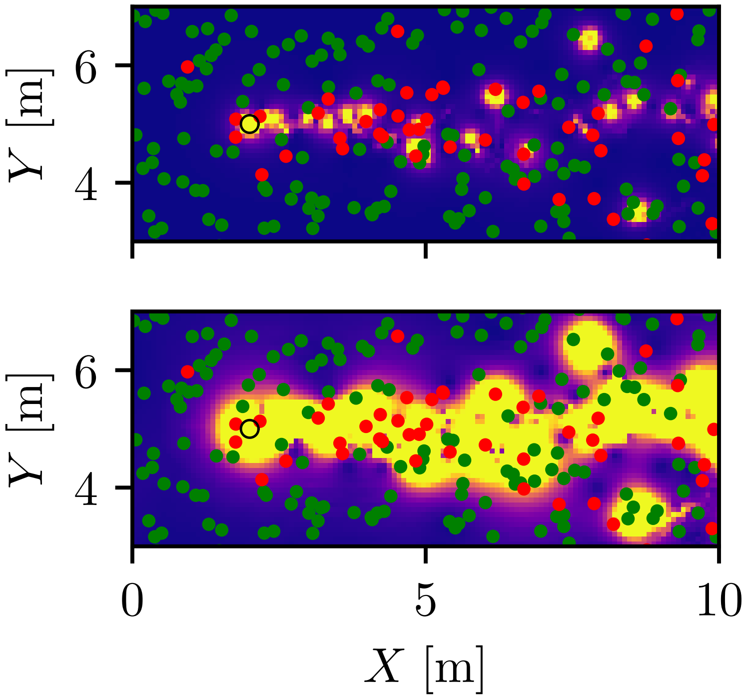

Figure 8.7: Distribution of organisms emitting light (red) and those that are not (green). The background shows the gradient of the velocity field. Clearly visible is the increase in emitting organisms in the detector's (black ring) wake. The top plot uses a larger range of gradients to visualize the vortices. The bottom one limits the range, emphasizing the regions where flashes due to shear stress are possible. Taken from [139].

A new effect, only visible due to the combined simulation method, is the maxima shift for different wavelengths in time, shown in figure 8.8, when multiple photo multiplier tubes (PMTs) with differing FoVs are used, such as those of KM3NeT, P-ONE and STRAW-b. These shifts are due to organisms drifting from one detector's FoV into another's. Should the duration of emission last longer than its time inside of the area of visibility of a single detector, the position of the maximum will be shifted. This in turn results in a single organism's pulse to appear as multiple when integrating over the wavelengths.

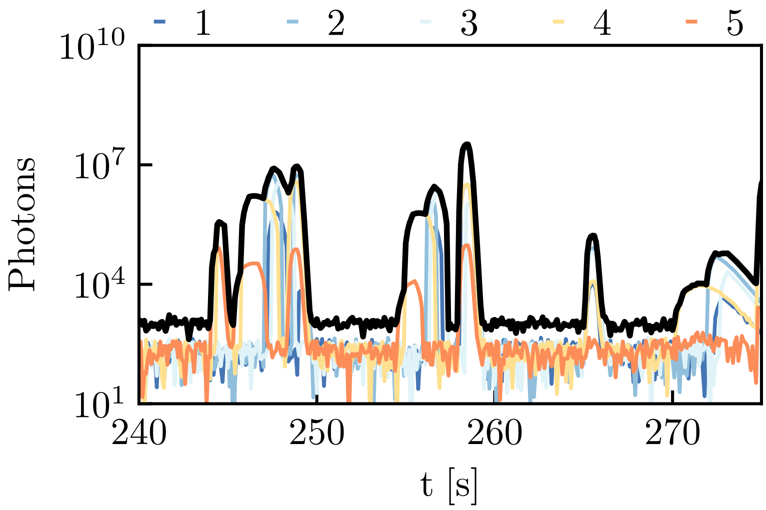

Figure 8.8: Example output for a spectrometer simulation with a 10 cm/s water current. Here we model five different PMTs measuring different wavelengths. In sequential order the wavelength ranges are [500 nm, 515 nm], [485 nm, 500 nm], [475 nm, 485 nm], [465 nm, 475 nm] and [455 nm, 465 nm]. The black line indicates the total photon count. Due to the finite opening angles of the detectors, here assumed to be 25°, and the current velocity, single emission flashes show varying maxima positions for different wavelengths. Taken from [139].

Due to these distribution shifts, we create a categorization plot in figure 8.9, where different arriving distributions are shown compared to the original emission pdf. With this we can assign any pulse measured by the detector to a specific species of organism. This type of analysis can be used by neutrino detectors to categorize organisms drifting by, should they posses differing emission pdfs. Applying a Fourier transform to the simulation results in figure 8.10. There we constructed a background model by scrambling the pulses in time. The yellow and green bands show the one and two sigma deviations respectively for the background model. The unscrambled simulation falls within the expectation of the scrambled one. This means the timing of the pulses is random. Due to the chaotic nature of the emission, we can construct realistic simulations by drawing from all possible pulse shapes and randomly distributing them according

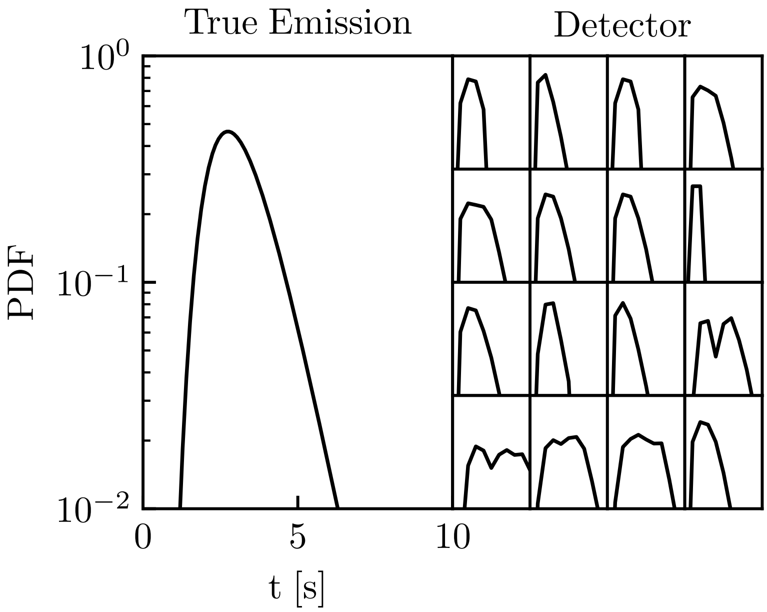

Figure 8.9: Left: emission distribution in time of the modeled organism. Right: emission distributions as seen by a detector pointing orthogonal to the current direction. The axes in the right plots are the same as for the plot on the left. The change in shape is due to the finite FoV and water current velocity. Taken from [139].

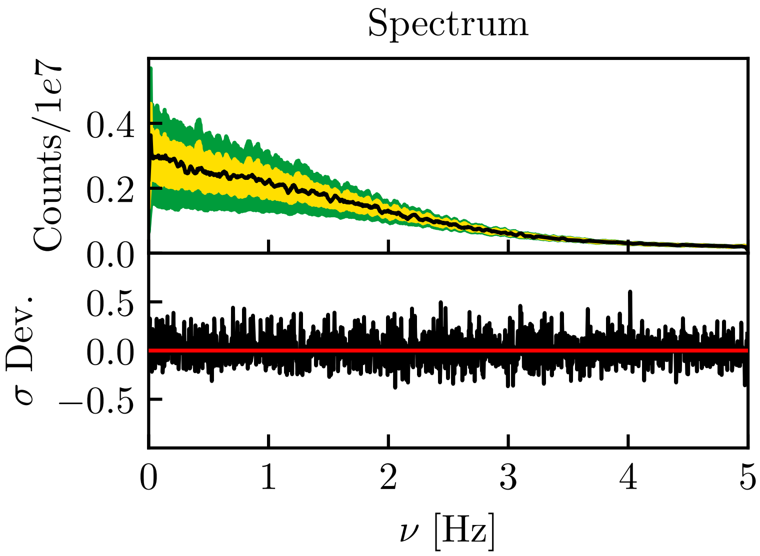

Figure 8.10: Fourier transform of the results from figure 8.8. The top plot shows the spectrum of light reaching the detector. In black is the averaged spectrum from 100 simulation runs. In yellow and green we show the 1σ and 2σ confidence intervals of the background model. The bottom plot shows the deviation of the simulation from the null hypothesis in units of sigma. Taken from [139].

to the expected average, given in figure 8.11. This reduces the calculation time drastically, since the expensive population modeling can be skipped. As discussed in [137] the average number of expected encounter flashes is $\approx 1\,\mathrm{h}^{-1}$, which our simulations confirm. This makes encounter flashes a sub-leading source of bioluminescence when compared to emission due to shear stress. As shown in figure 8.11 a perfect detector with a 360° field of view will measure $\approx$ 1000 flashes per hour in a 10 cm/s water flow. Additionally, shear emissions can not be modeled with a linear density dependence as encounters [137] and natural bioluminescence [171], as shown in figure 8.11.

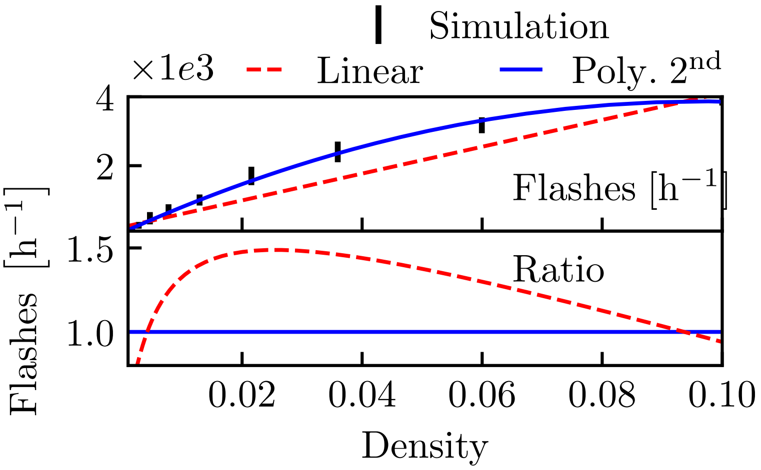

Figure 8.11: The average number of bioluminescence flashes measured by a detector shown in black. The red dashed line shows a linear fit while the blue solid line shows a polynomial fit of second order. The bottom plot shows the ratio between the fits. The x-axis is given in units of organisms / m^3. Taken from [139].

8.7 Simulation vs Data

A crucial step in verifying the simulation results, is a comparison with experimental data. For this reason we show here a comparison between the simulation and very preliminary data from the recently deployed STRAW-b's PMT Spectrometer. Specifically we only compare the unfiltered channel which measures wavelengths between $\lambda \in [325\text{ nm}, 600\text{ nm}]$ using a 1 inch PMT.
For the simulation we use two distinct artificial organisms, each with a Gaussian emission spectrum with $\mu = 490$ nm and $\sigma = 80$ nm. They differ in their emission profiles shown in figure 8.12. There both organisms use a gamma distribution with a mean of two seconds. They differ in the standard deviation, with the narrow pulse using 0.3 seconds and the long pulse 1.5 seconds.

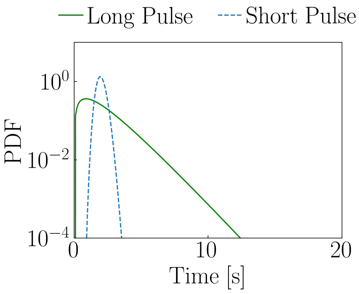

Figure 8.12: The emission profile of the two organisms used to model the STRAW-b measurements. One uses a narrow profile while the other a wider one. Both are gamma distributions with a mean of 2 seconds.

For the water current we assume a flow of 5 cm/s and we set the density of the organisms to 10^{-2} / m^3. Each pulse contains 10^{10} photons which we then propagate to the detector. As mentioned before, the diameter of the PMT is 1 inch with a quantum efficiency of approximately 25%. The resulting time series including preliminary data is shown in 8.13. There we show the closest approximation of the real data found in 100 hours of simulation. Due to the random nature of the emissions, as discussed before, the position of the peaks is completely random, while the shapes are defined by the geometry of the system and the detector. This comparison should give an idea, that the simulation is already capable of producing realistic results, which in turn can now be used to analyze bioluminescence data from the deep sea.

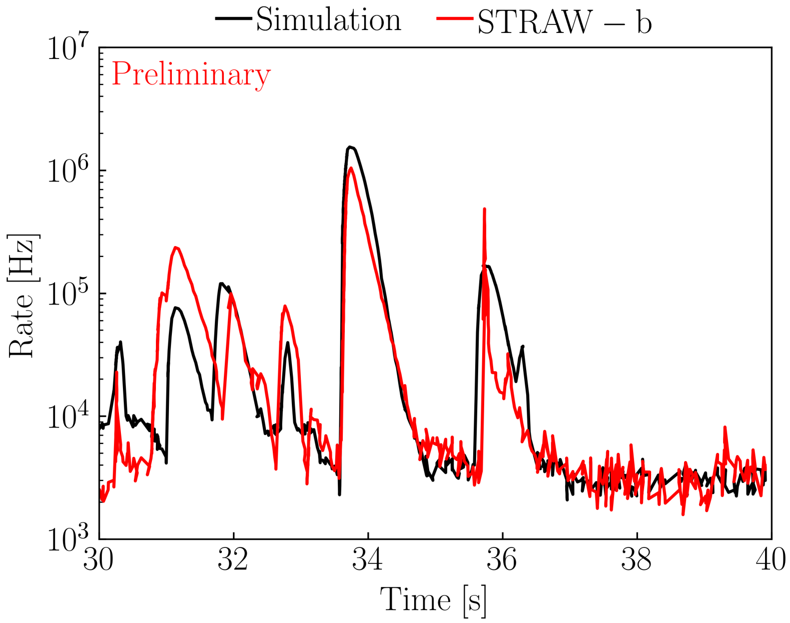

Figure 8.13: A comparison between the measured time series by STRAW-b using preliminary data and the simulation prediction. Here we show the best approximation from the simulation from 100 hours of simulated data.

8.8 Conclusion

Predicting deep sea bioluminescence requires precise simulations of the water flow around detectors. Unlike encounter flashes, which are negligible at large depths, emissions due to shear stress are not. We predict approximately 3 orders of magnitude higher rates for shear flashes than encounter emissions. Additionally, the rate shows a more complicated relationship to organism density than the linear dependence of encounter flashes and background glow, as seen in figure 8.11. For realistic detector modules, such as those employed by KM3NeT, P-ONE and STRAW-b, we have identified unique bioluminescence signatures, defined by the flow velocity and the FoVs of the PMTs. These can in turn be used to identify the organisms drifting past these detectors, making deep sea detectors interesting for biologists as well. Finally, by showing that the emissions are chaotic, we have constructed a model which is capable of producing large amounts of simulated data, based on a small subset of precise simulations.

Conclusion 9

In this thesis, we have covered a wide range of topics, from the modeling of atmospheric particle cascades to the study of new physics and even bridged the gap to biology.

Traditionally, we can use particle cascades to measure Standard Model cross sections and other observables, such as the kaon to pion ratio. We have shown, how exact modeling of the atmosphere and the effect on particle production and propagation is essential in such studies. Based on this we have measured the kaon to pion ratio using the BOREXINO detector. While such measurements are limited by detector specifications and statistics, theoretical uncertainties are also a source of variability. With ever improving detectors, theories need to become more precise as well, to push experiments to new frontiers.

To this end we have increased the precision of electromagnetic shower modeling by constructing a new interaction model based on new cross section calculations. We offer this model as part of a new simulation framework called EmCa, which also includes more traditional interaction models. This framework utilizes cascade equations to solve for the average flux of particles, achieving a similar precision as Monte Carlo simulations in a fraction of the time. Using this framework we were able to test and benchmark the new model, introducing material effects removing traditionally problematic modeling aspects, such as the infrared divergence of Bremsstrahlung. We were able to show that differences between cascade equation simulations and Monte Carlo ones were not based on 3D effects but instead on the precision of the used integrators. Using this new electromagnetic framework we modeled the difference in deposited energy when using the fluorescence technique, different electromagnetic models can cause. Using Bethe-Heitler models causes an overestimation of up to 5% of the shower's total energy. This makes the need to include uncertainties caused by electromagnetic models important, something which is usually neglected.

Using these exact modeling techniques, we then treated the atmosphere as a large collider experiment. Due to the far higher energies available in cosmic rays, when compared to collider experiments, we expect new physics could be found in atmospheric particle cascades. We introduce a new search technique for neutrino detectors, by looking for new physics signals towards the horizon. This requires precise modeling of the energy loss and production of particles in the atmosphere. Heavy charged particles, which couple weakly to the Standard Model, will lose most of their energy through ionization. This, unlike muons, makes them able to pass through the large amount of material surrounding IceCube or ocean based neutrino detectors, making this a clean channel for measuring new physics. The only background is provided by neutrinos, which produce muons near the detector. By setting hard energy and angular cuts we were able to set the most stringent non-collider based limit on the stau's mass, the supersymmetric partner to the tau. Extrapolating to larger livetimes we then showed that IceCube is more than capable of competing with collider experiments in setting limits on staus.

Next, we used the same modeling approach to simulate the production of neutrinos in the atmosphere by a new antiproton component. Some beyond the Standard Model theories predict such a new flux, for example from decaying dark matter. Using these predictions we study IceCube's sensitivity to this component and compare these to limits set by HAWC. We predict that IceCube is capable of setting similar constraints and can reach far higher energies. An added effect of this component is that the astrophysical flux measured by IceCube could, in part, be explained by antiprotons.

Finally, we moved away from particle cascades and to a new background component for oceanic neutrino detectors, bioluminescence. By utilizing precise flow models, we constructed a framework to model the light emissions of organisms drifting by deep ocean detectors. From this we predict unique signatures and show that encounter emissions are neglible compared to those caused by shear stress.

Together we introduced two new frameworks to increase the precision of existing background and signal models, while showing the power of these approaches in three different analysis.

Bibliography

[1] T. Antoni *et al.*, “Kascade measurements of energy spectra for elemental groups of cosmic rays: Results and open problems,” *Astroparticle Physics*, vol. 24, no. 1, pp. 1 – 25, 2005.

[2] M. Glasmacher *et al.*, “The cosmic ray energy spectrum between 1014 and 1016 ev,” *Astroparticle Physics*, vol. 10, no. 4, pp. 291 – 302, 1999.

[3] M. Takeda *et al.*, “Energy determination in the akeno giant air shower array experiment,” *Astroparticle Physics*, vol. 19, no. 4, pp. 447 – 462, 2003.

[4] R. Abbasi *et al.*, “Measurement of the flux of ultra high energy cosmic rays by the stereo technique,” *Astroparticle Physics*, vol. 32, no. 1, pp. 53 – 60, 2009.

[5] A. Aab *et al.*, “Combined fit of spectrum and composition data as measured by the Pierre Auger Observatory,” *JCAP*, vol. 04, p. 038, 2017. [Erratum: JCAP 03, E02 (2018)].

[6] W. D. Apel *et al.*, “The spectrum of high-energy cosmic rays measured with KASCADE-Grande,” *Astropart. Phys.*, vol. 36, pp. 183–194, 2012.

[7] G. Di Sciasco, “Measurement of the Cosmic Ray Energy Spectrum with ARGO-YBJ,” in *Vulcano Workshop 2014: Frontier Objects in Astrophysics and Particle Physics*, 8 2014.

[8] N. Budnev *et al.*, “The TAIGA experiment: From cosmic-ray to gamma-ray astronomy in the Tunka valley,” *Nucl. Instrum. Meth. A*, vol. 845, pp. 330–333, 2017.

[9] H. S. Ahn *et al.*, “Discrepant hardening observed in cosmic-ray elemental spectra,” *Astrophys. J. Lett.*, vol. 714, pp. L89–L93, 2010.

[10] R. Alfaro *et al.*, “All-particle cosmic ray energy spectrum measured by the HAWC experiment from 10 to 500 TeV,” *Phys. Rev. D*, vol. 96, no. 12, p. 122001, 2017.

[11] B. S. Acharya *et al.*, “Introducing the CTA concept,” *Astropart. Phys.*, vol. 43, pp. 3–18, 2013.

[12] M. Agostini *et al.*, “The Pacific Ocean Neutrino Experiment,” *Nature Astron.*, vol. 4, pp. 913–915, 2020.

[13] S. Adrian-Martinez *et al.*, “Letter of intent for KM3NeT 2.0,” *J. Phys.*, vol. G43, no. 8, p. 084001, 2016.

[14] A. D. Avrorin *et al.*, “Baikal-GVD,” *EPJ Web Conf.*, vol. 136, p. 04007, 2017.

[15] E. Aslanides *et al.*, “A deep sea telescope for high-energy neutrinos,” 5 1999.

[16] M. G. Aartsen *et al.*, “The IceCube Neutrino Observatory: Instrumentation and Online Systems,” *JINST*, vol. 12, no. 03, p. P03012, 2017.

[17] G. Alimonti *et al.*, “The Borexino detector at the Laboratori Nazionali del Gran Sasso,” *Nucl. Instrum. Meth. A*, vol. 600, pp. 568–593, 2009.

[18] M. Spurio, *Particles and Astrophysics: A Multi-Messenger Approach*. Astronomy and Astrophysics Library, Springer International Publishing, 2014.

[19] T. K. Gaisser, “Spectrum of cosmic-ray nucleons, kaon production, and the atmospheric muon charge ratio,” *Astropart. Phys.*, vol. 35, pp. 801–806, 2012.

[20] A. M. Hillas, “Cosmic Rays: Recent Progress and some Current Questions,” in *Conference on Cosmology, Galaxy Formation and Astro-Particle Physics on the Pathway to the SKA*, 7 2006.

[21] T. K. Gaisser, *Cosmic rays and particle physics*. Cambridge, UK: Univ. Pr. (1990) 279 p, 1990.

[22] B. Peters, “Primary cosmic radiation and extensive air showers,” *Il Nuovo Cimento (1955-1965)*, vol. 22, pp. 800–819, Nov. 1961.

[23] T. K. Gaisser, T. Stanev, and S. Tilav, “Cosmic Ray Energy Spectrum from Measurements of Air Showers,” *Front. Phys.(Beijing)*, vol. 8, pp. 748–758, 2013.

[24] M. Agostini *et al.*, “Modulations of the cosmic muon signal in ten years of borexino data,” *Journal of Cosmology and Astroparticle Physics*, vol. 2019, pp. 046–046, feb 2019.

[25] NASA, *U.S. Standard Atmosphere, 1976.* Oct 1976, NASA-TM-X-74335.

[26] J. M. Picone, A. E. Hedin, D. P. Drob, and A. C. Aikin, “Nrlmsise-00 empirical model of the atmosphere: Statistical comparisons and scientific issues,” *Journal of Geophysical Research: Space Physics*, vol. 107, no. A12, pp. SIA 15–1–SIA 15–16, 2002.

[27] D. P. Dee *et al.*, “The era-interim reanalysis: configuration and performance of the data assimilation system,” *Quarterly Journal of the Royal Meteorological Society*, vol. 137, no. 656, pp. 553–597, 2011.

[28] F. Riehn, H. P. Dembinski, R. Engel, A. Fedynitch, T. K. Gaisser, and T. Stanev, “The hadronic interaction model SIBYLL 2.3c and Feynman scaling,” *PoS*, vol. ICRC2017, p. 301, 2018. [35,301(2017)].

[29] T. Pierog, I. Karpenko, J. M. Katzy, E. Yatsenko, and K. Werner, “EPOS LHC: Test of collective hadronization with data measured at the CERN Large Hadron Collider,” *Phys. Rev.*, vol. C92, no. 3, p. 034906, 2015.

[30] S. Ostapchenko, “Monte Carlo treatment of hadronic interactions in enhanced Pomeron scheme: I. QGSJET-II model,” *Phys. Rev.*, vol. D83, p. 014018, 2011.

[31] S. Roesler, R. Engel, and J. Ranft, “The Monte Carlo event generator DPMJET-III,” pp. 1033–1038, 2000.

[32] R. Ulrich, “Proton-air and proton-proton cross sections,” *EPJ Web of Conferences*, vol. 52, pp. 07004–, 06 2013.

[33] R. Glauber and G. Matthiae, “High-energy scattering of protons by nuclei,” *Nuclear Physics B*, vol. 21, no. 2, pp. 135 – 157, 1970.

[34] T. Wibig and D. Sobczynska, “Proton - nucleus cross-section at high-energies,” *J. Phys. G*, vol. 24, pp. 2037–2047, 1998.

[35] H. P. Wellisch and D. Axen, “Total reaction cross section calculations in proton-nucleus scattering,” *Phys. Rev. C*, vol. 54, pp. 1329–1332, Sep 1996.

[36] K. A. Olive *et al.*, “Review of Particle Physics,” *Chin. Phys. C*, vol. 38, p. 090001, 2014.

[37] M. Honda, M. Nagano, S. Tonwar, K. Kasahara, T. Hara, N. Hayashida, Y. Matsubara, M. Teshima, and S. Yoshida, “Inelastic cross section for p-air collisions from air shower experiments and total cross section for p-p collisions up to $\sqrt{s}$ =24 tev,” *Phys. Rev. Lett.*, vol. 70, pp. 525–528, Feb 1993.

[38] G. Aielli *et al.*, “Proton-air cross section measurement with the argo-ybj cosmic ray experiment,” *Phys. Rev. D*, vol. 80, p. 092004, Nov 2009.

[39] V. Guzey and M. Strikman, “Proton-nucleus scattering and cross section fluctuations at RHIC and LHC,” *Phys. Lett. B*, vol. 633, pp. 245–252, 2006.

[40] S. Donnachie, H. G. Dosch, O. Nachtmann, and P. Landshoff, *Pomeron physics and QCD*, vol. 19. Cambridge University Press, 12 2004.

[41] J. R. Cudell, K. Kang, and S. K. Kim, “Simple pole fits to p p and anti-p p total cross-sections and real parts,” *Phys. Lett. B*, vol. 395, pp. 311–331, 1997.

[42] A. Donnachie and P. V. Landshoff, “pp and $\bar{p}p$ total cross sections and elastic scattering,” *Phys. Lett. B*, vol. 727, pp. 500–505, 2013. [Erratum: Phys.Lett.B 750, 669–669 (2015)].

[43] M. Guzzi, P. Nadolsky, E. Berger, H.-L. Lai, F. Olness, and C. P. Yuan, “CT10 parton distributions and other developments in the global QCD analysis,” 1 2011.

[44] A. Buckley, J. Ferrando, S. Lloyd, K. Nordström, B. Page, M. Rüfenacht, M. Schönherr, and G. Watt, "LHAPDF6: parton density access in the LHC precision era," *Eur. Phys. J.*, vol. C75, p. 132, 2015.

[45] T. Sjöstrand, S. Ask, J. R. Christiansen, R. Corke, N. Desai, P. Ilten, S. Mrenna, S. Prestel, C. O. Rasmussen, and P. Z. Skands, "An introduction to PYTHIA 8.2," *Comput. Phys. Commun.*, vol. 191, pp. 159–177, 2015.

[46] D. Heck, J. Knapp, J. N. Capdevielle, G. Schatz, and T. Thouw, "CORSIKA: A Monte Carlo code to simulate extensive air showers," 1998.

[47] H. Hirayama, Y. Namito, A. F. Bielajew, S. J. Wilderman, and W. R. Nelson, "The EGS5 code system," 2005.

[48] P. Lipari, "Lepton spectra in the earth's atmosphere," *Astropart. Phys.*, vol. 1, pp. 195–227, 1993.

[49] A. Fedynitch, *Cascade equations and hadronic interactions at very high energies*. PhD thesis, KIT, Karlsruhe, Dept. Phys., 11 2015.

[50] T. Bergmann, R. Engel, D. Heck, N. N. Kalmykov, S. Ostapchenko, T. Pierog, T. Thouw, and K. Werner, "One-dimensional Hybrid Approach to Extensive Air Shower Simulation," *Astropart. Phys.*, vol. 26, pp. 420–432, 2007.

[51] A. Fedynitch, R. Engel, T. K. Gaisser, F. Riehn, and T. Stanev, "Calculation of conventional and prompt lepton fluxes at very high energy," *EPJ Web Conf.*, vol. 99, p. 08001, 2015.

[52] C. Patrignani *et al.*, "Review of Particle Physics," *Chin. Phys.*, vol. C40, no. 10, p. 100001, 2016.

[53] J. Edsjo, J. Elevant, R. Enberg, and C. Niblaeus, "Neutrinos from cosmic ray interactions in the Sun," *JCAP*, vol. 06, p. 033, 2017.

[54] M. Aartsen *et al.*, "Searches for neutrinos from cosmic-ray interactions in the Sun using seven years of IceCube data," 12 2019.

[55] G. Casella and R. Berger, *Statistical Inference*. Duxbury advanced series in statistics and decision sciences, Thomson Learning, 2002.

[56] T. Gaisser, "Seasonal variation of atmospheric neutrinos in IceCube," in *33rd International Cosmic Ray Conference*, p. 0492, 2013.

[57] S. Tilav, P. Desiati, T. Kuwabara, D. Rocco, F. Rothmaier, M. Simmons, and H. Wissing, "Atmospheric Variations as Observed by IceCube," 1 2010.

[58] M. Ambrosio *et al.*, "Seasonal variations in the underground muon intensity as seen by MACRO," *Astropart. Phys.*, vol. 7, pp. 109–124, 1997.

[59] C. F. Vigorito, G. Bruno, W. Fulgione, A. Molinario, P. Ghia, M. Selvi, and G. Trinchero, "Underground flux of atmospheric muons and its variations with 25 years of data of the LVD experiment," *PoS*, vol. ICRC2017, p. 291, 2018.

[60] M. Agostini *et al.*, "Modulations of the Cosmic Muon Signal in Ten Years of Borexino Data," *JCAP*, vol. 02, p. 046, 2019.

[61] E. W. Grashorn, J. K. de Jong, M. C. Goodman, A. Habig, M. L. Marshak, S. Mufson, S. Osprey, and P. Schreiner, "The Atmospheric charged kaon/pion ratio using seasonal variation methods," *Astropart. Phys.*, vol. 33, pp. 140–145, 2010.

[62] P. Desiati, T. Kuwabara, T. K. Gaisser, S. Tilav, and D. Rocco, "Seasonal Variations of High Energy Cosmic Ray Muons Observed by the IceCube Observatory as a Probe of Kaon/Pion Ratio," in *32nd International Cosmic Ray Conference*, vol. 1, pp. 78–81, 2011.

[63] A. E. Hedin, "Extension of the msis thermosphere model into the middle and lower atmosphere," *Journal of Geophysical Research: Space Physics*, vol. 96, no. A2, pp. 1159–1172, 1991.

[64] P. H. Barrett, L. M. Bollinger, G. Cocconi, Y. Eisenberg, and K. Greisen, “Interpretation of cosmic-ray measurements far underground,” *Rev. Mod. Phys.*, vol. 24, pp. 133–178, Jul 1952.

[65] G. D. Barr, T. K. Gaisser, S. Robbins, and T. Stanev, “Uncertainties in Atmospheric Neutrino Fluxes,” *Phys. Rev. D*, vol. 74, p. 094009, 2006.

[66] W. Heitler, *The Quantum Theory of Radiation Ed. 2.* Oxford University Press, London, (1944) p. 234 (Chap 5), 1944.

[67] J. Matthews, “A heitler model of extensive air showers,” *Astroparticle Physics*, vol. 22, no. 5, pp. 387–397, 2005.

[68] B. Rossi, *High Energy Particles.* New Jersey: Prentice-Hall Englewood Cliffs NJ., 1952.

[69] A. A. Lagutin and V. V. Uchaikin, “Adjoint cascade theory in astroparticle physics,” *Izv. Altais. Gos. Univ.*, vol. 9, pp. 4–32, 1998.

[70] Y.-S. Tsai, “Pair Production and Bremsstrahlung of Charged Leptons,” *Rev. Mod. Phys.*, vol. 46, p. 815, 1974. [Erratum: Rev. Mod. Phys.49,521(1977)].

[71] H. Bethe and W. Heitler, “On the Stopping of fast particles and on the creation of positive electrons,” *Proc. Roy. Soc. Lond.*, vol. A146, pp. 83–112, 1934.

[72] A. B. Migdal, “Bremsstrahlung and pair production in condensed media at high energies,” *Phys. Rev.*, vol. 103, pp. 1811–1820, Sep 1956.

[73] B. G. Zakharov, “Landau-Pomeranchuk-Migdal effect for finite size targets,” *Pisma Zh. Eksp. Teor. Fiz.*, vol. 64, p. 737, 1996. [JETP Lett.64,781(1996)].

[74] V. N. Baier and V. M. Katkov, “Theory of the landau-pomeranchuk-migdal effect,” *Phys. Rev. D*, vol. 57, pp. 3146–3162, Mar 1998.

[75] V. N. Baier and V. M. Katkov, “Influence of a medium on pair photoproduction and bremsstrahlung,” *Phys. Rev. D*, vol. 62, p. 036008, Jul 2000.

[76] S. R. Klein, “e+ e- pair production from 10-GeV to 10-ZeV,” *Radiat. Phys. Chem.*, vol. 75, pp. 696–711, 2006.

[77] A. B. Migdal, “Bremsstrahlung and pair production in condensed media at high-energies,” *Phys. Rev.*, vol. 103, pp. 1811–1820, 1956.

[78] L. Gerhardt and S. R. Klein, “Electron and Photon Interactions in the Regime of Strong LPM Suppression,” *Phys. Rev.*, vol. D82, p. 074017, 2010.

[79] M. L. Ter-Mikaelian, “High energy electromagnetic processes in condensed media,” *John Wiley & Sons*, 1972.

[80] P. L. Anthony *et al.*, “Measurement of dielectric suppression of Bremsstrahlung,” *Phys. Rev. Lett.*, vol. 76, pp. 3550–3553, 1996.

[81] H. Burkhardt, S. R. Kelner, and R. P. Kokoulin, “Monte Carlo generator for muon pair production,” *CERN-SL*, vol. 97-016-AP, 2002.

[82] M. Tannenbaum, “Simple formulas for the energy loss of ultrarelativistic muons by direct pair production,” *Nuclear Instruments and Methods in Physics Research Section A: Accelerators, Spectrometers, Detectors and Associated Equipment*, vol. 300, no. 3, pp. 595–604, 1991.

[83] S. R. Kelner, R. P. Kokoulin, and A. A. Petrukhin, “Bremsstrahlung from muons scattered by atomic electrons,” *Phys. Atom. Nucl.*, vol. 60, pp. 576–583, 1997.

[84] O. Klein and Y. Nishina, “Über die Streuung von Strahlung durch freie Eleketronen nach der neuen relativistischen Quantendynamik von Dirac,” *Zeitschrift fuer Physik*, vol. 52, pp. 853–868, 1929.

[85] M. Berger, J. Coursey, M. Zucker, and J. Chang, "Stopping-Power & Range Tables for Electrons, Protons, and Helium Ions," *NIST*, 1998.

[86] H. A. Bethe, "Zur Theorie des Durchgangs schneller Korpuskularstrahlen durch Materie," *Ann. d. Physik*, vol. 397, pp. 325–400, 1930.

[87] H. A. Bethe, "Bremsformel für Elektronen relativistischer Geschwindigkeit," *Z. Phys.*, vol. 76, p. 293–299, 1932.

[88] J. Abraham *et al.*, "The Fluorescence Detector of the Pierre Auger Observatory," *Nucl. Instrum. Meth.*, vol. A620, pp. 227–251, 2010.

[89] H. Tokuno *et al.*, "New air fluorescence detectors employed in the Telescope Array experiment," *Nucl. Instrum. Meth.*, vol. A676, pp. 54–65, 2012.

[90] P. A. Cerenkov, "Visible radiation produced by electrons moving in a medium with velocities exceeding that of light," *Phys. Rev.*, vol. 52, pp. 378–379, 1937.

[91] W. R. Nelson, H. Hirayama, and D. W. O. Rogers, "The Egs4 Code System," 1985.

[92] M. Niechciol, M. Risse, P. Ruehl, M. Settimo, P. W. Younk, and A. Yushkov, "F_γ : A new observable for photon-hadron discrimination in hybrid air shower events," *Astropart. Phys.*, vol. 97, pp. 88–95, 2018.

[93] S. Flügge, J. Nishimura, Y. Fujimoto, W. R. Webber, R. J. Gould, J. J. Quenby, E. Schopper, D. Lal, and M. Honda, *ENCYCLOPEDIA OF PHYSICS - COSMIC RAYS II,*. New Jersey: SPRINGER-VERLAG, 1967.

[94] C. Song, Z. Cao, B. R. Dawson, B. E. Fick, W.-Y. Lee, P. Sokolsky, and X. Zhang, "Energy estimation of UHE cosmic rays using the atmospheric fluorescence technique," *Astropart. Phys.*, vol. 14, pp. 7–13, 2000.

[95] G. Giudice and R. Rattazzi, "Theories with gauge mediated supersymmetry breaking," *Phys. Rept.*, vol. 322, pp. 419–499, 1999.

[96] M. Aaboud *et al.*, "Search for heavy charged long-lived particles in the ATLAS detector in 36.1 fb^{-1} of proton-proton collision data at $\sqrt{s} = 13$ TeV," *Phys. Rev.*, vol. D99, no. 9, p. 092007, 2019.

[97] I. F. M. Albuquerque, G. Burdman, and Z. Chacko, "Neutrino telescopes as a direct probe of supersymmetry breaking," *Phys. Rev. Lett.*, vol. 92, p. 221802, 2004.

[98] Y. Huang, M. H. Reno, I. Sarcevic, and J. Uscinski, "Weak interactions of supersymmetric staus at high energies," *Phys. Rev. D*, vol. 74, p. 115009, 2006.

[99] I. F. M. Albuquerque, G. Burdman, and Z. Chacko, "Direct detection of supersymmetric particles in neutrino telescopes," *Phys. Rev.*, vol. D75, p. 035006, 2007.

[100] M. Ahlers, J. Kersten, and A. Ringwald, "Long-lived staus at neutrino telescopes," *JCAP*, vol. 0607, p. 005, 2006.

[101] M. H. Reno, I. Sarcevic, and S. Su, "Propagation of supersymmetric charged sleptons at high energies," *Astropart. Phys.*, vol. 24, pp. 107–115, 2005.

[102] I. F. M. Albuquerque and S. R. Klein, "Supersymmetric and Kaluza-Klein Particles Multiple Scattering in the Earth," *Phys. Rev. D*, vol. 80, p. 015015, 2009.

[103] R. Abbasi *et al.*, "Lateral Distribution of Muons in IceCube Cosmic Ray Events," *Phys. Rev. D*, vol. 87, no. 1, p. 012005, 2013.

[104] D. Soldin, "Atmospheric Muons Measured with IceCube," *EPJ Web Conf.*, vol. 208, p. 08007, 2019.

[105] IceCube Collaboration (2018), "All-sky point-source IceCube data: years 2010-2012 Dataset,"

[106] M. G. Aartsen *et al.*, "All-sky Search for Time-integrated Neutrino Emission from Astrophysical Sources with 7 yr of IceCube Data," *Astrophys. J.*, vol. 835, no. 2, p. 151, 2017.

[107] J. Alwall, R. Frederix, S. Frixione, V. Hirschi, F. Maltoni, O. Mattelaer, H. S. Shao, T. Stelzer, P. Torrielli, and M. Zaro, "The automated computation of tree-level and next-to-leading order differential cross sections, and their matching to parton shower simulations," *JHEP*, vol. 07, p. 079, 2014.

[108] R. Frederix, S. Frixione, V. Hirschi, D. Pagani, H. S. Shao, and M. Zaro, "The automation of next-to-leading order electroweak calculations," *JHEP*, vol. 07, p. 185, 2018.

[109] H.-L. Lai, M. Guzzi, J. Huston, Z. Li, P. M. Nadolsky, J. Pumplin, and C. P. Yuan, "New parton distributions for collider physics," *Phys. Rev.*, vol. D82, p. 074024, 2010.

[110] R. D. Ball *et al.*, "Parton distributions for the LHC Run II," *JHEP*, vol. 04, p. 040, 2015.

[111] J. M. Lindert, F. D. Steffen, and M. K. Trenkel, "Direct stau production at the LHC," *PoS*, vol. CORFU2011, p. 024, 2011.

[112] M. Ahlers, J. I. Illana, M. Masip, and D. Meloni, "Long-lived staus from cosmic rays," *JCAP*, vol. 0708, p. 008, 2007.

[113] M. Tanabashi *et al.*, "Review of Particle Physics," *Phys. Rev. D*, vol. 98, no. 3, p. 030001, 2018.

[114] D. E. Groom, "Atomic and nuclear properties of materials," 2008.

[115] D. E. Groom, N. V. Mokhov, and S. I. Striganov, "Muon stopping power and range tables 10-MeV to 100-TeV," *Atom. Data Nucl. Data Tabl.*, vol. 78, pp. 183–356, 2001.

[116] M. G. Aartsen *et al.*, "Characteristics of the diffuse astrophysical electron and tau neutrino flux with six years of IceCube high energy cascade data," 2020.

[117] M. Aartsen *et al.*, "Energy Reconstruction Methods in the IceCube Neutrino Telescope," *JINST*, vol. 9, p. P03009, 2014.

[118] M. G. Aartsen *et al.*, "Evidence for Astrophysical Muon Neutrinos from the Northern Sky with IceCube," *Phys. Rev. Lett.*, vol. 115, no. 8, p. 081102, 2015.

[119] M. Aartsen *et al.*, "Searches for Extended and Point-like Neutrino Sources with Four Years of IceCube Data," *Astrophys. J.*, vol. 796, no. 2, p. 109, 2014.

[120] G. J. Feldman and R. D. Cousins, "A Unified approach to the classical statistical analysis of small signals," *Phys. Rev. D*, vol. 57, pp. 3873–3889, 1998.

[121] J. van Santen, "IceCube-Gen2: the next-generation neutrino observatory for the South Pole," *PoS*, vol. ICRC2017, p. 991, 2018.

[122] M. Aguilar *et al.*, "Antiproton Flux, Antiproton-to-Proton Flux Ratio, and Properties of Elementary Particle Fluxes in Primary Cosmic Rays Measured with the Alpha Magnetic Spectrometer on the International Space Station," *Phys. Rev. Lett.*, vol. 117, no. 9, p. 091103, 2016.

[123] A. Abeysekara *et al.*, "Constraining the $\bar{p}/p$ ratio in TeV cosmic rays with observations of the Moon shadow by HAWC," *Phys. Rev. D*, vol. 97, no. 10, p. 102005, 2018.

[124] B. Bartoli *et al.*, "Measurement of the cosmic ray antiproton/proton flux ratio at TeV energies with the ARGO-YBJ detector," *Phys. Rev. D*, vol. 85, p. 022002, 2012.

[125] K. Hamaguchi, T. Moroi, and K. Nakayama, "Ams-02 antiprotons from annihilating or decaying dark matter," *Physics Letters B*, vol. 747, pp. 523 – 528, 2015.

[126] D. Maurin, R. Taillet, F. Donato, P. Salati, A. Barrau, and G. Boudoul, "Galactic cosmic ray nuclei as a tool for astroparticle physics," 12 2002.

[127] F. Donato, N. Fornengo, D. Maurin, and P. Salati, "Antiprotons in cosmic rays from neutralino annihilation," *Phys. Rev. D*, vol. 69, p. 063501, 2004.

[128] T. K. Gaisser, "Spectrum of cosmic-ray nucleons, kaon production, and the atmospheric muon charge ratio," *Astropart. Phys.*, vol. 35, pp. 801–806, 2012.

[129] M. G. Aartsen *et al.*, "Measurement of the cosmic ray energy spectrum with IceTop-73," *Phys. Rev. D*, vol. 88, no. 4, p. 042004, 2013.

[130] T. Antoni *et al.*, "KASCADE measurements of energy spectra for elemental groups of cosmic rays: Results and open problems," *Astropart. Phys.*, vol. 24, pp. 1–25, 2005.

[131] M. I. Latz, T. M. Frank, and J. F. Case, "Spectral composition of bioluminescence of epipelagic organisms from the Sargasso Sea," *Marine Biology*, vol. 98, pp. 441–446, June 1988.

[132] P. J. Herring and M. R. Clarke, "The spectral characteristics of luminous marine organisms," *Proceedings of the Royal Society of London. Series B. Biological Sciences*, vol. 220, no. 1219, pp. 183–217, 1983.

[133] R. Claus *et al.*, "A waveshifter light collector for a water cherenkov detector," *Nuclear Instruments and Methods in Physics Research Section A: Accelerators, Spectrometers, Detectors and Associated Equipment*, vol. 261, no. 3, pp. 540 – 542, 1987.

[134] F. Kulcsár, D. Teherani, and H. Altmann, "Study of the spectrum of cherenkov light," *Journal of radioanalytical chemistry*, vol. 68, pp. 161–168, Mar. 1982.

[135] J. Aguzzi *et al.*, "Inertial bioluminescence rhythms at the Capo Passero (KM3NeT-Italia) site, Central Mediterranean Sea," *Scientific Reports*, vol. 7, p. 44938, Mar. 2017.

[136] A. A. Badr, M. Garel, P. Cuny, J. Miquel, T. Toubal, A. Robert, and C. Tamburini, "Luminous bacteria in the deep-sea waters near the antares underwater neutrino telescope (mediterraean sea)," *Chemistry and Ecology*, vol. 26, pp. 57–72, 03 2010.

[137] I. G. Priede, A. Jamieson, A. Heger, J. Craig, and A. F. Zuur, "The potential influence of bioluminescence from marine animals on a deep-sea underwater neutrino telescope array in the Mediterranean Sea," *Deep Sea Research Part I: Oceanographic Research Papers*, vol. 55, no. 11, pp. 1474 – 1483, 2008.

[138] J. Craig, A. J. Jamieson, A. Heger, and I. G. Priede, "Distribution of bioluminescent organisms in the mediterranean sea and predicted effects on a deep-sea neutrino telescope," *Nuclear Instruments and Methods in Physics Research Section A: Accelerators, Spectrometers, Detectors and Associated Equipment*, vol. 602, no. 1, pp. 224 – 226, 2009. Proceedings of the 3rd International Workshop on a Very Large Volume Neutrino Telescope for the Mediterranean Sea.

[139] S. Meighen-Berger, L. Ruohan, and G. Wimmer, "Bioluminescence modeling for deep sea experiments," 2021.

[140] J. Rohr, M. I. Latz, S. Fallon, J. C. Nauen, and E. Hendricks, "Experimental approaches towards interpreting dolphin-stimulated bioluminescence.," *Journal of Experimental Biology*, vol. 201, no. 9, pp. 1447–1460, 1998.

[141] M. I. Latz, A. R. Juhl, A. M. Ahmed, S. E. Elghobashi, and J. Rohr, "Hydrodynamic stimulation of dinoflagellate bioluminescence: a computational and experimental study," *Journal of Experimental Biology*, vol. 207, no. 11, pp. 1941–1951, 2004.

[142] R. JJ, M. Latz, S. Fallon, J. Nauen, and E. Hendricks, "Experimental approaches towards interpreting dolphin-stimulated bioluminescence," *The Journal of experimental biology*, vol. 201, pp. 1447–60, 06 1998.

[143] M. I. Latz and J. Rohr, "Luminescent response of the red tide dinoflagellate lingulodinium polyedrum to laminar and turbulent flow," *Limnology and Oceanography*, vol. 44, no. 6, pp. 1423–1435, 1999.

[144] J. Nauen, *Biomechanics of Two Aquatic Defense Systems: 1. The Scaling of Tail-flip Kinematics and Force Production by the California Spiny Lobster Panulirus Interruptus : 2. Shear Sensitivity and Interspecific Variation in Flow-stimulated Dinoflagellate Bioluminescence*. Dissertations, University of California, San Diego, 1998.

[145] J. Rohr, M. Hyman, S. Fallon, and M. I. Latz, "Bioluminescence flow visualization in the ocean: an initial strategy based on laboratory experiments," *Deep Sea Research Part I: Oceanographic Research Papers*, vol. 49, no. 11, pp. 2009 – 2033, 2002.

[146] M. D. Stokes, G. B. Deane, M. I. Latz, and J. Rohr, "Bioluminescence imaging of wave-induced turbulence," *Journal of Geophysical Research: Oceans*, vol. 109, no. C1, 2004.

[147] D. K. Hartline, E. J. Buskey, and P. H. Lenz, "Rapid jumps and bioluminescence elicited by controlled hydrodynamic stimuli in a mesopelagic copepod, pleuromamma xiphias," *The Biological Bulletin*, vol. 197, no. 2, pp. 132–143, 1999. PMID: 28281821.

[148] E. M. Maldonado and M. I. Latz, "Shear-stress dependence of dinoflagellate bioluminescence," *Biological Bulletin*, vol. 212, no. 3, pp. 242–249, 2007.

[149] H. Schlichting and K. Gersten, *Boundary-Layer Theory*. 01 2017.

[150] J. Laufer and U. S. N. A. C. f. Aeronautics, *The Structure of Turbulence in Fully Developed Pipe Flow*. ARC-16399, National Advisory Committee for Aeronautics, 1954.

[151] E. A. Widder, S. A. Bernstein, D. F. Bracher, J. F. Case, K. R. Reisenbichler, J. J. Torres, and B. H. Robison, "Bioluminescence in the Monterey Submarine Canyon: image analysis of video recordings from a midwater submersible," *Marine Biology*, vol. 100, pp. 541–551, Mar. 1989.

[152] M. S. Engelman and M.-A. Jamnia, "Transient flow past a circular cylinder: a benchmark solution," *International Journal for Numerical Methods in Fluids*, vol. 11, no. 7, pp. 985–1000, 1990.

[153] J. H. Lienhard *et al.*, *Synopsis of lift, drag, and vortex frequency data for rigid circular cylinders*, vol. 300. Technical Extension Service, Washington State University Pullman, WA, 1966.

[154] C. Norberg, "Fluctuating lift on a circular cylinder: review and new measurements," *Journal of Fluids and Structures*, vol. 17, no. 1, pp. 57–96, 2003.

[155] A. Roshko, "On the development of turbulent wakes from vortex streets," 1953.

[156] R. Wille, "Karman vortex streets," in *Advances in Applied Mechanics*, vol. 6, pp. 273–287, Elsevier, 1960.

[157] H. C. Elman, D. J. Silvester, and A. J. Wathen, *Finite elements and fast iterative solvers: with applications in incompressible fluid dynamics*. Numerical Mathematics and Scie, 2014.

[158] C. Taylor and P. Hood, "A numerical solution of the navier-stokes equations using the finite element technique," *Computers & Fluids*, vol. 1, no. 1, pp. 73–100, 1973.

[159] K. Goda, "A multistep technique with implicit difference schemes for calculating two-or three-dimensional cavity flows," *Journal of computational physics*, vol. 30, no. 1, pp. 76–95, 1979.

[160] A. Quarteroni, R. Sacco, and F. Saleri, *Numerical mathematics*, vol. 37. Springer Science & Business Media, 2010.

[161] A. N. Brooks and T. J. Hughes, "Streamline upwind/petrov-galerkin formulations for convection dominated flows with particular emphasis on the incompressible navier-stokes equations," *Computer methods in applied mechanics and engineering*, vol. 32, no. 1-3, pp. 199–259, 1982.

[162] T. E. Tezduyar, "Stabilized finite element formulations for incompressible flow computations," *Advances in applied mechanics*, vol. 28, pp. 1–44, 1991.

[163] C. Geuzaine and J.-F. Remacle, "Gmsh: A 3-d finite element mesh generator with built-in pre-and post-processing facilities," *International journal for numerical methods in engineering*, vol. 79, no. 11, pp. 1309–1331, 2009.

[164] M. Homolya, L. Mitchell, F. Luporini, and D. A. Ham, "TSFC: a structure-preserving form compiler," *SIAM Journal on Scientific Computing*, vol. 40, no. 3, pp. C401–C428, 2018.

[165] F. Luporini, D. A. Ham, and P. H. Kelly, "An algorithm for the optimization of finite element integration loops," *ACM Transactions on Mathematical Software (TOMS)*, vol. 44, no. 1, pp. 1–26, 2017.

[166] F. Rathgeber, D. A. Ham, L. Mitchell, M. Lange, F. Luporini, A. T. T. McRae, G. T. Bercea, G. R. Markall, and P. H. J. Kelly, “Firedrake: automating the finite element method by composing abstractions,” *ACM Transactions on Mathematical Software (TOMS)*, vol. 43, no. 3, pp. 1–27, 2016.

[167] S. Balay, S. Abhyankar, M. Adams, J. Brown, P. Brune, K. Buschelman, L. Dalcin, A. Dener, V. Eijkhout, W. D. Gropp, *et al.*, “PETSc users manual,” 2019.

[168] S. Balay, W. D. Gropp, L. C. McInnes, and B. F. Smith, “Efficient management of parallelism in object-oriented numerical software libraries,” in *Modern software tools for scientific computing*, pp. 163–202, Springer, 1997.

[169] M. Behr, D. Hastreiter, S. Mittal, and T. Tezduyar, “Incompressible flow past a circular cylinder: dependence of the computed flow field on the location of the lateral boundaries,” *Computer Methods in Applied Mechanics and Engineering*, vol. 123, no. 1-4, pp. 309–316, 1995.

[170] H. Bradner *et al.*, “Attenuation of light in clear deep ocean water,” 1992.

[171] E. J. Buskey and E. Swift, “An encounter model to predict natural planktonic bioluminescence,” *Limnology and Oceanography*, vol. 35, no. 7, pp. 1469–1485, 1990.